Machine learning links T cell function and spatial localization to neoadjuvant immunotherapy and clinical outcome in pancreatic cancer

Katie E. Blise[1,2], Shamilene Sivagnanam[2,3], Courtney B. Betts[2,3,4], Konjit Betre[3], Nell Kirchberger[3], Benjamin Tate[2,5], Emma E. Furth[6,7], Andressa Dias Costa[8], Jonathan A. Nowak[9], Brian M. Wolpin[8], Robert H. Vonderheide[7,10], Jeremy Goecks[1,2,11,12,*], Lisa M. Coussens[2,3,*], Katelyn T. Byrne[2,3,13,*]

[1]Department of Biomedical Engineering, Oregon Health & Science University, Portland, OR USA

[2]The Knight Cancer Institute, Oregon Health & Science University, Portland, OR USA

[3]Department of Cell, Developmental & Cancer Biology, Oregon Health & Science University, Portland, OR USA

[4]Current affiliation: Akoya Biosciences, 100 Campus Drive, 6th Floor, Marlborough, MA USA

[5]Immune Monitoring and Cancer Omics Services, Oregon Health & Science University, Portland, OR USA

[6]Department of Pathology and Laboratory Medicine, Hospital of the University of Pennsylvania, Philadelphia, PA USA

[7]Abramson Cancer Center, Perelman School of Medicine, University of Pennsylvania, Philadelphia, PA USA

[8]Department of Medical Oncology, Dana-Farber Cancer Institute, Harvard Medical School, Boston, MA USA

[9]Department of Pathology, Brigham and Women's Hospital and Harvard Medical School, Boston, MA USA

[10]Parker Institute for Cancer Immunotherapy, Perelman School of Medicine, University of Pennsylvania, Philadelphia, PA USA

[11]Current affiliation: Department of Machine Learning, H. Lee Moffitt Cancer Center, Tampa, FL USA

[12]Current affiliation: Department of Biostatistics and Bioinformatics, H. Lee Moffitt Cancer Center, Tampa, FL USA

[13]Lead contact

*Co-corresponding author

*Co-corresponding authors: jeremy.goecks@moffitt.org (J.G.), coussenl@ohsu.edu (L.M.C.), byrneka@ohsu.edu (K.T.B.)

ABSTRACT

Tumor molecular datasets are becoming increasingly complex, making it nearly impossible for humans alone to effectively analyze them. Here, we demonstrate the power of using machine learning to analyze a single-cell, spatial, and highly multiplexed proteomic dataset from human pancreatic cancer and reveal underlying biological mechanisms that may contribute to clinical outcome. A novel multiplex immunohistochemistry antibody panel was used to audit T cell functionality and spatial localization in resected tumors from treatment-naive patients with localized pancreatic ductal adenocarcinoma (PDAC) compared to a second cohort of patients treated with neoadjuvant agonistic CD40 (αCD40) monoclonal antibody therapy. In total, nearly 2.5 million cells from 306 tissue regions collected from 29 patients across both treatment cohorts were assayed, and more than 1,000 tumor microenvironment (TME) features were quantified. We then trained machine learning models to accurately predict αCD40 treatment status and disease-free survival (DFS) following αCD40 therapy based upon TME features. Through downstream interpretation of the machine learning models' predictions, we found αCD40 therapy to reduce canonical aspects of T cell exhaustion within the TME, as compared to treatment-naive TMEs. Using automated clustering approaches, we found improved DFS following αCD40 therapy to correlate with the increased presence of $CD44^{+}$ $CD4^{+}$ Th1 cells located specifically within cellular spatial neighborhoods characterized by increased T cell proliferation, antigen-experience, and cytotoxicity in immune aggregates. Overall, our results demonstrate the utility of machine learning in molecular cancer immunology applications, highlight the impact of αCD40

therapy on T cells within the TME, and identify potential candidate biomarkers of DFS for αCD40-treated patients with PDAC.

KEYWORDS

Tumor microenvironment, machine learning, T cell, pancreatic ductal adenocarcinoma, spatial proteomics

INTRODUCTION

Pancreatic ductal adenocarcinoma (PDAC) is one of the most aggressive treatment-refractory cancers with a median overall survival rate of just months, thus there is a critical need for new treatment strategies for this disease (1-3). Recent reports reveal that immunological responses in PDAC can be temporarily induced via approaches that promote priming of T cell responses against PDAC, such as occurs following agonistic CD40 (αCD40) monoclonal antibodies (4) and peptide vaccination (5) strategies. We and others have previously reported that αCD40 binds to CD40 on dendritic cells (DCs), thereby licensing DCs to subsequently enhance T cell activation and bolster anti-tumor immunity (6-8). However, little is known regarding selective impact of αCD40 therapy on specific T cell states within the TME and to what degree this therapy sustains T cell functionality in situ, or instead promotes T cell dysfunction that could in turn limit potential use of αCD40 combination therapies in the clinical setting.

Upon antigen stimulation, T cells upregulate CD44 and exist along a spectrum of diverse differentiation states with varying functionalities (9-11). On one end of the spectrum, T cells possess stem-cell-like plasticity, accompanied by memory, proliferative and cytotoxic capabilities, and are identified by expression of T-BET, and/or TCF-1 (12, 13). On the other end of the spectrum, T cells are exhausted and/or dysfunctional and canonically express TOX1 and/or EOMES (14, 15). Along the spectrum, expressed in varying combinations, are T cells expressing immune checkpoint molecules such as PD-1, LAG-3 and TIM3, with increased numbers of immune checkpoint molecules correlating with more exhausted T cells (16). These partially exhausted T cells are susceptible to

reinvigoration by immune checkpoint blockade (ICB) and regain the ability to proliferate and produce effector cytokines after PD-1 blockade, for example (17, 18). However, terminally differentiated T cells expressing TOX1 or EOMES are resistant to rescue by ICB and cannot proliferate or exert cytotoxic activity (19). Flow cytometric analyses of T cells in preclinical tumor models or tissues following viral infection have elucidated notable T cell states associated with priming, proliferation, cytotoxic capability, or functional exhaustion; however, characterizations of effector versus exhausted T cell phenotypes from tumors in patients are scant. Moreover, with the advent of single-cell sequencing approaches, the diversity of T cell subset possibilities within tumors is seemingly endless and in need of clarification (20, 21). We sought to clarify T cell subset characteristics within the PDAC TME, and to identify those subsets associated with response to therapeutic αCD40 therapy. Recognizing that both the cellular composition and spatial organization of cells, including T cells, is a critical metric associated with therapeutic response and clinical outcome (22-32), we investigated and report on the impact of αCD40 therapy on the complex spatial contexture of T cells within the PDAC TME and association with survival.

We previously developed a multiplex immunohistochemistry (mIHC) single-cell spatial proteomics imaging platform to interrogate leukocyte heterogeneity and spatial landscape within the TMEs of various cancer types (33-35). Following a cyclical staining protocol, the mIHC platform iteratively utilizes up to 30 antibodies to stain protein biomarkers on a single tissue specimen, thus preserving spatial context of the TME. The resulting data provide single-cell resolution maps, which can be quantified by several metrics including

cellular density, cell-cell spatial interactions, and cellular neighborhoods. While it is possible to quantify and correlate each of these TME features individually with clinical outcome, this approach fails to combine and weight features together to capture biological complexities of the TME. Machine learning can be used to address TME complexity, as it is a form of artificial intelligence whereby computational models are trained to identify which combinations of data features can predict a given output. Models can then be used to make accurate predictions from new data and interrogated to understand which combinations of features are most important in making the predictions. Machine learning is becoming widely utilized in precision oncology to decipher patterns in large data sets resulting from deep interrogations (36-39).

Here, we leveraged machine learning to elucidate the frequency of various T cell states in PDAC and investigated the impact of αCD40 therapy on those states. We first designed a novel mIHC antibody panel to deeply audit T cell functionality and spatial organization in two PDAC cohorts, one of which was treatment-naive and the other of which received neoadjuvant αCD40 therapy. Using this mIHC panel, we generated a dataset of nearly 2.5 million cells with spatially resolved single-cell phenotypic and functional measurements. Interrogation of this dataset presented a unique opportunity to elucidate: 1) the types of T cells present at baseline in a treatment-refractory disease and 2) to what degree αCD40 therapy sustains T cell functionality in situ, or instead promotes T cell dysfunction that could in turn limit potential use of αCD40 or other T cell priming therapies in the clinical setting. Given the vast amount of spatially resolved data and complexity of T cell function in the TME, we leveraged machine learning approaches to discern new

biological insights regarding T cells in the pancreatic TME and their association with clinical outcome for pancreatic cancer patients.

MATERIALS AND METHODS

Tissue Acquisition

Human PDAC tissue specimens from cohort 1 were obtained from patients with approval from the Oregon Pancreas Tissue Registry under Oregon Health & Science University IRB protocol #3609 and Dana Farber Harvard Cancer Center protocols #03-189 and #12-013 (**Fig. 1A**). Specimens from cohort 2 were obtained from patients treated with neoadjuvant selicrelumab with approval under the IRBs of four sites across the United States involved in an open-label phase I clinical trial (Cancer Immunotherapy Trials Network CITN11-01; NCT02588443; **Fig. 1A**), including 8 patients with neoadjuvant selicrelumab alone and 3 patients with neoadjuvant selicrelumab combined with gemcitabine and nab-paclitaxel. For the purposes of this paper, this cohort has been combined as the αCD40-treated cohort given previous analyses of the TME (4). All studies were conducted in accordance with the Declaration of Helsinki and written informed consent was obtained.

Multiplex Immunohistochemistry Image Acquisition and Analysis

Formalin-fixed, paraffin-embedded (FFPE) surgical tissue samples were sectioned and assessed using hematoxylin and eosin (H&E), as well as chromogen based mIHC. Using pathologist annotations overlaid from the H&E-stained slides, sections were assessed with regard to histopathologic regions of interest (ROI; **Fig. 1B**) annotated as tumor (T), immune aggregate (IA), tumor-adjacent stroma (TAS), or normal-adjacent pancreas (NAP), as defined by the pathologist (35). Multiplex staining was performed on 5 μm sections, as previously described, and each stained image was scanned at 20x

magnification on an Aperio AT2 scanner (Leica Biosystems) (35). The antibody panel was designed to delineate epithelial cells, mesenchymal cells, B cells, myeloid cells, and 18 T cell subpopulations, spanning T cell activation and exhausted states. Human tonsil and spleen were included in all rounds of mIHC as staining controls. Image processing was performed using previously described methods (35). Each region was registered to the final hematoxylin using Matlab Computer Vision Toolbox (The Mathworks, Inc., Natick, MA), color deconvolution and watershed-based nuclei segmentation was performed using ImageJ, and single cell mean intensity for each stain was quantified using Cell Profiler (40). Single marker positivity thresholds were set using FCS Express Image Cytometry RUO (De Novo Software, Glendale, CA) to visually validate protein biomarker expression overlaid on signal extracted images. Single cell classification was performed using R Statistical Software based on filtering exclusive populations in a defined hierarchy.

Machine Learning Classifiers and Feature Importance Analyses

Elastic net (EN) classifier models were built to predict: 1) treatment status and 2) disease-free survival (DFS), using scikit-learn's LogisticRegression function (41). Predictions were made on a region basis to maximize sample size and model robustness. Separate models were created for each histopathologic site in order to: 1) compare performance of models derived from different histopathologic sites; 2) identify where therapy was potentially exerting greatest impact; and 3) mitigate broad variation in average tissue area from each histopathologic site (**Fig. 1B**). A leave-one-patient-out cross-validation approach was used to split the train and test sets. Thus, within each cross-validation loop, a new EN

model was created and trained on all regions except those from one patient, and testing was then performed on regions from the patient withheld from training. This process was repeated until all patients were cycled through the test set. This approach prevents data leakage by ensuring regions from the same patient were not in both the train and test sets for one model, thus preventing the EN models from learning patient-specific features, which often artificially increases model accuracy. Test set predictions were aggregated across all cross-validation loops to construct one final confusion matrix, from which performance of the models was assessed by calculating accuracy, F1 score, and area under the receiver operating characteristic curve (AUC). These metrics address both precision and recall (F1 score), in addition to the true positive rate and false positive rate (AUC) – these are often used to assess performance of classifier models. Model overfitting was mitigated by using the same model hyperparameters across cross-validation loops. The penalty term was set to "elasticnet," and the "l1_ratio" hyperparameter was set to 0.5, representing an equal balance of the lasso model and ridge model effects. All features were log10+1 normalized and scaled using a minmax [0,1] scaler in order to equally compare features spanning different orders of magnitude and improve model interpretability. To further prevent data leakage, in each cross-validation loop, the scaler was fit to the train set and then applied to the train set and subsequently the test set. Test feature outliers were clipped to [0,1] following this normalization. The train set was balanced within each cross-validation loop using Synthetic Minority Over-sampling Technique (SMOTE) to up-sample the minority class to equal the majority class (42). Feature importance analyses were conducted by computing Shapley Additive exPlanations (SHAP) values for each model (43). SHAP values enable

the interpretation of which combinations of features contribute to the overall model predictions.

Cell-Cell Spatial Interaction Quantification

Cell-cell interactions were defined as cells separated by a distance of ≤ 20 μm, according to centroid (x,y) coordinates of any two cells, enriching for cells that were directly adjacent as previously reported (44-46). Total cell-cell interactions were normalized by dividing summed densities of cell states involved in the interactions to avoid skewing by cell states present in high abundances.

Recurrent Cellular Neighborhood Analysis

Recurrent cellular neighborhoods were quantified to assess spatial organization of tissues. A neighborhood was created for every cell by counting all cells within a 60 μm radius of each seed cell's center, as inferred from previous studies (47-50). Using proportions of cells comprising the neighborhoods as features, neighborhoods were grouped using K-means clustering. The elbow method was used to determine the number of clusters, resulting in groupings of spatial neighborhoods that were similar in cellular composition that could be found across all regions of interest in the analysis.

Statistics

Mann-Whitney U tests were used to determine statistically significant differences in top TME features between treatment cohorts or DFS groups. The Benjamini-Hochberg correction was used to account for multiple hypothesis testing for each analysis. *P*-values

less than 0.05 were considered statistically significant. Statistical calculations were performed with the Scipy and statsmodels packages using Python software (51, 52).

DATA AVAILABILITY

mIHC data used for this study is available for download on Zenodo at https://doi.org/10.5281/zenodo.8357193.

CODE AVAILABILITY

The code used to generate all computational results of this research was created using Python version 3.9.4 and is available at https://github.com/kblise/PDAC_mIHC_paper.

RESULTS

Designing a novel mIHC antibody panel to deeply phenotype T cells within the PDAC TME

29 PDAC tumors were surgically resected from patients across two treatment cohorts (**Fig. 1A**). Tumors from cohort 1 were treatment-naive upon resection and were previously evaluated for immune contexture as a subset of a larger study (n=104 tumors) designed to broadly evaluate leukocyte composition in treatment-naive PDAC (35). The 18 treatment-naive tumors evaluated in the current study were selected as a representative subset of the larger PDAC cohort based on cellular subsets not being statistically different from the full cohort in terms of leukocyte densities or patient survival durations (**Supplementary Table S1**). Thus, PDAC specimens from cohort 1 served as a representative baseline comparison to the 11 specimens from cohort 2, which reflected patients who had received neoadjuvant αCD40 therapy alone (n=8) or in combination with gemcitabine and nab-paclitaxel (n=3) prior to resection (4). Three to 26 ROIs per PDAC resection were selected by a pathologist and quantitatively assayed by mIHC, with each region annotated as one of four histopathologic sites within the resected samples: tumor (T), immune aggregate (IA), tumor-adjacent stroma (TAS), or normal-adjacent pancreas (NAP) (**Fig. 1B**) (35). Breakdown of region types assayed per patient are shown (**Fig. 1C**).

In total, nearly 2.5 million cells were assayed across 306 tissue regions by our novel 21-antibody mIHC panel (**Fig. 1D** and **E**, **Supplementary Table S2**, **Supplementary Fig. S1A**). Given our goal of revealing T cell states present in the PDAC TME at baseline, and

the impact of αCD40 therapy on those T cells, the majority of antibodies included in the mIHC panel were chosen for their ability to elucidate differentiation, exhaustion, proliferative and cytotoxic status of various T cell lineage subtypes as defined by prior literature (14, 53-57). First, 423,317 T cells were identified by CD3 expression and then subsequently stratified by CD8α expression. $CD8^+$ T cells were further classified as one of six cell states (T_{NAIVE}, T_{EFF}, T_{EM}, T_{EMRA}, T_{EX}, or T_{TEX}) (**Fig. 1F**). Due to biomarker selection and positional restrictions within the cyclic multiplex panel, we did not include a CD4 antibody. However, the majority (72%) of $CD3^+$ $CD8^-$ T cells were $CD4^+$ as determined in a testing panel using a subset of the data (**Supplementary Fig. S1B**); we therefore refer to $CD3^+$ $CD8^-$ T cells as $CD4^+$ T cells herein, although it is possible other minor lineages may be represented (20). Based on this schema, $CD3^+$ $CD8^-$ T cells were further evaluated; $CD4^+$ Th1 cells were defined by T-BET^+ expression, and further classified as one of three cell states (T_{EFF}, T_{EM}, or T_{EMRA}) (**Fig. 1F**). We originally anticipated the majority of $CD8^+$ T cells and $CD4^+$ Th1 cells would fall into one of the clearly defined states (e.g., T_{NAIVE}, T_{EFF}, T_{EM}, T_{EMRA}, T_{EX}, T_{TEX}); however, only 6% of $CD8^+$ T or $CD4^+$ Th1 cells were phenotyped as one of these states (**Supplementary Table S3**). To investigate the remaining 94% – labeled T_{OTHER} (**Fig. 1F**) – we stratified cells based on expression of CD44, a canonical biomarker of prior cognate antigen experience. Furthermore, there was a population of T-BET^- $CD4^+$ Th cells (non-Th1-specific T helper cells), which we stratified into two cell states based upon CD44 expression only (**Fig. 1F**). Finally, the remaining $CD3^+$ $CD8^-$ T cells were $FOXP3^+$ T_{REG} cells, and classified into three cell states (Naive T_{REG}, mT_{REG}, and T-BET^+ T_{REG}) (**Fig. 1F**). Despite low numbers of certain T cell states (**Supplementary Table S3**), we included all 18 T cell states in

downstream analyses based upon calculations from previous single-cell studies (58), as well as the fact that these populations were manually gated and thus represent real phenotypes of T cells present in the PDAC TME. In addition, we utilized antibodies for 10 T cell functionality biomarkers to assess differentiation/exhaustion status on all T cells (TOX1, TIM3, TCF-1, CD38, PD-1, EOMES, CD39, CD44, LAG-3, and T-BET), as well as for proliferation (Ki-67) and cytotoxicity (granzyme B, GrzB) (**Fig. 1D**, **E**). Finally, the remaining $CD3^-$ (non-T) cells were defined by a hierarchical gating strategy and classified as B cells, myeloid cells, mesenchymal fibroblast-like cells (also referred to as mesenchymal cells), or neoplastic epithelial cells (**Fig. 1F**, **Supplementary Fig. S1C**). Altogether, cells were phenotyped as one of 23 different cell lineages and states (**Fig. 1F**).

Interrogating cell states and spatial interactions within the PDAC TME

Using single-cell spatial data collected from the mIHC assay, we used three approaches to quantify treatment-naive and αCD40-treated PDAC TMEs: 1) Cell state densities, to identify types of cells present (**Supplementary Table S3**); 2) T cell "functionality barcodes," to reflect functional phenotypes of T cells by unique combinations of functional biomarker expression (**Supplementary Table S4**); and 3) Cell-cell spatial interactions, to reveal relative locations between cell types (**Supplementary Table S5**). Using these three metrics, we created a granular map of leukocyte infiltration, T cell functionality status, and cellular spatial orientation in the PDAC TME (**Fig. 2**).

To identify the types and amounts of cell states present in the PDAC TME, we first quantified densities of each of the 23 cell states for each tissue region assayed by dividing raw counts of cells (**Supplementary Table S3**) by tissue area. Varying densities of leukocytes, mesenchymal fibroblast-like cells, and neoplastic epithelial cells were present in regions of each histopathologic annotation and each treatment cohort (**Fig. 2A**, **top**). In T regions, neoplastic epithelial cells were dominant. In IA regions, T cells and B cells were most prevalent, while in TAS regions, which encompassed the tumor borders, there was a mix of neoplastic cells, T cells, myeloid cells, and mesenchymal cells. Finally, myeloid cells were the dominant population in distal NAP regions. T cells were further divided into 18 T cell states defined by the mIHC gating strategy (**Fig. 1F**, **white boxes**). On average, $CD4^+$ T cells were present in increased densities, nearly two-fold, as compared to $CD8^+$ T cells (**Fig. 2A**, **middle**, **bottom rows**), regardless of histopathologic type or treatment cohort. However, average densities of the $CD8^+$ and $CD4^+$ T cell states often differed by histopathologic site and treatment cohort. These results demonstrate the importance of identifying spatial and histopathological information for interpreting how – and where – αCD40 therapy alters T cells in the PDAC TME, important information that could not be captured by flow cytometric methodologies.

To understand how T cell functionality differed based on histopathology and prior treatment, we assigned all T cell states a “Functionality Barcode,” as defined by binary positive or negative expression of unique combinations of 10 T cell functionality biomarkers (**Fig. 1D**, **middle column**). Among the 423,317 T cells present in the dataset, we identified expression of 961 unique barcodes (**Supplementary Table S4**). The top 15

most common barcodes by average density are shown for each histopathologic type and treatment cohort (**Fig. 2B**). Over half of the most common barcoded T cells were present in both treatment cohorts, regardless of histopathologic site, as indicated by brown bars (**Fig. 2B**). Of the barcodes present in 'high' densities only within the treatment-naive cohort (orange bars), the majority contained two functionality biomarkers; however, of the most abundant barcodes present in the αCD40 cohort only (blue bars, **Fig. 2B**), the majority contained three or more functionality biomarkers. This result supports the hypothesis that αCD40 therapy shifts T cell differentiation/functionality within the PDAC TME, as represented by an increase in the number of functionality biomarkers expressed. However, further elucidation of the specific patterns of biomarkers expressed by T cells is needed to identify the direction of this shift following immunotherapy.

Finally, to address spatial organization of cells in the PDAC TME, we leveraged the fact that mIHC preserves spatial context and quantified frequency of two cell states interacting, based on their cell centers being within 20 μm from each other (44-46). We identified 268 unique pairs of cell-cell interactions present in the datasets (**Supplementary Table S5**). On average, there were increased interactions between $CD4^+$ T cells of various subpopulation states with other $CD4^+$ T cells in the αCD40 cohort, regardless of histopathologic site (**Fig. 2C**, **white boxes**). Altogether, these results support the hypothesis that αCD40 drives an increase in $CD4^+$ T cell density, functional capacity, and spatial proximity in the PDAC TME, as compared to treatment-naive PDAC TMEs.

Following these three TME single-cell quantification methods, all 2,428,274 cells present across the 306 regions were phenotyped as one of 23 cell states. In addition, all 423,317 T cells were assigned one of 961 T cell functionality barcodes. Finally, the immediate spatial neighbors of each cell were computed and binned into one of 268 types of pairwise cell-cell interactions. In total, 1,252 TME features were computed across the 306 regions, and each region was annotated as one of four histopathologic sites. Given the complexity and large amount of data, we leveraged machine learning and feature importance analyses to identify: 1) impact of αCD40 therapy on composition, functional capacity, and spatial organization of cells within the PDAC TME, and 2) the likely mechanism(s) we hypothesized underlying improved clinical outcome following αCD40 therapy. To do this, we trained EN classifier models to predict treatment status and DFS within the αCD40-treated cohort from the 1,252 TME features quantified above (**Fig. 2D** and **Methods**). EN models perform well on datasets as generated herein where there are more features than samples (tissue regions) (59). This is because EN models use mathematical regularization approaches to identify and select the most informative subset of features to make model predictions while accounting for feature collinearity (60). Further, our approach was unbiased as we did not perform any prior feature selection and instead provided all 1,252 TME features to the models, leveraging the EN algorithm's ability to perform aggressive feature selection within model training. Finally, SHAP values were used to interpret cellular biology underpinning model predictions (43). SHAP values denote the relative importance of a given feature in driving a model's prediction – this method has been used to explain machine learning predictions in prior cancer studies (38, 61, 62).

Machine learning models classify αCD40-treated TMEs as having reduced T cell exhaustion phenotypes

To reveal the impact of αCD40 therapy on T cell exhaustion phenotype, we first trained four EN classifier models – one per histopathologic annotation (**Fig. 1B**; T, IA, TAS, and NAP) – to predict the treatment status of the tissue. All models, regardless of histopathologic site, performed well, as measured by the accuracy, F1 score, and area under the receiver operating characteristic curve (AUC) for test sets of each of the models (**Fig. 3A** and **B**). Across the four models, accuracy ranged from 0.83 to 0.85, F1 score ranged from 0.73 to 0.89, and AUC ranged from 0.87 to 0.90. As models were trained to differentiate treatment-naive from αCD40-treated PDAC, high performance of all four models indicates that αCD40 modulates all types of histopathologic regions across the TME evaluated herein.

To identify which combinations of features drove model predictions, and thus reveal how αCD40 therapy impacted T cells in the PDAC TME, we calculated SHAP values for each of the four models (**Supplementary Fig. S2A**). The top 30 weighted features out of 1,252 features in total accounted for the majority of feature importance according to SHAP values (T model: 84%; IA model: 74%; TAS model: 87%; NAP model: 92%), while remaining features exhibited limited impact on the models. Comparison of the top 15 features driving model predictions for each of the four histopathologic models revealed that 13 features were top contributors across multiple models (**Fig. 3C**), indicating some amount of shared T cell densities, differentiation states, and spatial organizations across

histopathologic sites within a given treatment cohort. To further bolster the machine learning results, we compared the normalized values for each of the top features detected by SHAP analysis between treatment-naive samples versus αCD40-treated samples within each histopathologic site (**Supplementary Fig. S2B**, **C**, **D**, and **E**). Following correction for multiple hypothesis testing, all 15 features derived from the T model were significantly different between treatment cohorts, 14 of 15 features derived from the IA and TAS models were significantly different between treatment cohorts, and 9 of 15 features derived from the NAP models were significantly different between treatment cohorts. Given that NAP sites had the fewest number of ROIs present in the data, it is unsurprising that fewer features were statistically significant.

Overall, the models identified αCD40-treated TMEs as containing increased densities of mesenchymal fibroblast-like cells and several T cell states, including three $CD4^+$ T helper populations and two antigen-experienced $CD8^+$ T cell populations (T_{EX} and $CD44^+$ T_{OTHER}) (**Fig. 3C**, **Supplementary Fig. S2B, C, D,** and **E**), as compared to treatment-naïve TMEs, which contained increased densities of naive $CD8^+$ T cells (although not significantly different) and B cells. In addition to cell state densities, analysis of T cell functionality barcodes revealed that αCD40-treated TMEs contained increased densities of T cells expressing combinations of T-BET, CD44, CD39, TIM3, and TCF-1 (**Fig. 3C**, **Supplementary Fig. S2B, C, D,** and **E**). On the other hand, treatment-naive TMEs contained increased densities of T cells expressing combinations of TOX1 and EOMES, concordant with mIHC stained tissue images (**Fig. 3D**). Finally, spatial interactions involving $CD4^+$ Th1 cells were more likely identified within the αCD40-treated cohort,

whereas interactions involving myeloid cells, naive T_{REGs} (not significantly different), and Ki-67$^+$ neoplastic epithelial cells were more likely to be associated with treatment-naive tissue (**Fig. 3C**, **Supplementary Fig. S2B, C, D,** and **E**). Altogether, these results indicate αCD40 TMEs contained increased presence of T cells in close spatial proximity to one another – in particular, CD4$^+$ T helper cells – with reduced exhaustion profiles, as compared to treatment-naive TMEs.

Of the top features across all four models, the majority of features were densities of T cell functionality barcodes. As all barcodes present on any T cell (regardless of the T cell state) were provided to the machine learning models, we sought to understand the types of T cells expressing each of the predictive barcodes to determine whether there were patterns in the types and proportions of T cell states expressing each barcode. We ensured that only T cells within regions of the histopathologic site the predictive model was derived from were counted, as well as from the treatment cohort the barcoded T cell was predictive of. We then correlated barcodes based off of the types and proportions of T cell states expressing each barcode (**Fig. 3E**). Barcodes expressed by similar proportions of the same T cells were highly correlated and appear adjacent to each other in the heatmap. This analysis resulted in four clusters (i. – iv.) of barcodes, each distinct in types of T cells expressing them, and unrelated to histopathologic site, indicating that barcodes expressed by similar T cells exist across the TME. Barcodes belonging to cluster (i) were expressed by antigen-inexperienced (as defined by a lack of CD44 expression) CD8$^+$ T cells, antigen-inexperienced CD4$^+$ T helper cells, naive T_{REGs}, and mT_{REGs}. However, barcodes in cluster (i) ranged from TOX1$^+$ and EOMES$^+$ expression

profiles when their increased densities were predictive of treatment-naive, to CD39$^+$ TIM3$^+$, and TCF-1$^+$ expression profiles when their increased densities were predictive of αCD40 therapy. This result supports the notion that, while the same T cell types were present regardless of therapy exposure, their functional capacity differed following αCD40 treatment. Higher densities of barcodes in clusters (ii), (iii), and (iv) were all predictive of αCD40 therapy and included combinations of T-BET$^+$, TIM3$^+$, TCF-1$^+$, and CD44$^+$. These barcoded cells were expressed by distinct groups of T cell states, including multiple antigen-experienced CD4$^+$ Th1 cell states, as well as T-BET$^+$ T_{REGs}, which have been reported to be similar to CD4$^+$ Th1 cells in their function (63).

Machine learning model classifies long disease-free survivors as having more T cell effector functionality following αCD40 therapy

The clinical trial from which the αCD40-treated specimens were derived was not designed to assess correlates with survival. However, we hypothesized that we could train machine learning models to accurately predict DFS for these patients, with the ultimate goal of identifying which combinations of TME features were associated with long versus short DFS. In contrast to the αCD40-treated patients who all received the same adjuvant treatment regimen (αCD40 therapy and chemotherapy), the patients from the treatment-naive cohort went on to receive varying adjuvant therapies. Thus, we did not train models to predict DFS for the treatment-naive cohort, as identifying the underlying biology driving improved survival for these patients would be challenging. Therefore, we trained EN classifier models to predict long or short DFS for tissue regions only from patients treated with αCD40 therapy. The median DFS timepoint (9.8 months) across all patients in the

αCD40-treated cohort was used to segregate long and short disease-free survivors. Again, separate models were built for regions annotated as each histopathologic site, including T, IA, and TAS. There were too few NAP regions to build a model assessing DFS from the αCD40-treated patients for this histopathologic site. Only the model trained from IA regions performed well in predicting both long and short DFS, with an accuracy of 0.81, F1 score of 0.88, and AUC of 0.77 (**Fig. 4A** and **B**).

To identify which combinations of features drove predictions for the IA-derived model, and thus hypothesize potential mechanisms contributing to improved DFS following αCD40 therapy, we followed a similar model interpretation analysis as described above. SHAP values were calculated to highlight feature importance (**Supplementary Fig. S3A**, **Fig. 4C**), and the top 30 features out of 1,252 features fed into the model accounted for 78% of feature importance. All of the top 15 features detected by the SHAP analysis for the IA-derived model were significantly different between DFS groups (**Supplementary Fig. S3B**), thus demonstrating how machine learning can be used to reveal potential combinations of candidate biomarkers of DFS in the PDAC TME.

Of note, an increased density of $CD44^+$ $CD4^+$ Th1 cells was observed in IA regions from patients with long DFS, as compared to those with from patients with short DFS (**Fig. 4C**, **Supplementary Fig. S3B**). In addition, we found increased spatial interactions between $CD4^+$ Th1 T_{EM} cells or $CD8^+$ T_{EMRA} cells and T-BET^+ T_{REGs} to be associated with long DFS rather than short DFS (**Fig. 4C**, **Supplementary Fig. S3B**). Interestingly, of the three types of TME features, densities of T cell functionality barcodes were the most common

feature predictive of DFS, accounting for 12 of the top 15 features. Eight of these barcode densities were associated with short DFS, while the remaining four were associated with long DFS (**Fig. 4C**, **Supplementary Fig. S3B**). A number of biomarkers segregated based on DFS status (**Fig. 4C**, **D**); namely, TOX1 was expressed across all eight barcodes whose increased densities were associated with short DFS, and PD-1 expression was found exclusively in five of the eight barcodes whose increased densities were associated with short DFS. In contrast, expression of CD44, CD38, CD39, TIM3, and LAG-3 were unique to the four barcodes whose increased densities were associated with long DFS (**Fig. 4C**, **D**).

To identify whether the types and amounts of T cell states expressing each of the predictive barcodes were similar, we correlated the barcodes based off of the proportions of T cells expressing each of them (**Fig. 4E**). We found four distinct clusters of barcodes, and within each cluster, the barcodes were expressed by similar types of T cell states and in similar proportions. All but one of the barcodes in clusters (i) and (ii) were among the features whose increased densities were associated with short DFS and were expressed by (i) antigen-inexperienced $CD8^+$ T cells, antigen-inexperienced $CD4^+$ T helper cells, naive T_{REGs}, and mT_{REGs}; and (ii) antigen-inexperienced $CD8^+$ T cells and $CD4^+$ Th1 cells, as well as T-BET^+ T_{REGs}. In contrast, increased densities of all barcodes in clusters (iii) and (iv) were associated with long DFS. Cluster (iii) consisted of one barcode that was uniquely expressed by $CD8^+$ T_{EM} and T_{EMRA} cells, $CD44^+$ $CD4^+$ T helper cells, as well as naive T_{REG} cells. Finally, cluster (iv) barcodes were expressed by $CD44^+$ $CD8^+$ T cells, $CD4^+$ Th1 T_{EM} and T_{EMRA} cells, $CD44^+$ $CD4^+$ Th1 cells, and T-BET^+ T_{REGs}. In summary,

these findings indicate αCD40 therapy stimulates an anti-tumor T cell response, characterized by presence of $CD44^+$ T cells, in particular $CD4^+$ Th1 cells, and is associated with prolonged DFS time within IAs.

Cellular neighborhood analysis identifies spatial organization of T cells to correlate with DFS following αCD40 therapy

The majority of top TME feature types driving the αCD40 DFS IA model predictions were presence of specific barcoded T cells, supporting the notion that these T cell subsets likely play a major role in extending DFS. However, the spatial organization of the specific barcoded T cells identified by the machine learning analyses remained unknown, as the spatial interaction features did not account for T cell functionality barcodes. TME spatial architecture is associated with clinical outcomes across cancer types (24-27, 31); thus, we aimed to identify the spatial neighbors of the top barcoded T cells whose densities were associated with DFS to better understand their potential role in prolonging DFS following αCD40 therapy within IA regions.

To quantify the spatial organization of the tissue, we performed a recurrent cellular neighborhood (RCN) analysis across all IA regions within the αCD40-treated cohort (26, 64). Here, we established a 60 μm radius (47-50) around every cell as its neighborhood and identified all cells within that neighborhood (**Fig. 5A**). We then clustered all cells according to the cellular neighborhoods' compositions (**Methods**). This resulted in seven RCNs (**Supplementary Fig. S4A**) – each one representing spatial neighborhoods present across multiple IAs that were distinct in proportions and types of cell states

located within the neighborhood. The average cellular composition of each RCN is shown (**Fig. 5B**). We confirmed that no single RCN dominated the IA regions analyzed (**Supplementary Fig. S4B** and **C**) and that no RCN was exclusively derived from any single IA region or patient (**Supplementary Fig. S4D** and **E**). Upon viewing the scatterplot reconstructions of regions, clearly defined spatial patterns within IAs were revealed (**Fig. 5C**, **Supplementary Fig. S4F**). For example, cells in RCN1, whose neighborhood consisted of majority B cells, were often found to be spatially clustered together, potentially representing “germinal center”-like pockets within IA regions.

Given that our goal was to identify neighbors surrounding the top barcoded T cells from the αCD40 DFS model, we first identified which of the seven RCNs the barcoded T cells were assigned to. We then assessed whether there was a relationship between spatial organization of the barcoded T cells and clinical outcome by comparing the RCNs of barcoded T cells from patients with long DFS versus the RCNs of barcoded T cells from patients with short DFS. We performed unsupervised clustering of barcoded T cells from long and short DFS patients together based on proportions of the seven RCNs the barcoded T cells resided in (**Fig. 5D**). This resulted in two distinct clusters based on which RCNs the barcoded T cells resided in; the clusters also separated barcoded T cells from patients associated with long DFS versus short DFS. Cluster 1 (C1) included all barcoded T cells from patients with long DFS, as well as $CD44^{+}$ $T\text{-}BET^{+}$ barcoded T cells from patients with short DFS. Cluster 2 (C2) consisted of all remaining barcoded T cells from patients with short DFS.

The most striking difference between the two clusters was proportions of barcoded T cells residing in RCN5 (**Fig. 5E**). Of all RCNs, RCN5 contained the greatest proportion of $CD44^+$ T cells, spanning both $CD8^+$ T cells and $CD4^+$ T helper lineages (**Fig. 5B**). 45% of T cells in C1 (long DFS) resided in RCN5, whereas only 3% of T cells from C2 (short DFS) resided in RCN5 (**Fig. 5E**). Given that C1 consisted of T cells from patients with long DFS and C2 consisted of T cells from patients with short DFS, our results highlight a relationship between cellular spatial organization and clinical outcome. Specifically, T cells correlated with long DFS were frequently found to be surrounded by $CD44^+$ T cells, thus supporting the hypothesis that αCD40 therapy promotes T cell priming and/or recruitment of primed T cells to PDAC TMEs.

Finally, to further elucidate potential cellular mechanisms at play within various RCNs, we calculated proportions of T cells expressing Ki-67 or GrzB in each RCN and compared values to the overall proportion of $Ki\text{-}67^+$ or $GrzB^+$ T cells across all αCD40 IA regions. Given our prior findings that the majority of T cell barcodes whose increased density correlated with long DFS were assigned to RCN5 (**Fig. 5E**), we hypothesized that T cells assigned to RCN5 would possess increased proliferative and/or cytotoxic capabilities. We found a larger proportion of T cells expressing Ki-67 residing in RCN1 and RCN5 as compared to the overall T cell population (dashed line) (**Fig. 5F**). In addition, we found a larger proportion of T cells (excluding T_{REGs}) expressing GrzB residing in RCN5, RCN6, and RCN7, as compared to the overall non-T_{REG} T cell population (dashed line) (**Fig. 5G**). However, raw counts of $GrzB^+$ T cells in RCN6 and RCN7 were low (RCN6: n=8 cells; RCN7: n=11 cells), whereas RCN5 contained the highest level of $GrzB^+$ T cells across all

RCNs (n=168). Visualization of a representative mIHC image depicts presence of $GrzB^+$ T cells localized to RCN5 in an IA region from a patient with long DFS (**Fig. 5H**). Collectively, these results provide further support that T cells within RCN5 are likely activated and possess an effector phenotype capable of an anti-tumor cytotoxic response.

DISCUSSION

In this study, we advance spatial proteomic imaging technology and leverage machine learning approaches to understand the role of T cell phenotypes and spatial organization in the complex TME of human pancreatic cancer. In contrast to previous single-cell spatial proteomic studies, which often group T cells together as broad populations, such as $CD8^+$ T cells, $CD4^+$ T cells, and T_{REGs} (23, 25, 65-67), our novel mIHC panel was curated to phenotype T cells as one of 18 distinct states along with functionality status from 10 different markers, all while preserving the spatial orientation of each cell in the TME. In considering the full spectrum of T cell states in addition to their spatial organization within the TME, the data became increasingly complex, highlighting the need for quantitative analyses that consider integration of all features together, rather than one-off correlations which fail to represent intertwining biological mechanisms at play. We leveraged machine learning, as the models detect combinations and weights of tissue features associated with a given output, such as treatment status or DFS, and thus it is an appropriate and powerful tool for interrogating TME complexity. Through our machine learning approaches we identified TME features most associated with αCD40 therapy exposure or prolonged DFS out of the >1000 features that we measured. This study demonstrates the value of merging single-cell spatial proteomic assays with machine learning analyses to interrogate how immunotherapy modulates the PDAC TME and drives improved survival from a holistic perspective.

Despite the multitude of unique T cell states identified herein, our machine learning models were able to identify T cell subsets associated with anti-tumor characteristics and

prolonged DFS. Consistent with our preclinical studies revealing that $CD4^+$ T cells are a major contributor to PDAC immunity following αCD40 therapy (8), our machine learning models revealed that αCD40-treated patient tumors contain increased densities of effector memory cells specifically within the $CD4^+$ Th1 lineage. Along the T cell spectrum, T_{EM} cells are fully functional with some self-renewal capacities (68-70), and mediate potent anti-tumor immunity (71). No increase was observed in $CD8^+$ memory T cell populations, supporting the notion that αCD40 therapy promotes immunological memory from the $CD4^+$ T cell lineage in both mouse and human PDAC tissue. Our models also identified antigen-experienced $CD4^+$ Th1 helper cells as the main cell type whose density associated with prolonged DFS following αCD40 therapy. This result is supported by two independent studies, including characterization of immune cells in biopsied PDAC liver metastases following CD40 agonism (72), and the second investigating primary resected PDAC TMEs after treatment with a granulocyte-macrophage colony-stimulating factor-secreting allogenic PDAC vaccine (GVAX) (rather than αCD40 therapy) (73). Both studies reported that presence of $CD4^+$ T helper cells contribute to improved survival following immunotherapy in PDAC (72, 73). Here, we further characterized expression features of the $CD4^+$ T helper cells as $CD44^+$ Th1 cells, which correlated with improved outcomes. Reports have also highlighted the direct role of $CD4^+$ T cells in mediating anti-tumor immunity, including via cytotoxicity (74) and production of effector cytokines like interferon-γ and tumor necrosis factor-α (75, 76). As such, we hypothesize that future therapies designed to harness effector and memory functions of $CD4^+$ T helper cells following administration of αCD40 therapy may be clinically beneficial.

In addition to investigating presence of various T cell states, our machine learning analyses also shed light on localization and spatial organization of T cells within PDAC TMEs related to prolonged survival following αCD40 treatment. High performance of the IA-derived DFS model, coupled with poor performance of the T and TAS-derived DFS models, supports the notion that IAs are a major site of αCD40-induced immune response contributing to prolonged DFS. We previously reported an increase in number of IAs following αCD40 treatment in PDAC-bearing mice (77), and in the aforementioned GVAX study, survival was linked to increased $CD4^+$ T helper pathway genes specifically within IAs (and not tumor regions) (73). Additionally, a recent study found the enrichment of gene signatures representing mature tertiary lymphoid structures in pre-treatment PDACs associated with improved survival in patients following treatment with varying chemoimmunotherapies (78). Our RCN analyses further revealed that the key T cells associated with prolonged DFS were often surrounded by antigen-experienced $CD8^+$ T cells and $CD4^+$ T helper cells, as well as a higher proportion of proliferating and cytotoxic T cells, as compared to all T cells regardless of spatial neighborhood. Collectively, the results indicate IAs may function as sites of T cell priming or second signal, promoting T cell activation and function in PDAC TMEs, contributing to prolonged DFS following multiple types of immunotherapies.

Our interrogation of IAs also revealed T cell features correlating with short DFS following αCD40 therapy, identifying T cell states that are concordant with dysfunctional tumor-infiltrating T cell phenotypes. $TOX1^+$ T cells are at the far end of the exhausted T cell spectrum (14, 79), and TOX1 expression correlates with PD-1 on T cells and impaired

immunotherapy response in hepatocellular carcinoma (80). Correspondingly, we observed that expression of TOX1 and/or PD-1 on $CD8^+$ T cells and $CD4^+$ T helper cells associated with shorter DFS following αCD40 therapy. Further, T cells linked to short DFS expressing TOX1 and/or PD-1 were largely $CD44^-$ T cells, which may represent a population of antigen-naïve T cells that have aberrantly upregulated these markers, or could potentially represent T cells that have become terminally exhausted and differentiated due to repeated T cell receptor stimulation (and thus downregulated CD44 expression) (81). We also found increased presence of $TOX1^+$ T cells within treatment-naive TMEs, indicating a baseline terminally exhausted T cell phenotype in PDAC. Interestingly, despite the presence of $TOX1^+$ exhausted T cells within treatment-naive TMEs, we did not identify abundant expression of PD-1^+ T cells in treatment-naive TMEs, in contrast to other tumors, such as melanoma (82), where PD-1^+ T cells are abundant in TMEs. The paucity of PD-1^+ T cells in PDAC TMEs could be a contributing factor to the failure of ICBs targeting PD-1 or PD-L1 in the vast majority of patients with PDAC (83). Together, our data support the conclusion that TOX1, but not PD-1, is a dominant feature of exhausted T cells in PDAC. As such, therapies that modulate $TOX1^+$ T cells in the TME – such as αCD40 agonism in this study – may improve clinical outcomes for patients with PDAC. An overview of the main TME features detected by our machine learning models in this study are visually described (**Fig. 6**).

Notably, the dataset we used to conduct this study was unique in several aspects – including therapy administered, mIHC panel used, and histopathologic sites assayed – making absolute validation of our results challenging and highlighting the need for

additional studies on larger cohorts to address the potential of building a model capable of more generalized predictions. Patient samples were collected from multiple institutions per treatment cohort, yet our machine learning models were still able to accurately classify patient samples according to therapy. This suggests any institutional or technical differences in tissue processing were not driving features in model predictions. Importantly, the machine learning models we trained performed comparably to or better than several other models derived from similar studies (36, 38, 84-88). Additionally, our biological conclusions on impacts of αCD40 are concordant with several prior studies (8, 14, 72, 73, 77, 79, 80, 83), providing further support for our methods and findings. Future antibody panels may incorporate additional markers, such as chemokine receptors, to further characterize key T cell subsets, or additional cell lineage markers, such as myeloid cell markers (89), to further phenotype cell-cell interactions. It should be noted that in our study, treatment with αCD40 did not prolong DFS as compared to the treatment-naive cohort, and similar machine learning analyses on data from clinical trials that did improve outcome will be useful to validate our conclusions where the patient cohort size is better powered for survival analyses. Finally, tumors were resected 12 days after αCD40 administration, so it is possible that the T cells involved in prolonged DFS did not have sufficient time to transit beyond IAs and into surrounding TMEs following priming. Further analyses investigating timing of T cell trafficking into various sites within PDAC TMEs are necessary to determine if analysis of T or TAS regions sampled at later timepoints following treatment could be used to assess clinical outcome for these patients.

This study provides proof-of-principle for leveraging computational approaches to evaluate highly multiplexed cancer datasets and supports the notion that similar analytic approaches could be utilized in future studies to identify important, and otherwise inconspicuous alterations in TMEs correlating with patient treatment or response. Future studies could expand upon these findings to target pathways identified via this approach to benefit patients who do not respond to current treatment strategies.

ACKNOWLEDGEMENTS

The authors thank Drs. David L. Bajor, E. Gabriela Chiorean, Daniel A. Laheru, and Mark H. O'Hara for efforts as site investigators for the neoadjuvant selicrelumab (CD40 agonist) clinical trial. We also thank John Wherry for helpful discussion related to panel design and marker selection. This research was supported by the National Cancer Institute (NCI) of the National Institutes of Health grants T32CA254888 (K.E.B.), P50 CA127003 (J.A.N.), R01 CA248857 (J.A.N.), R01 CA205406 (J.A.N.), R01 CA169141 (J.A.N.), R35 CA197735 (J.A.N.), U01 CA250549 (J.A.N.), U24CA231877 (J.G.), and U2CCA233280 (J.G.), the DFCI Hale Family Center for Pancreatic Cancer Research (J.A.N. and B.M.W.), the Lustgarten Foundation Dedicated Laboratory program (J.A.N., B.M.W.), the Parker Institute for Cancer Immunotherapy (R.H.V. and K.T.B.), the Brenden-Colson Center for Pancreatic Care (L.M.C., S.S., C.B.B., K.T.B., N.K.), the Robert L. Fine Cancer Research Foundation (K.T.B.), funding from the Prospect Creek Foundation to the OHSU SMMART (Serial Measurement of Molecular and Architectural Responses to Therapy) Program (J.G.), and a generous startup package from the Knight Cancer Institute and the Brenden-Colson Center for Pancreatic Care (K.T.B.).

AUTHOR CONTRIBUTIONS

Conceptualization: K.E.B., J.G., L.M.C., K.T.B.

Formal analysis: K.E.B., S.S., C.B.B., B.T.

Funding acquisition: J.G., L.M.C., K.T.B.

Investigation: K.E.B., S.S., C.B.B., K.B., N.K., E.E.F., A.D.C., J.A.N.

Methodology: K.E.B., S.S., C.B.B., K.B., N.K., B.T., J.G., L.M.C., K.T.B.

Resources: R.H.V., B.M.W., J.G., L.M.C., K.T.B.

Supervision: J.G., L.M.C., K.T.B.

Visualization: K.E.B., S.S., N.K.

Writing – original draft: K.E.B., S.S., J.G., L.M.C., K.T.B.

Writing – review and editing: all authors.

CONFLICT OF INTEREST

R.H.V. is an inventor on licensed patents relating to cancer cellular immunotherapy and cancer vaccines, and mutant Kras specific T cell receptors; has received consulting fees from BMS; and receives royalties from Children's Hospital Boston for a licensed research-only monoclonal antibody and from the University of Pennsylvania for licensed research cell lines. J.A.N. receives consulting fees from Leica Biosystems and research support from Natera. B.M.W. receives research funding from AstraZeneca, Celgene/BMS, Eli Lilly, Novartis, and Revolution Medicines, and consulting for Celgene, GRAIL, Ipsen, Mirati, Third Rock Ventures unrelated to the current work. C.B.B. is an employee of, and holds equity in, Akoya Biosciences, Inc. K.T.B. receives royalties from the University of Pennsylvania for licensed research cell lines and has received consulting fees from Guidepoint. L.M.C. has received reagent support from Cell Signaling Technologies, Syndax Pharmaceuticals, Inc., ZielBio, Inc., and Hibercell, Inc.; holds sponsored research agreements with Syndax Pharmaceuticals, Hibercell, Inc., Prospect Creek Foundation, Lustgarten Foundation for Pancreatic Cancer Research, Susan G. Komen Foundation,

and the National Foundation for Cancer Research; is on the Advisory Board for Carisma Therapeutics, Inc., CytomX Therapeutics, Inc., Kineta, Inc., Hibercell, Inc., Cell Signaling Technologies, Inc., Alkermes, Inc., Raska Pharma, Inc., NextCure, Guardian Bio, AstraZeneca Partner of Choice Network (OHSU Site Leader), Genenta Sciences, Pio Therapeutics Pty Ltd., and Lustgarten Foundation for Pancreatic Cancer Research Therapeutics Working Group, Inc.

REFERENCES

1. Pishvaian MJ, Blais EM, Brody JR, Lyons E, DeArbeloa P, Hendifar A*, et al.* Overall survival in patients with pancreatic cancer receiving matched therapies following molecular profiling: a retrospective analysis of the Know Your Tumor registry trial. Lancet Oncol **2020**;21(4):508-18.
2. Siegel RL, Miller KD, Fuchs HE, Jemal A. Cancer statistics, 2022. CA Cancer J Clin **2022**;72(1):7-33.
3. Hosein AN, Dougan SK, Aguirre AJ, Maitra A. Translational advances in pancreatic ductal adenocarcinoma therapy. Nat Cancer **2022**;3(3):272-86.
4. Byrne KT, Betts CB, Mick R, Sivagnanam S, Bajor DL, Laheru DA*, et al.* Neoadjuvant Selicrelumab, an Agonist CD40 Antibody, Induces Changes in the Tumor Microenvironment in Patients with Resectable Pancreatic Cancer. Clin Cancer Res **2021**;27(16):4574-86.
5. Rojas LA, Sethna Z, Soares KC, Olcese C, Pang N, Patterson E*, et al.* Personalized RNA neoantigen vaccines stimulate T cells in pancreatic cancer. Nature **2023**;618(7963):144-50.
6. Vonderheide RH. The Immune Revolution: A Case for Priming, Not Checkpoint. Cancer Cell **2018**;33(4):563-9.
7. Vonderheide RH. CD40 Agonist Antibodies in Cancer Immunotherapy. Annu Rev Med **2020**;71:47-58.
8. Morrison AH, Diamond MS, Hay CA, Byrne KT, Vonderheide RH. Sufficiency of CD40 activation and immune checkpoint blockade for T cell priming and tumor immunity. Proc Natl Acad Sci U S A **2020**;117(14):8022-31.

9. Baaten BJ, Tinoco R, Chen AT, Bradley LM. Regulation of Antigen-Experienced T Cells: Lessons from the Quintessential Memory Marker CD44. Front Immunol **2012**;3:23.

10. Gattinoni L, Klebanoff CA, Restifo NP. Paths to stemness: building the ultimate antitumour T cell. Nat Rev Cancer **2012**;12(10):671-84.

11. Oliveira G, Wu CJ. Dynamics and specificities of T cells in cancer immunotherapy. Nat Rev Cancer **2023**;23(5):295-316.

12. Kao C, Oestreich KJ, Paley MA, Crawford A, Angelosanto JM, Ali MA*, et al.* Transcription factor T-bet represses expression of the inhibitory receptor PD-1 and sustains virus-specific CD8+ T cell responses during chronic infection. Nat Immunol **2011**;12(7):663-71.

13. Wang Y, Hu J, Li Y, Xiao M, Wang H, Tian Q*, et al.* The Transcription Factor TCF1 Preserves the Effector Function of Exhausted CD8 T Cells During Chronic Viral Infection. Front Immunol **2019**;10:169.

14. Khan O, Giles JR, McDonald S, Manne S, Ngiow SF, Patel KP*, et al.* TOX transcriptionally and epigenetically programs CD8(+) T cell exhaustion. Nature **2019**;571(7764):211-8.

15. Wherry EJ, Ha SJ, Kaech SM, Haining WN, Sarkar S, Kalia V*, et al.* Molecular signature of CD8+ T cell exhaustion during chronic viral infection. Immunity **2007**;27(4):670-84.

16. Wherry EJ. T cell exhaustion. Nat Immunol **2011**;12(6):492-9.

17. Huang AC, Orlowski RJ, Xu X, Mick R, George SM, Yan PK*, et al.* A single dose of neoadjuvant PD-1 blockade predicts clinical outcomes in resectable melanoma. Nat Med **2019**;25(3):454-61.

18. Pauken KE, Sammons MA, Odorizzi PM, Manne S, Godec J, Khan O*, et al.* Epigenetic stability of exhausted T cells limits durability of reinvigoration by PD-1 blockade. Science **2016**;354(6316):1160-5.

19. Schietinger A, Philip M, Krisnawan VE, Chiu EY, Delrow JJ, Basom RS*, et al.* Tumor-Specific T Cell Dysfunction Is a Dynamic Antigen-Driven Differentiation Program Initiated Early during Tumorigenesis. Immunity **2016**;45(2):389-401.

20. Chu Y, Dai E, Li Y, Han G, Pei G, Ingram DR*, et al.* Pan-cancer T cell atlas links a cellular stress response state to immunotherapy resistance. Nat Med **2023**;29(6):1550-62.

21. Zheng L, Qin S, Si W, Wang A, Xing B, Gao R*, et al.* Pan-cancer single-cell landscape of tumor-infiltrating T cells. Science **2021**;374(6574):abe6474.

22. Zhang H, AbdulJabbar K, Moore DA, Akarca A, Enfield KSS, Jamal-Hanjani M*, et al.* Spatial Positioning of Immune Hotspots Reflects the Interplay between B and T Cells in Lung Squamous Cell Carcinoma. Cancer Res **2023**;83(9):1410-25.

23. Karimi E, Yu MW, Maritan SM, Perus LJM, Rezanejad M, Sorin M*, et al.* Single-cell spatial immune landscapes of primary and metastatic brain tumours. Nature **2023**;614(7948):555-63.

24. Jackson HW, Fischer JR, Zanotelli VRT, Ali HR, Mechera R, Soysal SD*, et al.* The single-cell pathology landscape of breast cancer. Nature **2020**;578(7796):615-20.

25. Keren L, Bosse M, Marquez D, Angoshtari R, Jain S, Varma S*, et al.* A Structured Tumor-Immune Microenvironment in Triple Negative Breast Cancer Revealed by Multiplexed Ion Beam Imaging. Cell **2018**;174(6):1373-87 e19.

26. Blise KE, Sivagnanam S, Banik GL, Coussens LM, Goecks J. Single-cell spatial architectures associated with clinical outcome in head and neck squamous cell carcinoma. NPJ Precis Oncol **2022**;6(1):10.

27. Farkkila A, Gulhan DC, Casado J, Jacobson CA, Nguyen H, Kochupurakkal B*, et al.* Immunogenomic profiling determines responses to combined PARP and PD-1 inhibition in ovarian cancer. Nat Commun **2020**;11(1):1459.

28. Enfield KSS, Martin SD, Marshall EA, Kung SHY, Gallagher P, Milne K*, et al.* Hyperspectral cell sociology reveals spatial tumor-immune cell interactions associated with lung cancer recurrence. J Immunother Cancer **2019**;7(1):13.

29. Gide TN, Silva IP, Quek C, Ahmed T, Menzies AM, Carlino MS*, et al.* Close proximity of immune and tumor cells underlies response to anti-PD-1 based therapies in metastatic melanoma patients. Oncoimmunology **2020**;9(1):1659093.

30. Giraldo NA, Nguyen P, Engle EL, Kaunitz GJ, Cottrell TR, Berry S*, et al.* Multidimensional, quantitative assessment of PD-1/PD-L1 expression in patients with Merkel cell carcinoma and association with response to pembrolizumab. J Immunother Cancer **2018**;6(1):99.

31. Barua S, Fang P, Sharma A, Fujimoto J, Wistuba I, Rao AUK*, et al.* Spatial interaction of tumor cells and regulatory T cells correlates with survival in non-small cell lung cancer. Lung Cancer **2018**;117:73-9.

32. Mi H, Sivagnanam S, Betts CB, Liudahl SM, Jaffee EM, Coussens LM*, et al.* Quantitative Spatial Profiling of Immune Populations in Pancreatic Ductal Adenocarcinoma Reveals Tumor Microenvironment Heterogeneity and Prognostic Biomarkers. Cancer Res **2022**;82(23):4359-72.

33. Tsujikawa T, Kumar S, Borkar RN, Azimi V, Thibault G, Chang YH*, et al.* Quantitative Multiplex Immunohistochemistry Reveals Myeloid-Inflamed Tumor-Immune Complexity Associated with Poor Prognosis. Cell Rep **2017**;19(1):203-17.

34. Banik G, Betts CB, Liudahl SM, Sivagnanam S, Kawashima R, Cotechini T*, et al.* High-dimensional multiplexed immunohistochemical characterization of immune contexture in human cancers. Methods Enzymol **2020**;635:1-20.

35. Liudahl SM, Betts CB, Sivagnanam S, Morales-Oyarvide V, da Silva A, Yuan C*, et al.* Leukocyte Heterogeneity in Pancreatic Ductal Adenocarcinoma: Phenotypic and Spatial Features Associated with Clinical Outcome. Cancer Discov **2021**;11(8):2014-31.

36. Risom T, Glass DR, Averbukh I, Liu CC, Baranski A, Kagel A*, et al.* Transition to invasive breast cancer is associated with progressive changes in the structure and composition of tumor stroma. Cell **2022**;185(2):299-310 e18.

37. Kim DW, Lee S, Kwon S, Nam W, Cha IH, Kim HJ. Deep learning-based survival prediction of oral cancer patients. Sci Rep **2019**;9(1):6994.

38. Buk Cardoso L, Cunha Parro V, Verzinhasse Peres S, Curado MP, Fernandes GA, Wunsch Filho V*, et al.* Machine learning for predicting survival of colorectal cancer patients. Sci Rep **2023**;13(1):8874.

39. Sorin M, Rezanejad M, Karimi E, Fiset B, Desharnais L, Perus LJM*, et al.* Single-cell spatial landscapes of the lung tumour immune microenvironment. Nature **2023**;614(7948):548-54.

40. Carpenter AE, Jones TR, Lamprecht MR, Clarke C, Kang IH, Friman O*, et al.* CellProfiler: image analysis software for identifying and quantifying cell phenotypes. Genome Biol **2006**;7(10):R100.

41. Pedregosa F, Varoquaux G, Gramfort A, Michel V, Thirion B, Grisel O*, et al.* Scikit-learn: Machine Learning in Python. JMLR **2011**;12:2825-30.

42. Chawla NV, Bowyer KW, Hall LO, Kegelmeyer WP. SMOTE: Synthetic Minority Over-sampling Technique. JAIR **2002**;16:321-57.

43. S.M. L, S. L. A Unified Approach to Interpreting Model Predictions. NIPS **2017**:4765-74.

44. Carstens JL, Correa de Sampaio P, Yang D, Barua S, Wang H, Rao A*, et al.* Spatial computation of intratumoral T cells correlates with survival of patients with pancreatic cancer. Nat Commun **2017**;8:15095.

45. Gartrell RD, Enzler T, Kim PS, Fullerton BT, Fazlollahi L, Chen AX*, et al.* Neoadjuvant chemoradiation alters the immune microenvironment in pancreatic ductal adenocarcinoma. Oncoimmunology **2022**;11(1):2066767.

46. Siret C, Collignon A, Silvy F, Robert S, Cheyrol T, Andre P*, et al.* Deciphering the Crosstalk Between Myeloid-Derived Suppressor Cells and Regulatory T Cells in Pancreatic Ductal Adenocarcinoma. Front Immunol **2019**;10:3070.

47. Busse D, de la Rosa M, Hobiger K, Thurley K, Flossdorf M, Scheffold A*, et al.* Competing feedback loops shape IL-2 signaling between helper and regulatory T

lymphocytes in cellular microenvironments. Proc Natl Acad Sci U S A **2010**;107(7):3058-63.

48. Muller AJ, Filipe-Santos O, Eberl G, Aebischer T, Spath GF, Bousso P. CD4+ T cells rely on a cytokine gradient to control intracellular pathogens beyond sites of antigen presentation. Immunity **2012**;37(1):147-57.

49. Oyler-Yaniv A, Oyler-Yaniv J, Whitlock BM, Liu Z, Germain RN, Huse M*, et al.* A Tunable Diffusion-Consumption Mechanism of Cytokine Propagation Enables Plasticity in Cell-to-Cell Communication in the Immune System. Immunity **2017**;46(4):609-20.

50. Thibaut R, Bost P, Milo I, Cazaux M, Lemaitre F, Garcia Z*, et al.* Bystander IFN-gamma activity promotes widespread and sustained cytokine signaling altering the tumor microenvironment. Nat Cancer **2020**;1(3):302-14.

51. Virtanen P, Gommers R, Oliphant TE, Haberland M, Reddy T, Cournapeau D*, et al.* SciPy 1.0: fundamental algorithms for scientific computing in Python. Nat Methods **2020**;17(3):261-72.

52. Seabold S, Perktold J. statsmodels: Econometric and statistical modeling with python. Proceedings of the 9th Python in Science Conference **2010**.

53. Blank CU, Haining WN, Held W, Hogan PG, Kallies A, Lugli E*, et al.* Defining 'T cell exhaustion'. Nat Rev Immunol **2019**;19(11):665-74.

54. McLane LM, Abdel-Hakeem MS, Wherry EJ. CD8 T Cell Exhaustion During Chronic Viral Infection and Cancer. Annu Rev Immunol **2019**;37:457-95.

55. Chu T, Zehn D. Charting the Roadmap of T Cell Exhaustion. Immunity **2020**;52(5):724-6.

56. Philip M, Fairchild L, Sun L, Horste EL, Camara S, Shakiba M*, et al.* Chromatin states define tumour-specific T cell dysfunction and reprogramming. Nature **2017**;545(7655):452-6.

57. Canale FP, Ramello MC, Nunez N, Araujo Furlan CL, Bossio SN, Gorosito Serran M*, et al.* CD39 Expression Defines Cell Exhaustion in Tumor-Infiltrating CD8(+) T Cells. Cancer Res **2018**;78(1):115-28.

58. Davis A, Gao R, Navin NE. SCOPIT: sample size calculations for single-cell sequencing experiments. BMC Bioinformatics **2019**;20(1):566.

59. Jang IS, Neto EC, Guinney J, Friend SH, Margolin AA. Systematic assessment of analytical methods for drug sensitivity prediction from cancer cell line data. Pac Symp Biocomput **2014**:63-74.

60. Zou H, Hastie T. Regularization and variable selection via the elastic net. Journal of the Royal Statistical Society: Series B (Statistical Methodology) **2005**;67(2):301-20.

61. Moncada-Torres A, van Maaren MC, Hendriks MP, Siesling S, Geleijnse G. Explainable machine learning can outperform Cox regression predictions and provide insights in breast cancer survival. Sci Rep **2021**;11(1):6968.

62. Huang T, Le D, Yuan L, Xu S, Peng X. Machine learning for prediction of in-hospital mortality in lung cancer patients admitted to intensive care unit. PLoS One **2023**;18(1):e0280606.

63. Duhen T, Duhen R, Lanzavecchia A, Sallusto F, Campbell DJ. Functionally distinct subsets of human FOXP3+ Treg cells that phenotypically mirror effector Th cells. Blood **2012**;119(19):4430-40.

64. Schurch CM, Bhate SS, Barlow GL, Phillips DJ, Noti L, Zlobec I*, et al.* Coordinated Cellular Neighborhoods Orchestrate Antitumoral Immunity at the Colorectal Cancer Invasive Front. Cell **2020**.

65. De Vargas Roditi L, Jacobs A, Rueschoff JH, Bankhead P, Chevrier S, Jackson HW*, et al.* Single-cell proteomics defines the cellular heterogeneity of localized prostate cancer. Cell Rep Med **2022**;3(4):100604.

66. Ali HR, Jackson HW, Zanotelli VRT, Danenberg E, Fischer JR, Bardwell H*, et al.* Imaging mass cytometry and multiplatform genomics define the phenogenomic landscape of breast cancer. Nat Cancer **2020**;1(2):163-75.

67. Xiao X, Guo Q, Cui C, Lin Y, Zhang L, Ding X*, et al.* Multiplexed imaging mass cytometry reveals distinct tumor-immune microenvironments linked to immunotherapy responses in melanoma. Commun Med (Lond) **2022**;2:131.

68. Gattinoni L, Lugli E, Ji Y, Pos Z, Paulos CM, Quigley MF*, et al.* A human memory T cell subset with stem cell-like properties. Nat Med **2011**;17(10):1290-7.

69. Sallusto F, Lenig D, Forster R, Lipp M, Lanzavecchia A. Two subsets of memory T lymphocytes with distinct homing potentials and effector functions. Nature **1999**;401(6754):708-12.

70. Willinger T, Freeman T, Hasegawa H, McMichael AJ, Callan MF. Molecular signatures distinguish human central memory from effector memory CD8 T cell subsets. J Immunol **2005**;175(9):5895-903.

71. Tay RE, Richardson EK, Toh HC. Revisiting the role of CD4(+) T cells in cancer immunotherapy-new insights into old paradigms. Cancer Gene Ther **2021**;28(1-2):5-17.

72. Padron LJ, Maurer DM, O'Hara MH, O'Reilly EM, Wolff RA, Wainberg ZA*, et al.* Sotigalimab and/or nivolumab with chemotherapy in first-line metastatic pancreatic cancer: clinical and immunologic analyses from the randomized phase 2 PRINCE trial. Nat Med **2022**;28(6):1167-77.

73. Lutz ER, Wu AA, Bigelow E, Sharma R, Mo G, Soares K*, et al.* Immunotherapy converts nonimmunogenic pancreatic tumors into immunogenic foci of immune regulation. Cancer Immunol Res **2014**;2(7):616-31.

74. Sledzinska A, Vila de Mucha M, Bergerhoff K, Hotblack A, Demane DF, Ghorani E*, et al.* Regulatory T Cells Restrain Interleukin-2- and Blimp-1-Dependent Acquisition of Cytotoxic Function by CD4(+) T Cells. Immunity **2020**;52(1):151-66 e6.

75. Chen D, Varanasi SK, Hara T, Traina K, Sun M, McDonald B*, et al.* CTLA-4 blockade induces a microglia-Th1 cell partnership that stimulates microglia phagocytosis and anti-tumor function in glioblastoma. Immunity **2023**;56(9):2086-104 e8.

76. Kennedy R, Celis E. Multiple roles for CD4+ T cells in anti-tumor immune responses. Immunol Rev **2008**;222:129-44.

77. Byrne KT, Vonderheide RH. CD40 Stimulation Obviates Innate Sensors and Drives T Cell Immunity in Cancer. Cell Rep **2016**;15(12):2719-32.

78. Kinker GS, Vitiello GAF, Diniz AB, Cabral-Piccin MP, Pereira PHB, Carvalho MLR*, et al.* Mature tertiary lymphoid structures are key niches of tumour-specific immune responses in pancreatic ductal adenocarcinomas. Gut **2023**;72(10):1927-41.

79. Bengsch B, Ohtani T, Khan O, Setty M, Manne S, O'Brien S*, et al.* Epigenomic-Guided Mass Cytometry Profiling Reveals Disease-Specific Features of Exhausted CD8 T Cells. Immunity **2018**;48(5):1029-45 e5.

80. Wang X, He Q, Shen H, Xia A, Tian W, Yu W*, et al.* TOX promotes the exhaustion of antitumor CD8(+) T cells by preventing PD1 degradation in hepatocellular carcinoma. J Hepatol **2019**;71(4):731-41.

81. Abu Eid R, Ahmad S, Lin Y, Webb M, Berrong Z, Shrimali R*, et al.* Enhanced Therapeutic Efficacy and Memory of Tumor-Specific CD8 T Cells by Ex Vivo PI3K-delta Inhibition. Cancer Res **2017**;77(15):4135-45.

82. Ahmadzadeh M, Johnson LA, Heemskerk B, Wunderlich JR, Dudley ME, White DE*, et al.* Tumor antigen–specific CD8 T cells infiltrating the tumor express high levels of PD-1 and are functionally impaired. Blood **2009**;114(8):1537-44.

83. Morrison AH, Byrne KT, Vonderheide RH. Immunotherapy and Prevention of Pancreatic Cancer. Trends Cancer **2018**;4(6):418-28.

84. Iwatate Y, Hoshino I, Yokota H, Ishige F, Itami M, Mori Y*, et al.* Radiogenomics for predicting p53 status, PD-L1 expression, and prognosis with machine learning in pancreatic cancer. Br J Cancer **2020**;123(8):1253-61.

85. Jiang C, Xiu Y, Qiao K, Yu X, Zhang S, Huang Y. Prediction of lymph node metastasis in patients with breast invasive micropapillary carcinoma based on machine learning and SHapley Additive exPlanations framework. Front Oncol **2022**;12:981059.

86. Sammut SJ, Crispin-Ortuzar M, Chin SF, Provenzano E, Bardwell HA, Ma W*, et al.* Multi-omic machine learning predictor of breast cancer therapy response. Nature **2022**;601(7894):623-9.

87. Lapuente-Santana O, van Genderen M, Hilbers PAJ, Finotello F, Eduati F. Interpretable systems biomarkers predict response to immune-checkpoint inhibitors. Patterns (N Y) **2021**;2(8):100293.

88. Chowell D, Yoo SK, Valero C, Pastore A, Krishna C, Lee M*, et al.* Improved prediction of immune checkpoint blockade efficacy across multiple cancer types. Nat Biotechnol **2022**;40(4):499-506.

89. Dias Costa A, Vayrynen SA, Chawla A, Zhang J, Vayrynen JP, Lau MC*, et al.* Neoadjuvant Chemotherapy Is Associated with Altered Immune Cell Infiltration and an Anti-Tumorigenic Microenvironment in Resected Pancreatic Cancer. Clin Cancer Res **2022**;28(23):5167-79.

MAIN FIGURE LEGENDS

Figure 1. Designing a novel mIHC antibody panel to deeply phenotype T cells within the PDAC TME.

A. Overview of two PDAC cohorts assayed via mIHC.

B. Representative PDAC tissue resection stained with H&E (middle) showing four histopathologic sites annotated. Total number of regions assayed and average tissue area per histopathologic site are listed. Scale bars = 100 μm.

C. Number of regions assayed per patient. Each box represents one tissue region and is colored according to its histopathologic site.

D. 21-marker mIHC antibody panel used to assay tissue regions.

E. Representative pseudo-colored mIHC images showing T cell functionality markers with CD3 expression. Scale bars = 50 μm.

F. Cell phenotyping strategy by hierarchical gating of lineage markers and functional markers. Circles indicate colors associated with each cell state in the following figures.

Figure 2. Interrogating cell states and spatial interactions within the PDAC TME.

A. Stacked bar charts showing the average cell state densities for each treatment cohort and histopathologic site. Top row: lineage defining cells including neoplastic epithelial cells, mesenchymal fibroblast-like cells, myeloid cells, B cells, and $CD3^+$ T cells; Middle row: $CD8^+$ T cell states; Bottom row: $CD4^+$ T cell states. Columns denote histopathologic site, and each plot is further broken into treatment cohort.

B. Bar charts showing average densities of barcoded T cells for each treatment cohort and histopathologic site. Only the 15 most abundant barcodes are shown as measured by average density. Rows denote histopathologic site, and columns denote treatment cohort. Brown bars denote barcoded T cells that are in the top 15 most abundant barcodes in both cohorts. Orange bars denote barcoded T cells that are in the top 15 most abundant barcodes in the treatment-naive cohort only. Blue bars denote barcoded T cells that are in the top 15 most abundant barcodes in the αCD40-treated cohort only.

C. Heatmaps showing average number of spatial interactions between two cell states for each treatment cohort and histopathologic site. Cell states are denoted by colors shown in **Figure 1F**. Interactions were normalized first by density of cells participating in the interaction and were then log10+1 transformed. Rows denote treatment cohort and columns denote histopathologic site.

D. Overview schematic of analyses performed in this study. TME features were calculated for each tissue region. Two machine learning classifier models were built for each histopathologic site to predict treatment status and DFS. Feature importance analyses were performed to interpret biological meaning.

Figure 3. Machine learning models classify αCD40-treated TMEs as having reduced T cell exhaustion phenotypes.

A. Bar chart showing accuracy and F1 score for each histopathologic model that predicts treatment status.

B. ROC curve with corresponding AUC for each histopathologic model.

C. Bubble chart showing top 15 features whose increased presence drove each histopathologic model to predict treatment-naive (orange) or αCD40-treated (blue). Features are grouped by TME feature type (density, barcode, interaction). Bubble size denotes relative importance of the feature for a given histopathologic model. Bubbles appearing multiple times in the same row indicate TME feature is a top feature across histopathologic models.

D. Representative pseudo-colored mIHC images showing $TOX1^+$ and/or $EOMES^+$ $CD3^+$ T cells in treatment-naive tissue (left) and $CD44^+$ and/or $T\text{-}BET^+$ $CD3^+$ T cells in aCD40-treated tissue (right).

E. Matrix showing correlations between top barcodes from the models with each other based on types and proportions of T cell states expressing the barcodes. Stacked bars at the top of correlation matrixes show proportions of T cell states expressing barcodes, with T cells color coded and listed for each group to the right of the heatmap, along with corresponding barcodes in each group. Leftmost columns are color coded according to which treatment group the presence of the barcode was predicted by the model, followed by the histopathologic site the model was derived from.

Figure 4. Machine learning model classifies long disease-free survivors as having more T cell effector functionality following αCD40 therapy.

A. Bar chart showing accuracy and F1 score for each histopathologic model predicting αCD40 DFS.

B. ROC curve with corresponding AUC for the IA histopathologic model.

C. Bubble chart showing the top 15 features whose increased presence drove the IA model to predict short DFS (purple) or long DFS (green). Features are grouped by TME feature type (density, barcode, interaction). Bubble size denotes relative importance of the feature.

D. Representative pseudo-colored mIHC images showing TOX1$^+$ and/or PD-1$^+$ CD3$^+$ T cells in short DFS tissue (left) and CD44$^+$ and/or CD39$^+$ CD3$^+$ T cells in long DFS tissue (right). Scale bars = 100 μm.

E. Matrix showing correlations between the top barcodes from the IA model with each other based on types and proportions of T cell states expressing the barcodes. Stacked bars at the top of the correlation matrix show proportions of T cell states expressing the barcodes, and T cells are color coded and listed for each group to the right of the heatmap, along with the corresponding barcodes in each group. Leftmost column is color coded according to which DFS group the presence of the barcode predicted by the model.

Figure 5. Cellular neighborhood analysis identifies spatial organization of T cells to correlate with DFS following αCD40 therapy.

A. Schematic depicting RCN analysis. Cellular neighborhoods were defined by identifying all cells within a 60 μm radius of a given cell. Neighborhoods were calculated for all cells in αCD40-treated IA regions. Neighborhoods were then grouped using K-means clustering to identify RCNs. Created with BioRender.com.

B. Stacked bar chart showing average cellular composition of each of seven RCNs from the αCD40-treated IA regions. Bars are colored by cell state and represent

average proportions (out of 1.0) of each cell state present in neighborhoods assigned to each RCN.

C. Representative IA tissue region as depicted by scatterplot reconstructions. Each dot represents a cell present in the IA, and each cell is colored by its original cell state phenotype (left scatterplot) or RCN assignment (right scatterplot).

D. Heatmap showing top T cell barcodes from the αCD40 IA DFS model clustered by proportion of RCNs the T cell barcodes were assigned to. Rows are barcoded T cells from IA regions from patients associated with short DFS or long DFS ordered by hierarchical clustering of their RCN assignment. Columns are RCNs used as clustering features. Proportion of RCNs was normalized using a log10+1 transformation prior to clustering. Leftmost columns are color coded by DFS group followed by barcode.

E. Stacked bar chart showing average fraction of RCNs barcoded T cells were assigned to for each of two hierarchically clustered groups (C1 or C2).

F. Bar chart showing percentage of T cells expressing Ki-67 residing in each of seven RCNs for αCD40 IA regions. Horizontal dashed line represents percentage of Ki-67$^+$ T cells across all αCD40 IA regions, regardless of RCN assignment.

G. Bar chart showing percentage of T cells expressing GrzB residing in each of seven RCNs for αCD40 IA regions. Horizontal dashed line represents percentage of GrzB$^+$ T cells across all αCD40 IA regions, regardless of RCN assignment. T_{REG} populations were excluded from this analysis.

H. Representative IA region from a patient with long DFS with cells colored by RCN assignment in the upper left scatterplot. Remaining images show mIHC staining of $GrzB^+$ $CD44^+$ $CD3^+$ T cells localized within RCN5. Scale bars = 100 μm.

Figure 6. Spatial features of T cells associated with αCD40 therapy and prolonged DFS in the PDAC TME.

A. T cell subsets that best define resected tumor samples from treatment-naïve (left) or αCD40-treated (right) patients. In the absence of therapy, T cells appear in an exhausted state, while T cells present with activated and effector phenotypes after CD40 agonism. Created with BioRender.com.

B. T cell phenotypes in IAs from αCD40-treated patients associated with long (top) or short (bottom) DFS. IAs from patients with long DFS are characterized by the presence of spatial neighborhoods of effector T cells capable of proliferating and cytotoxicity, while IAs from patients with short DFS have a preponderance of exhausted T cell states. Created with BioRender.com.

SUPPLEMENTARY FIGURE LEGENDS

Supplementary Figure S1.

A. Representative IHC staining of each antibody used in sequence in the panel. Scale bar = 50 μm.

B. Two representative regions stained with CD3, CD8, and CD4 antibodies. For each region, top images show gates for CD8 on $CD3^+$ population (left) and CD4 on $CD3^+$ $CD8^-$ population (right), and bottom row shows pseudo-colored mIHC images.

C. Hierarchical gating template used to phenotype cells using image gating cytometry in FCS Image Cytometry RUO.

Supplementary Figure S2.

A. SHAP plots showing the top 30 features driving each histopathologic model. Features are ordered on the y-axis such that those with a larger impact on model's predictions appear at the top of the SHAP plots. SHAP values are shown on the x-axis, with a value of zero (center) indicating no impact on the model, and negative or positive SHAP values predicting treatment-naive or αCD40-treated tissues, respectively. Red or blue dots indicate presence or absence, respectively, of the corresponding feature in the tissue.

B-E. Box plots showing feature values for each of the top 15 features for models derived from T, IA, TAS, or NAP sites, respectively, split by treatment cohort. Each dot represents the log10+1 normalized feature value for one tissue region, inputted into the classifier model. Boxes = quartile 1 (Q1) to quartile 3 (Q3); whiskers = smallest and largest datapoints within 1.5*interquartile range (IQR) +/- Q3/Q1;

solid line = median. Mann–Whitney *U*-test used to determine statistical significance. *P*-values corrected using the Benjamini–Hochberg procedure. *, $P \leq 0.05$; **, $P \leq 0.01$; ***, $P \leq 0.001$.

B. T site, n= 55 treatment-naive and n = 48 αCD40-treated regions per feature.

C. IA site, n= 89 treatment-naive and n = 43 αCD40-treated regions per feature.

D. TAS site, n = 25 treatment-naive and n = 27 αCD40-treated regions per feature.

E. NAP site, n = 6 treatment-naive and n = 13 αCD40-treated regions per feature.

Supplementary Figure S3.

A. SHAP plot showing the top 30 features driving the IA model. Features are ordered on the y-axis such that those with a larger impact on the model's predictions appear at the top of the SHAP plot. SHAP values are shown on the x-axis, with a value of zero (center) indicating no impact on the model, and negative or positive SHAP values predicting long DFS or short DFS, respectively. Red or blue dots indicate presence or absence, respectively, of the corresponding feature in tissues.

B. Box plot showing feature values for each of the top 15 features for the model derived from IA regions of the αCD40 cohort split by DFS group (n = 30 regions from short DFS patients per feature; n = 13 regions from long DFS patients per feature). Each dot represents the log10+1 normalized feature value for one tissue region, which was inputted into the classifier model. Boxes = Q1 to Q3; whiskers = smallest and largest datapoints within 1.5*IQR +/- Q3/Q1; solid line = median. Mann–Whitney *U*-test used to determine statistical significance. *P*-values

corrected using the Benjamini–Hochberg procedure. *, $P \leq 0.05$; **, $P \leq 0.01$; ***, $P \leq 0.001$.

Supplementary Figure S4.

A. Elbow plot showing optimal number of RCNs (k=7) for grouping cellular neighborhoods.

B. Bar chart showing the number of cells assigned to each of the seven RCNs across all αCD40 IA regions.

C. Bar chart showing the percentage (out of 100) of cells assigned to each of the seven RCNs across all αCD40 IA regions.

D. Stacked bar chart showing fraction (out of 1.0) of RCNs present per αCD40 IA region.

E. Stacked bar chart showing average proportion (out of 1.0) of RCNs present in IA regions for each αCD40-treated patient.

F. Scatterplot reconstructions for each αCD40 IA region. Each dot represents a cell present in the IA, and each cell is colored by its original cell state phenotype (top scatterplot) or RCN assignment (bottom scatterplot).

SUPPLEMENTARY TABLE LEGENDS

Supplementary Table S1.

Statistical comparison between the Liudahl et al. original PDAC cohort(35) and the selected subset used as Cohort 1 in this study. Mean value and standard error of the

mean (SEM) shown for each variable. *P*-values computed using Fisher's exact test for categorical variables, Wilcoxon rank-sum test for continuous variables, and log rank test for overall survival.

Supplementary Table S2.

Table of antibodies used in mIHC panel.

Supplementary Table S3.

Raw counts of cell states defined by mIHC gating strategy present in the dataset.

Supplementary Table S4.

Raw counts of T cells expressing each functionality barcode present in the dataset.

Supplementary Table S5.

Raw counts of cell-cell spatial interactions present in the dataset.

A

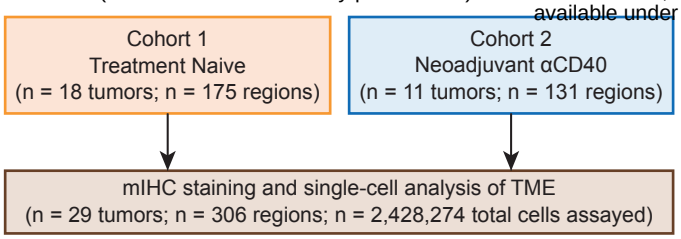

B

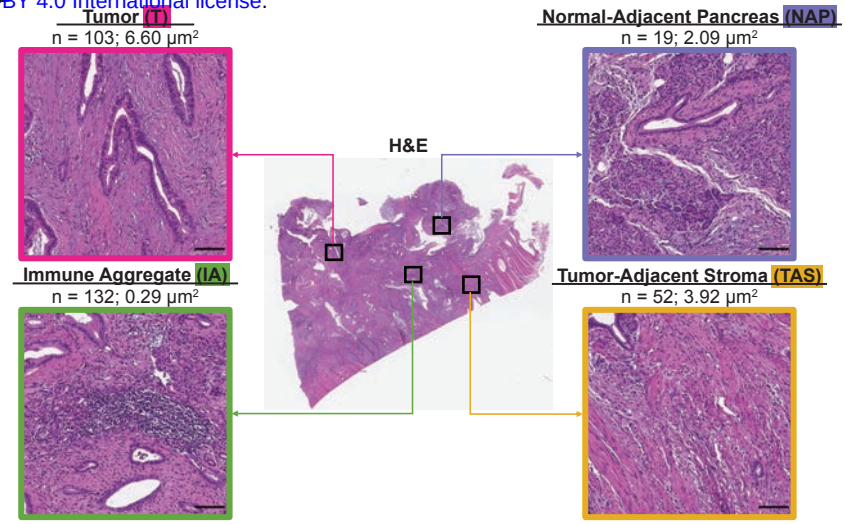

C

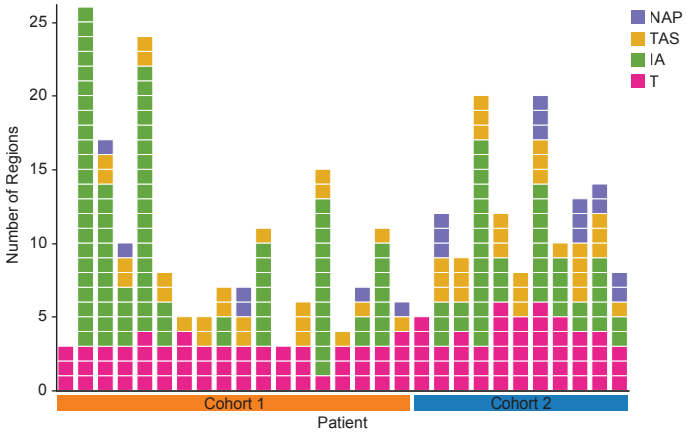

D

mIHC Antibody Panel		
Lineage	T Cell Functionality	Proliferation/ Cytotoxicity
CD3	TOX1	Ki-67
CD20	TIM3	GrzB
CD8	TCF-1	
FOXP3	CD38	
CD45RA	PD-1	
CD45RO	EOMES	
CD11b	CD39	
αSMA	CD44	
PanCK	LAG-3	
	T-BET	

E

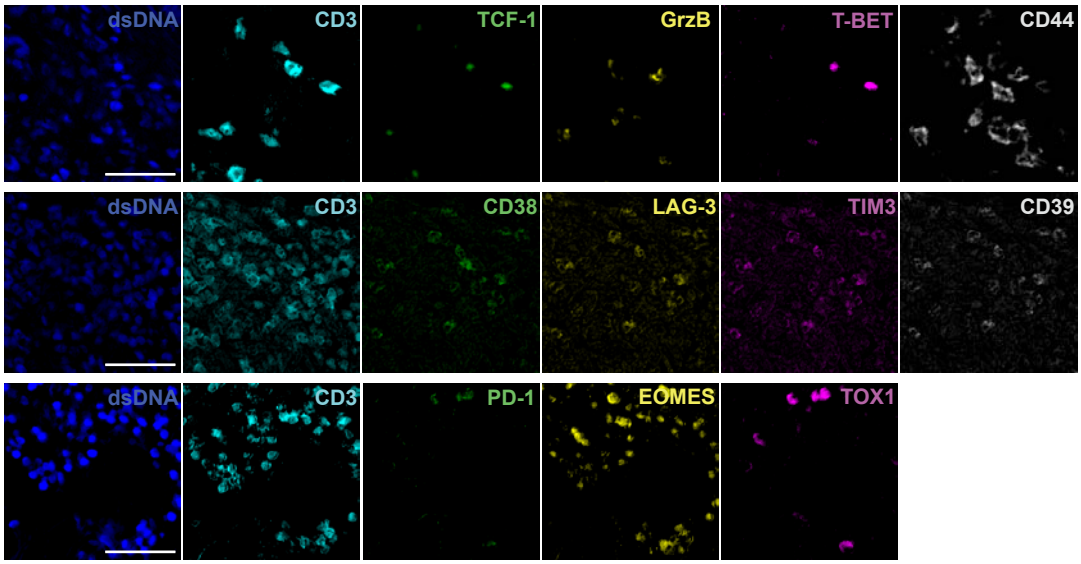

F

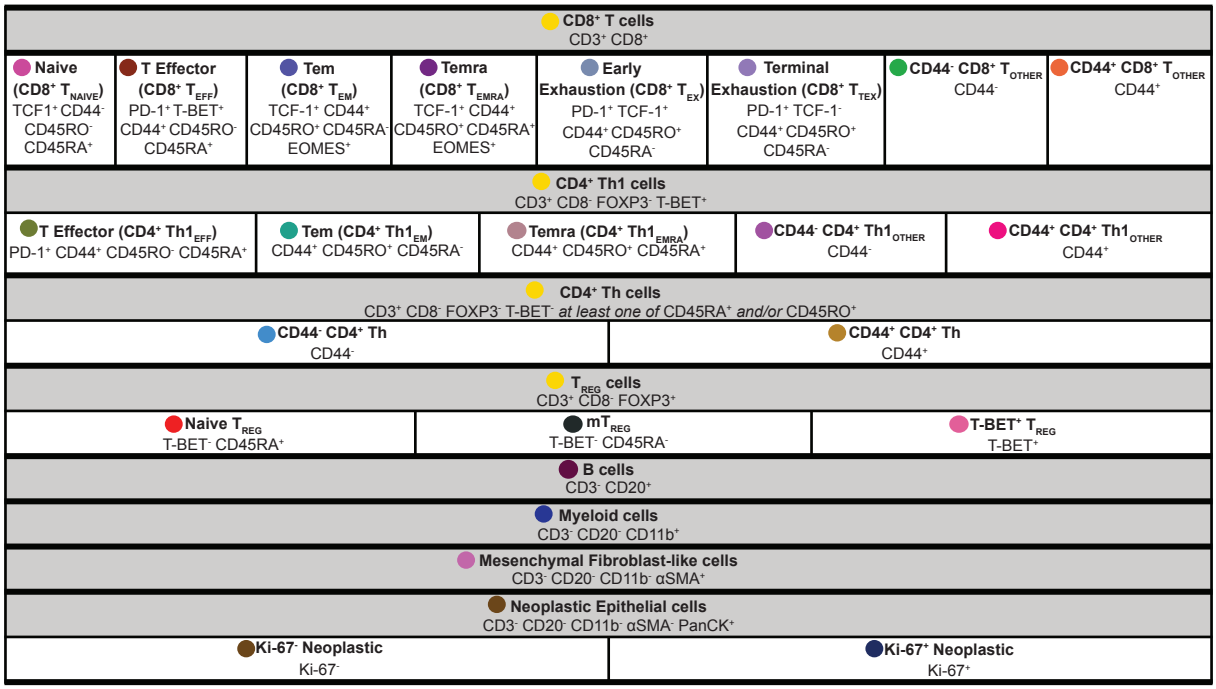

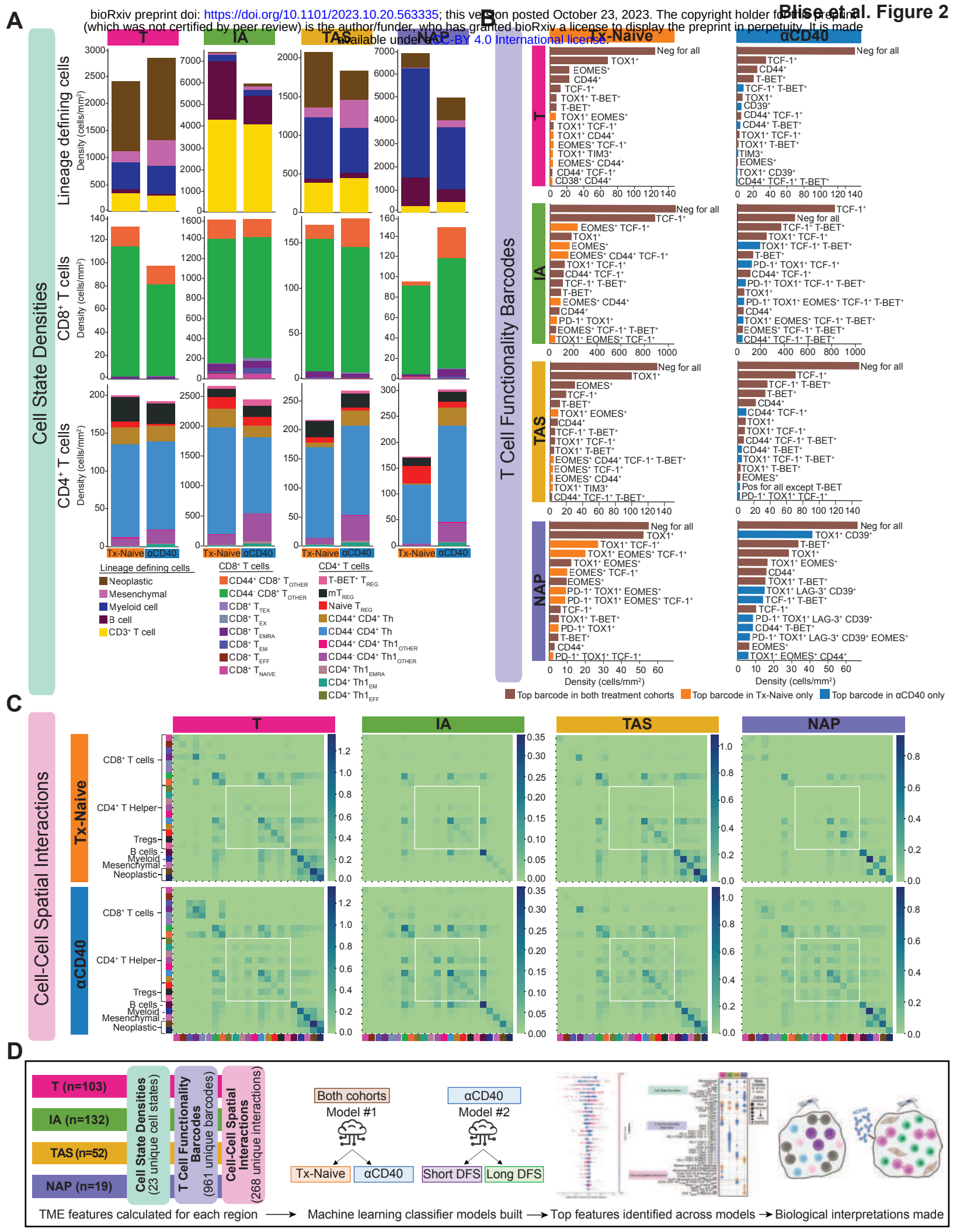

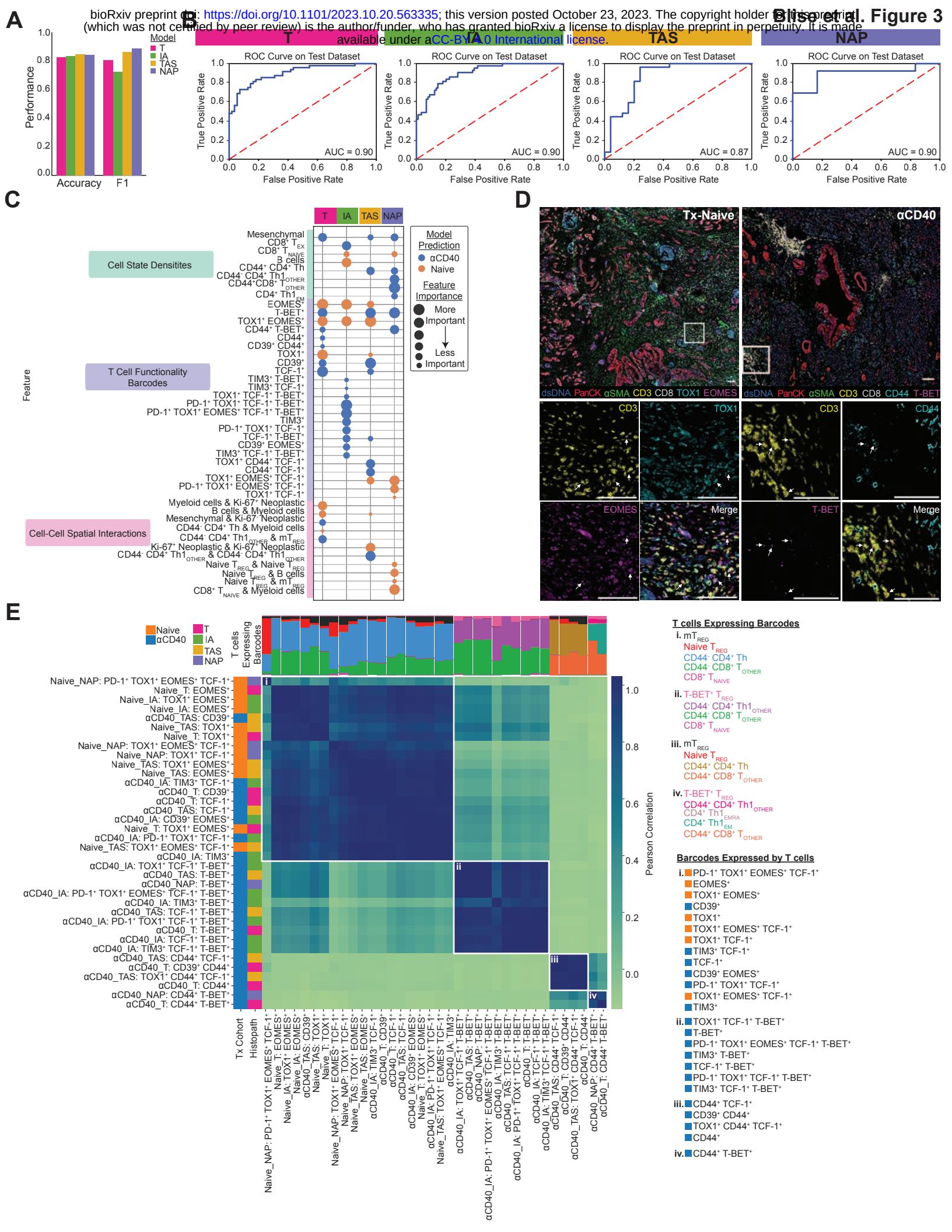

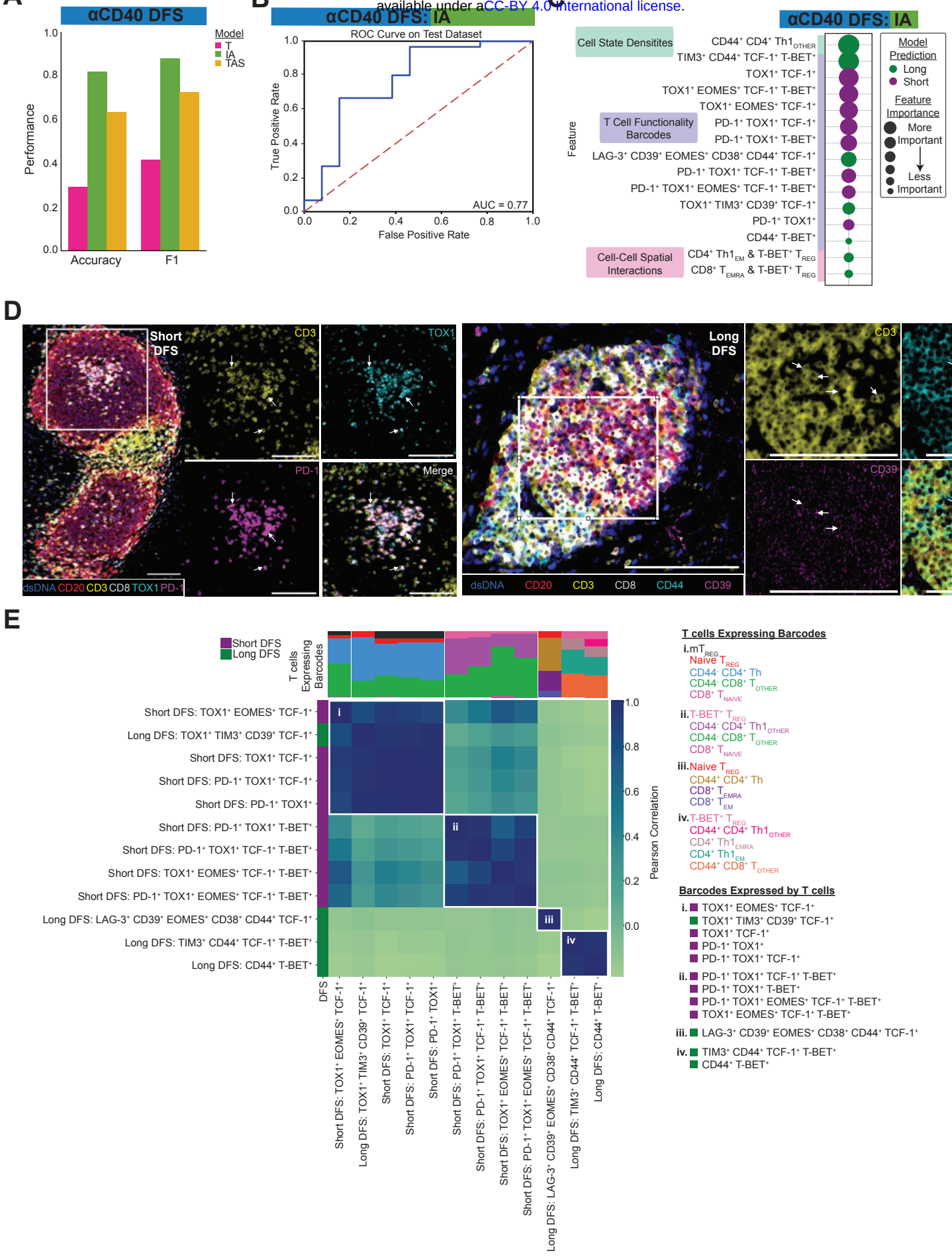

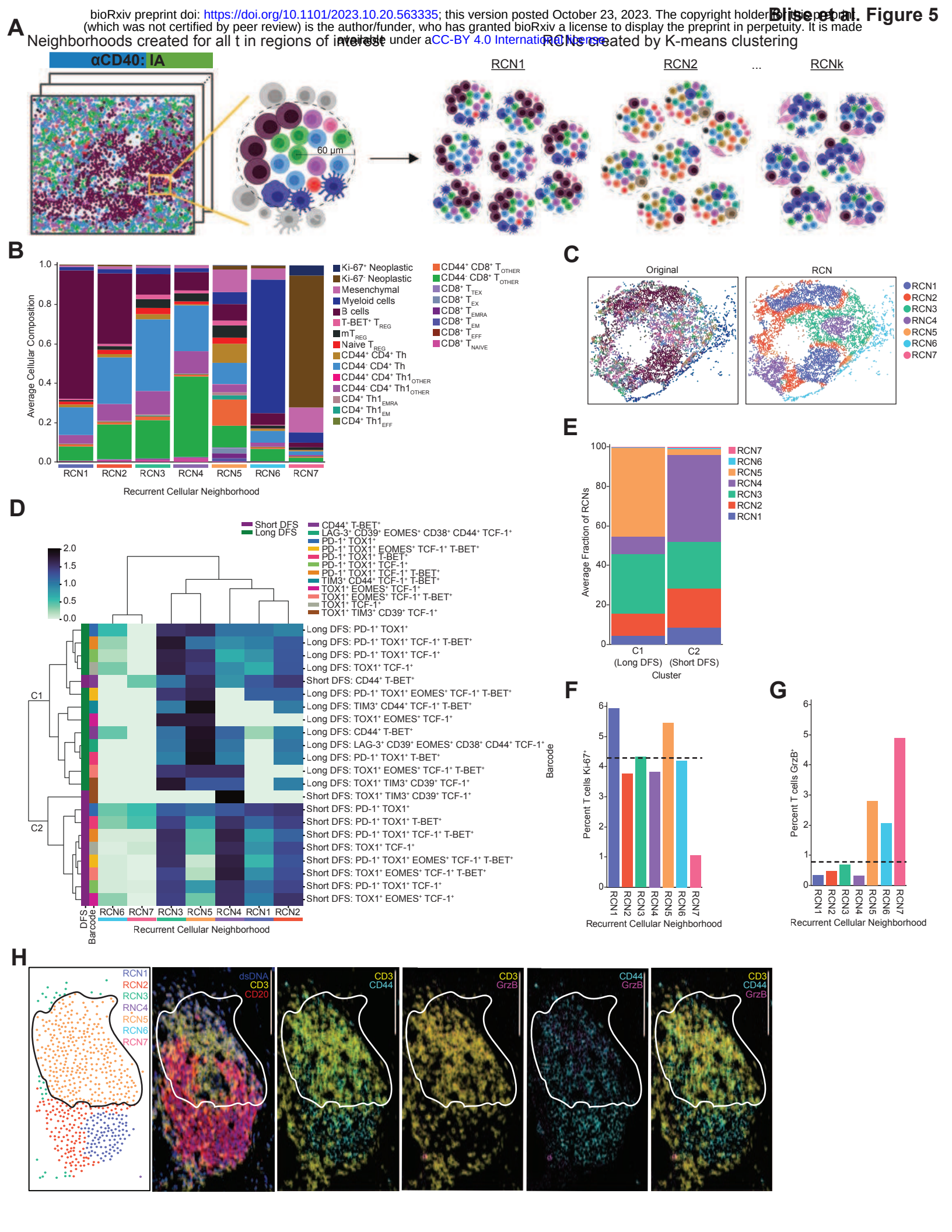

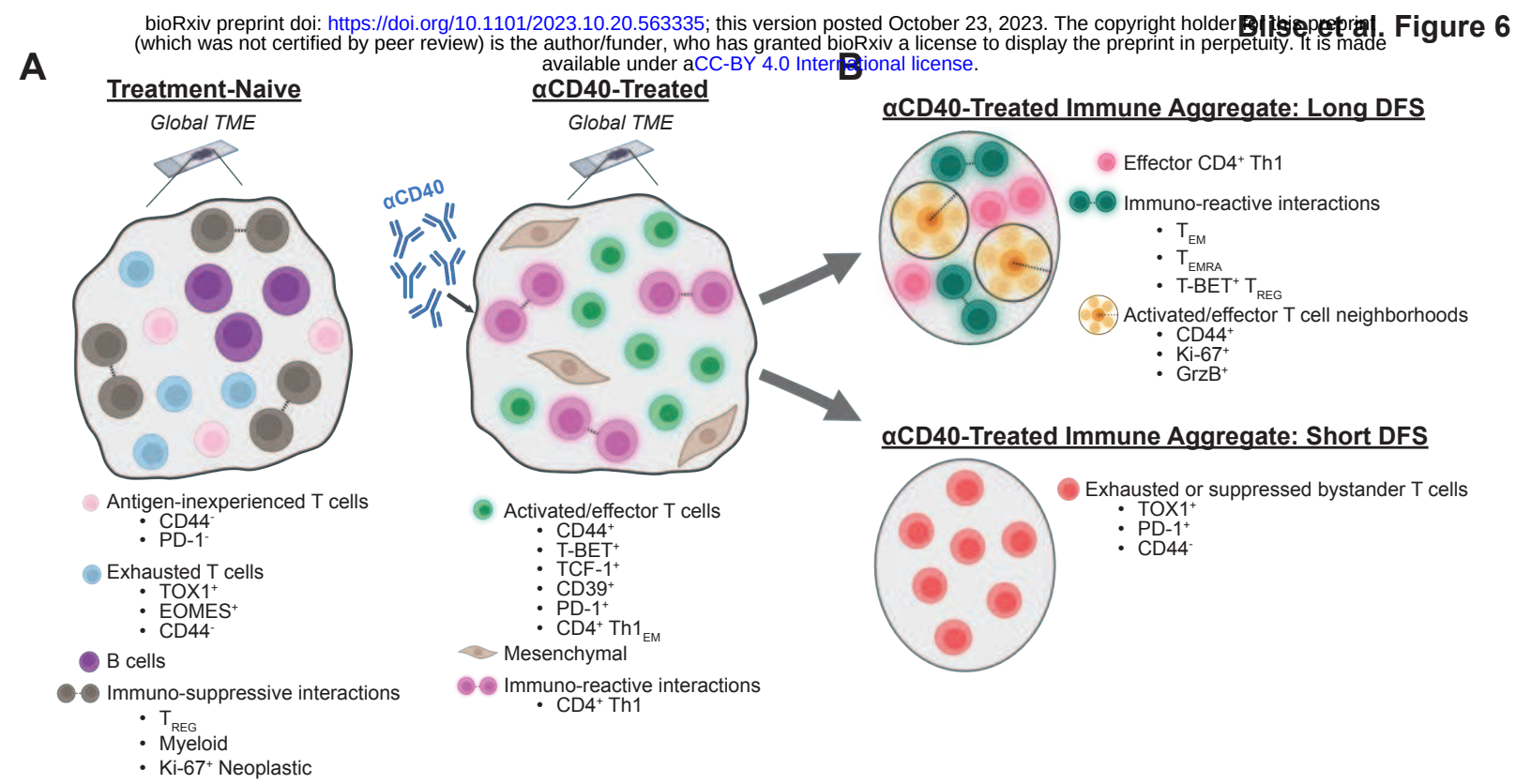

A

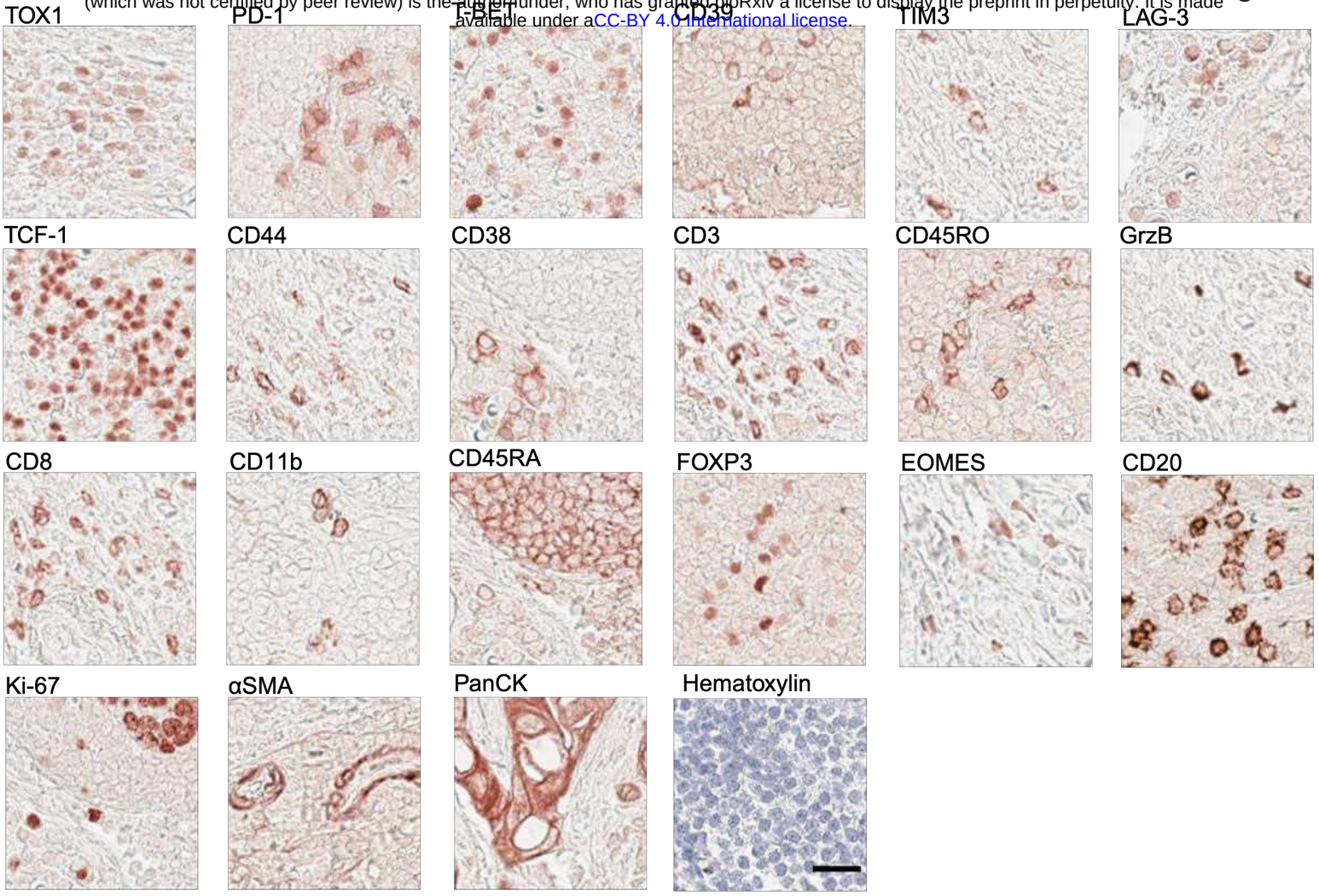

B

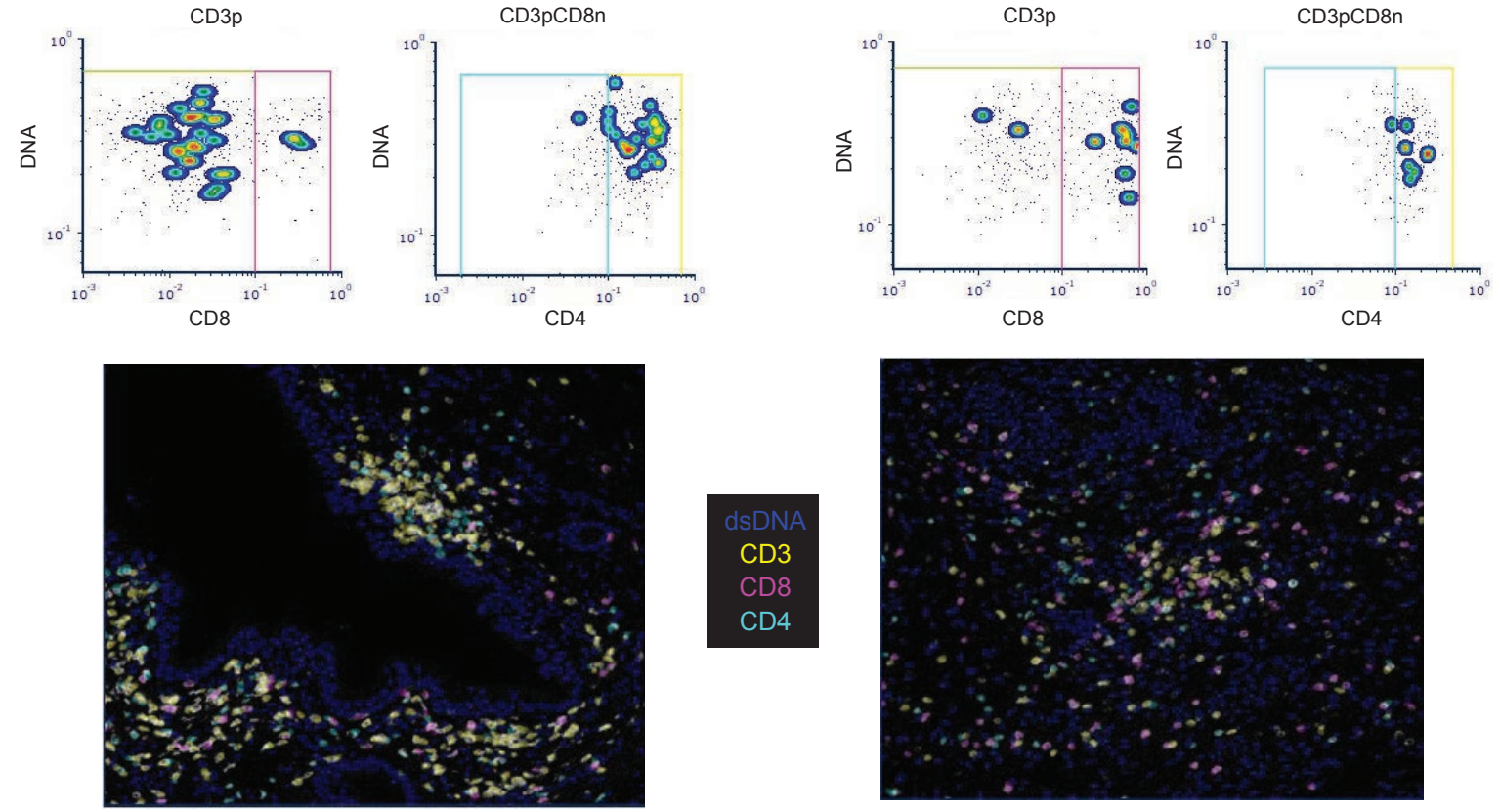

C

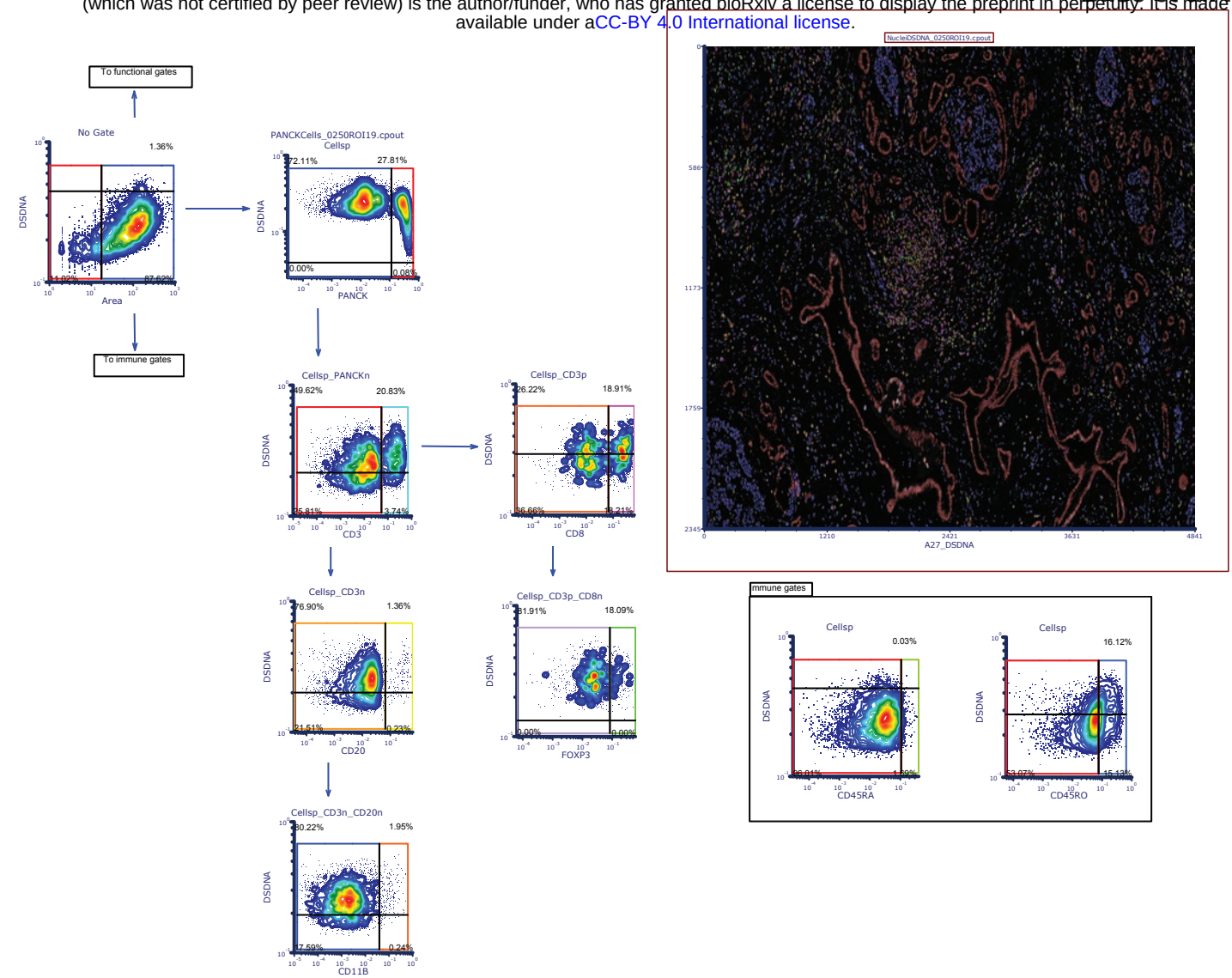

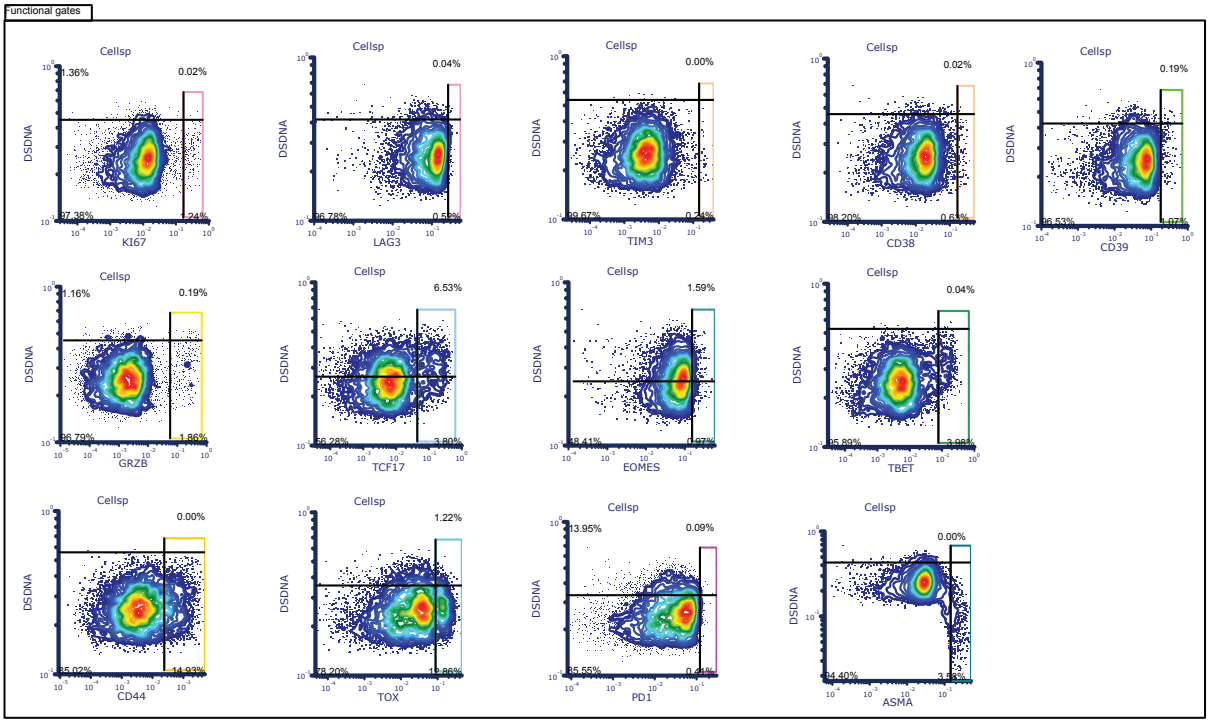

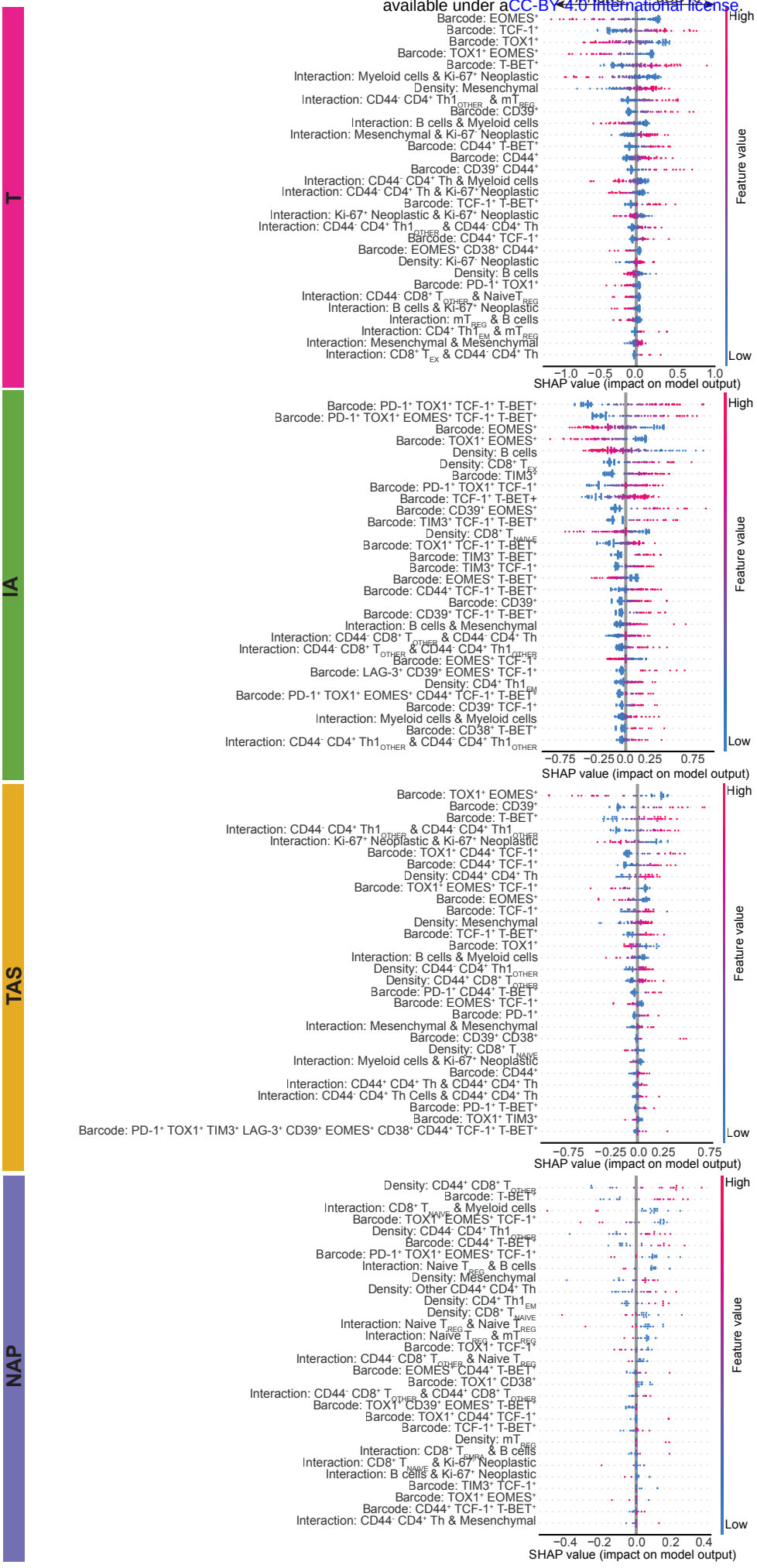

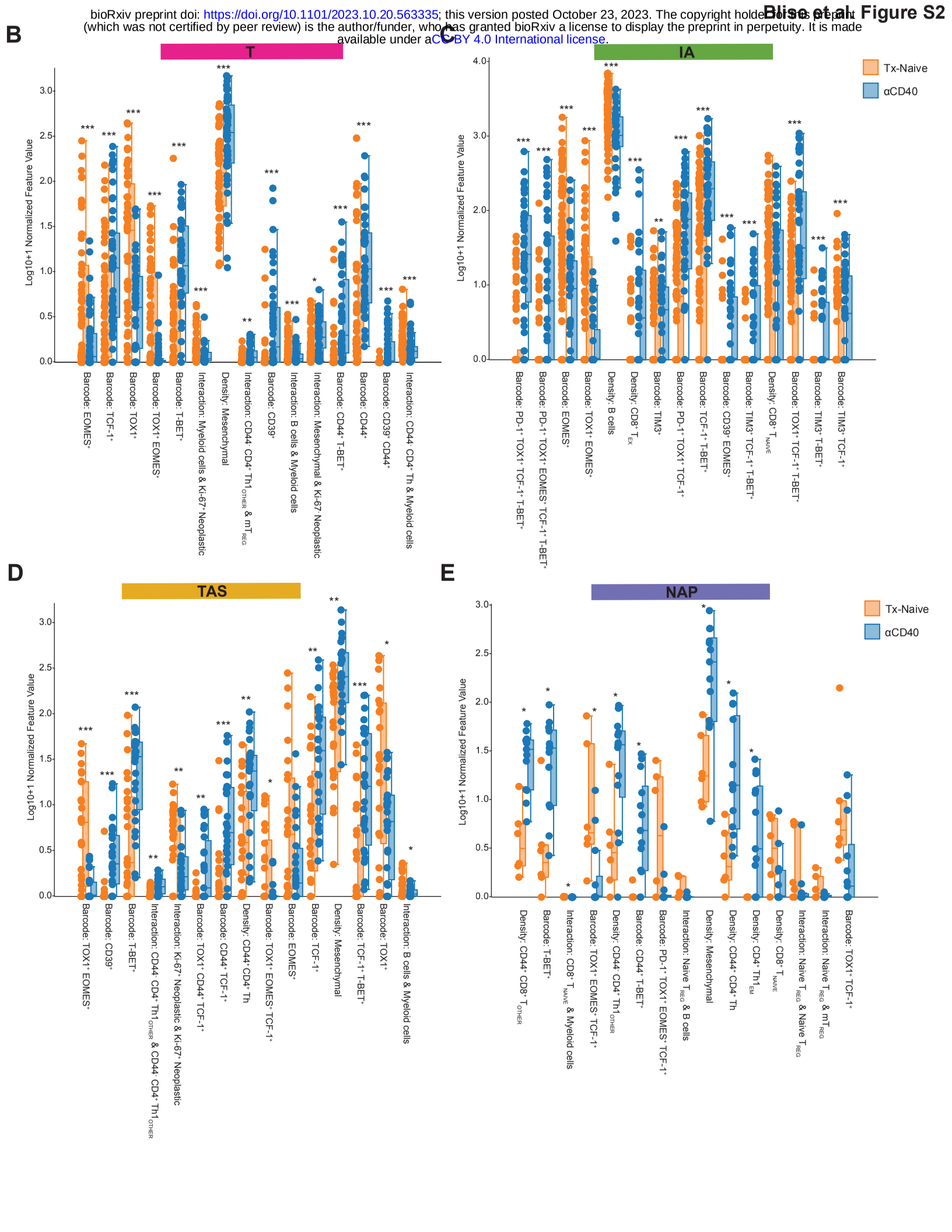

A

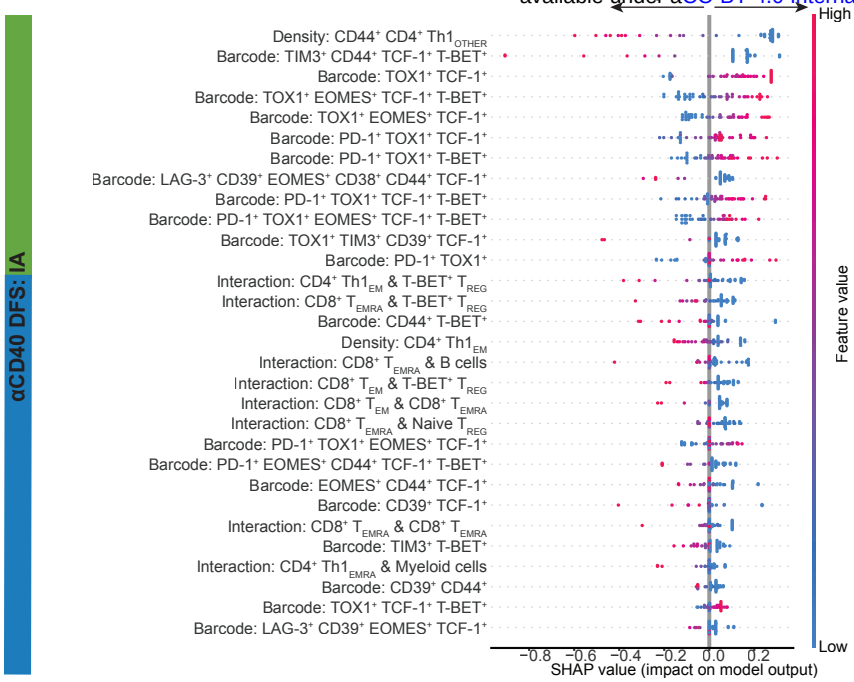

B

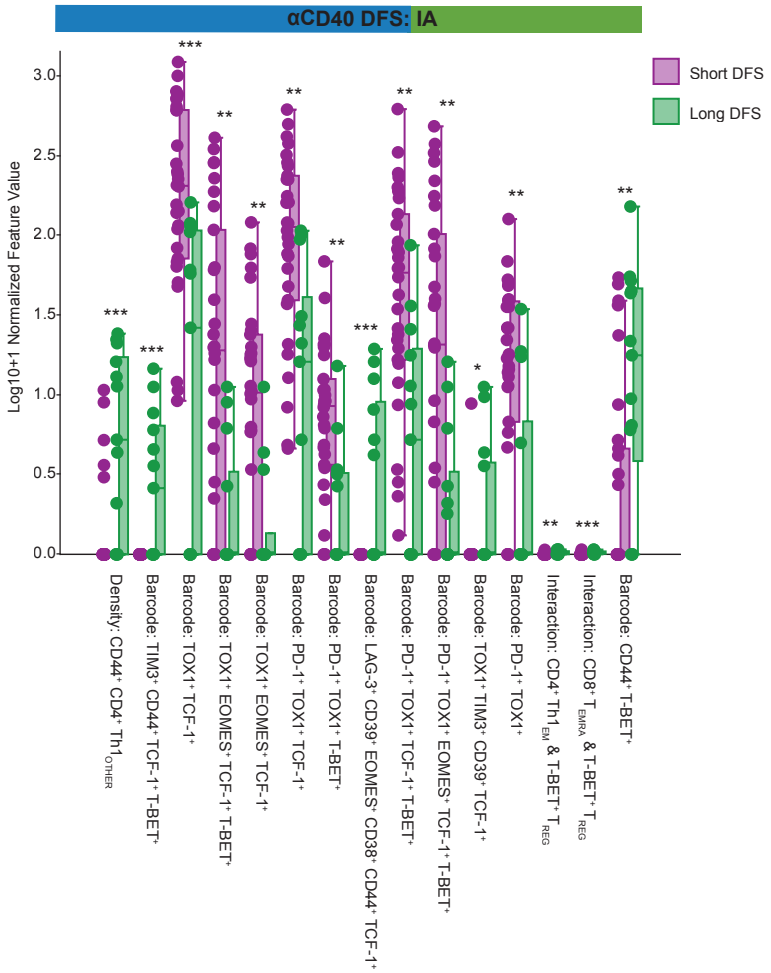

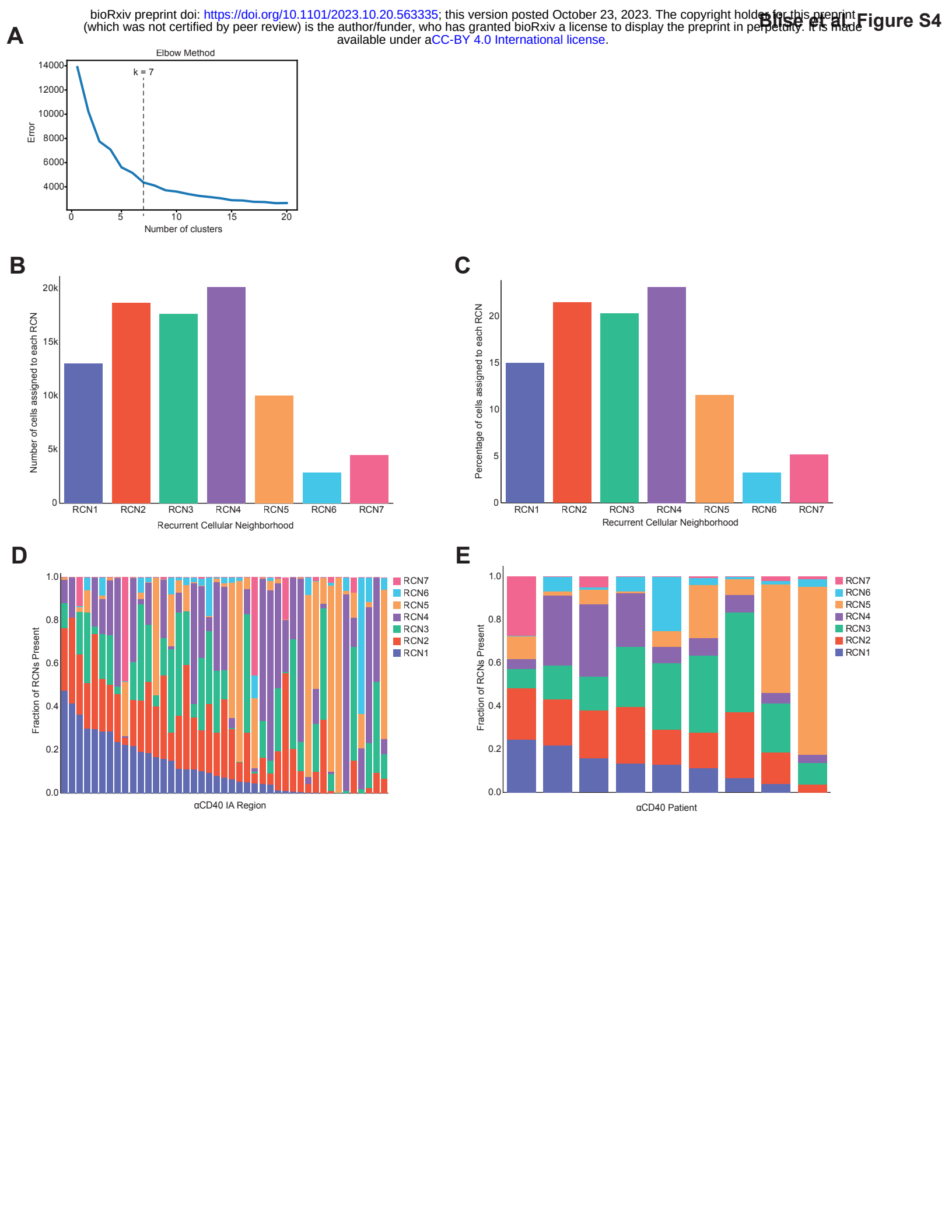

F

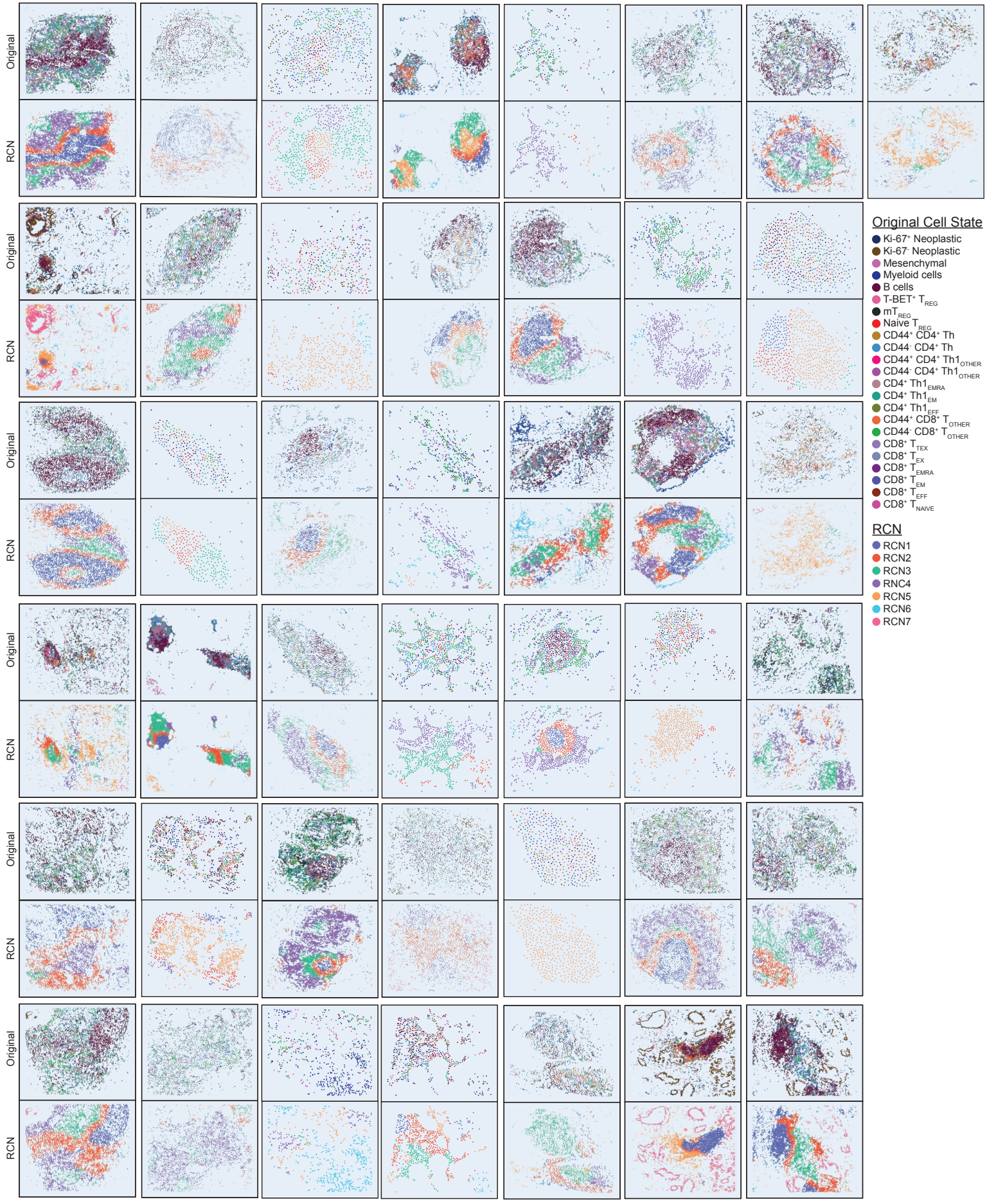

Supplementary Table 1. Statistical comparison between the Liudahl et al. original PDAC cohort and the selected subset used as Cohort 1 in this study. Mean value and standard error of the mean (SEM) shown for each variable. *P*-values computed using Fisher's exact test for categorical variables, Wilcoxon rank-sum test for continuous variables, and log rank test for overall survival.

	Original Cohort	**Selected Subset**	***P***
OS (months) (mean ± SEM)	27.34 ± 2.25	27.27 ± 4.75	0.90
# cases OHSU/DFCI	45/59	6/12	0.61
$CD8^+$ T cell density (mean ± SEM)	144.57 ± 11.49	152.51 ± 26.35	0.63
$CD4^+$ T cell density (mean ± SEM)	185.95 ± 12.45	215.15 ± 30.41	0.33
$CD20^+$ B cell density (mean ± SEM)	98.01 ± 10.68	97.73 ± 21.11	0.85
Plasmablast density (mean ± SEM)	12.13 ± 2.13	10.78 ± 2.86	0.89
Plasma cell density (mean ± SEM)	3.31 ± 0.69	2.51 ± 1.57	0.67
Mast cell density (mean ± SEM)	30.00 ± 2.51	21.25 ± 3.32	0.34
Neutrophil/Eosinophil density (mean ± SEM)	155.74 ± 29.28	220.87 ± 94.11	0.39
Mature Dendritic cell density (mean ± SEM)	3.32 ± 0.32	3.46 ± 0.67	0.59
Immature Dendritic cell density (mean ± SEM)	118.52 ± 11.86	108.79 ± 19.72	0.89
$CD163^-$ Monocyte -Macrophage density (mean ± SEM)	51.68 ± 4.17	37.79 ± 5.50	0.30
$CD163^+$ Monocyte -Macrophage density (mean ± SEM)	73.94 ± 7.16	62.31 ± 14.26	0.59
$CD8^+/CD68^+$ Ratio (mean ± SEM)	1.86 ± 0.24	2.41 ± 0.89	0.21
Total $CD68^+$ cell density (mean ± SEM)	125.61 ± 9.84	100.09 ± 17.97	0.35

Supplementary Table 2. Table of antibodies used in the mIHC panel.

Primary Antibody	Clone	Species	Supplier	Catalog number
TOX1 (Tox)	NAN488B	Rat	Abcam	ab237009
PD-1 (PD1)	NAT105	Mouse	Abcam	ab52597
T-BET (TBET)	D6N8B	Rabbit	Cell Signaling Technologies	13232S
CD39	A1	Mouse	Biolegend	328202
TIM3	D5D5R	Rabbit	Cell Signaling Technologies	45208S
LAG-3 (Lag3)	17B4	Mouse	Novus Biologicals	NBP1-97657
TCF-1 (TCF1/7)	C6D39	Rabbit	Cell Signaling Technologies	2203
CD44	156-3C11	Mouse	Cell Signaling Technologies	3570
CD38	38C03	Mouse	Thermofisher Scientific	MA5-14413
CD3	SP7	Rabbit	Thermofisher Scientific	RM-9107-S
CD45RO	UCHL-1	Mouse	Thermofisher Scientific	MA5-11532
GrzB (Granzyme B)	Polyclonal	Rabbit	Abcam	ab4059
CD8	C8/144B	Mouse	Thermofisher Scientific	MA5-13473
CD11b (CD11B)	EPR1344	Rabbit	Abcam	ab133357
CD45RA	F8-11-13	Mouse	Abcam	ab59168
FOXP3 (Foxp3)	236A/E7	Mouse	eBioscience	14-4777-82
EOMES	Polyclonal	Rabbit	EMD Millipore	AB2283
CD20	L26	Mouse	Abcam	ab9475
Ki-67 (KI67)	SP6	Rabbit	Sigma/Cell Marque	275R-14
αSMA (Alpha-SMA)	Polyclonal	Rabbit	Abcam	ab5694
PanCK (Pan-Cytokeratin)	AE1/AE3	Mouse	Abcam	ab27988

Supplementary Table S3. Raw counts of cell states defined by mIHC gating strategy present in the dataset.

Cell State	Count
Ki-67- Neoplastic	915586
Myeloid cells	593571
Mesenchymal	247778
CD44- CD4 Th	163809
CD44- CD8 TOTHER	136543
B cells	132728
Ki-67+ Neoplastic	115294
mTREG	30836
CD44+ CD4 Th	24232
CD44+ CD8 TOTHER	21711
CD44- CD4 Th1OTHER	21157
Naive TREG	10075
TBET+ TREG	3674
CD8 TEMRA	3550
CD8 TNAIVE	2328
CD4 Th1EM	2038
CD4 Th1EMRA	1165
CD8 TEM	940
CD8 TEX	525
CD44+ CD4 Th1OTHER	449
CD8 TTEX	200
CD8 TEFF	64
CD4 Th1EFF	21

Supplementary Table S4. Raw counts of T cells expressing each functionality barcode present in the dataset.

T cell Functionality Barcode	Count
Negative for all	144053
TOX1+	51606
TCF-1+	50915
CD44+	19724
T-BET+	15539
EOMES+	15405
TCF-1+ T-BET+	12775
TOX1+ TCF-1+	10565
CD44+ TCF-1+	7742
EOMES+ TCF-1+	6118
TOX1+ T-BET+	5000
TOX1+ EOMES+	4876
TOX1+ TCF-1+ T-BET+	4403
EOMES+ CD44+	3505
EOMES+ CD44+ TCF-1+	3318
TOX1+ CD44+	3002
PD-1+ TOX1+ TCF-1+	2684
PD-1+ TOX1+	2669
CD44+ T-BET+	2174
CD44+ TCF-1+ T-BET+	2103
EOMES+ TCF-1+ T-BET+	1862
CD39+	1804
TOX1+ EOMES+ TCF-1+	1629
TOX1+ CD44+ TCF-1+	1591
TOX1+ TIM3+	1574
TOX1+ CD39+	1472
CD38+ CD44+	1356
PD-1+ TOX1+ TCF-1+ T-BET+	1262
PD-1+	1177
TOX1+ EOMES+ TCF-1+ T-BET+	1153
EOMES+ T-BET+	1152
TIM3+	1084
TOX1+ CD38+	949
CD38+	936
PD-1+ TOX1+ EOMES+ TCF-1+ T-BET+	923
TOX1+ EOMES+ CD44+	851
PD-1+ TOX1+ EOMES+	840
PD-1+ TCF-1+	833
LAG-3+	819
PD-1+ TOX1+ EOMES+ TCF-1+	785
EOMES+ CD44+ TCF-1+ T-BET+	751
PD-1+ TOX1+ TIM3+ LAG-3+ CD39+ EOMES+ CD38+ CD44+ TCF-1+ T-BET+	728
TOX1+ EOMES+ T-BET+	582

PD-1+ TOX1+ CD44+ TCF-1+	553
TOX1+ CD38+ CD44+	512
TOX1+ CD39+ EOMES+	495
TOX1+ CD44+ TCF-1+ T-BET+	483
CD39+ EOMES+	478
LAG-3+ TCF-1+	473
TOX11+ CD44+ T-BET+	461
PD-1+ TOX11+ T-BET+	457
CD39+ TCF-1+	448
TOX11+ EOMES+ CD44+ TCF-1+	437
TIM3+ CD44+	430
PD-1+ T-BET+	386
EOMES+ CD38+ CD44+	351
CD38+ CD44+ TCF-1+	341
EOMES+ CD38+ CD44+ TCF-1+	319
PD-1+ TOX1+ CD39+	310
TOX1+ LAG-3+ CD39+	304
TOX1+ LAG-3+	303
EOMES+ CD44+ T-BET+	292
TIM3+ TCF-1+	281
LAG-3+ T-BET+	269
PD-1+ EOMES+ TCF-1+	256
EOMES+ CD38+	252
TIM3+ T-BET+	249
PD-1+ TOX1+ TIM3+ LAG-3+ CD39+ EOMES+ CD38+ CD44+ TCF-1+	247
PD-1+ TOX1+ CD44+	244
CD38+ TCF-1+	228
PD-1+ TCF-1+ T-BET+	216
PD-1+ EOMES+	216
TOX1+ TIM3+ T-BET+	208
LAG-3+ EOMES+ TCF-1+	198
LAG-3+ TCF-1+ T-BET+	193
CD39+ CD44+	190
TOX1+ CD38+ CD44+ TCF-1+	178
PD-1+ TOX1+ LAG-3+ CD39+	175
PD-1+ TOX1+ CD44+ TCF-1+ T-BET+	173
LAG-3+ EOMES+	167
PD-1+ CD44+ TCF-1+	166
TOX1+ TIM3+ CD39+ CD44+ TCF-1+ T-BET+	165
TOX1+ EOMES+ CD44+ TCF-1+ T-BET+	162
CD39+ T-BET+	161
TOX1+ TIM3+ CD44+	157
TOX1+ TIM3+ TCF-1+	150
PD-1+ CD44+	149

TIM3+ TCF-1+ T-BET+	144
TOX1+ EOMES+ CD44+ T-BET+	144
CD39+ EOMES+ TCF-1+	144
CD39+ TCF-1+ T-BET+	141
PD-1+ TOX1+ EOMES+ T-BET+	139
TOX1+ CD39+ EOMES+ TCF-1+	138
TOX1+ TIM3+ CD39+ CD38+ CD44+ TCF-1+ T-BET+	137
PD-1+ TOX1+ LAG-3+ CD39+ EOMES+	135
TOX1+ EOMES+ CD38+ CD44+ TCF-1+	133
TOX1+ CD39+ TCF-1+	133
PD-1+ TOX1+ TIM3+ LAG-3+ CD39+ CD38+ CD44+ TCF-1+ T-BET+	129
TOX1+ CD38+ T-BET+	125
PD-1+ TOX1+ CD39+ EOMES+	124
EOMES+ CD38+ TCF-1+	124
TOX1+ LAG-3+ TCF-1+	122
PD-1+ TOX1+ LAG-3+	118
PD-1+ TOX1+ EOMES+ CD44+ TCF-1+	116
TOX1+ LAG-3+ EOMES+	115
PD-1+ EOMES+ TCF-1+ T-BET+	115
TIM3+ EOMES+	113
PD-1+ TOX1+ LAG-3+ CD39+ EOMES+ CD38+ CD44+ TCF-1+	112
TOX1+ EOMES+ CD38+ CD44+	111
PD-1+ TOX1+ TIM3+	109
LAG-3+ CD44+ TCF-1+	109
LAG-3+ CD39+	107
LAG-3+ CD44+	107
TOX1+ TIM3+ EOMES+	105
TIM3+ CD44+ TCF-1+	103
PD-1+ TOX1+ CD39+ EOMES+ TCF-1+	101
CD38+ T-BET+	100
TOX1+ CD39+ EOMES+ CD38+ TCF-1+	99
TIM3+ CD39+	97
TOX1+ TIM3+ TCF-1+ T-BET+	97
PD-1+ TOX1+ EOMES+ CD44+ TCF-1+ T-BET+	97
LAG-3+ EOMES+ TCF-1+ T-BET+	95
CD39+ EOMES+ TCF-1+ T-BET+	94
CD39+ CD38+	94
TOX1+ LAG-3+ CD39+ EOMES+	94
PD-1+ TOX1+ TIM3+ LAG-3+ EOMES+ CD38+ CD44+ TCF-1+ T-BET+	94
CD38+ CD44+ T-BET+	93
CD39+ EOMES+ CD38+ CD44+	93
TOX1+ CD39+ T-BET+	91
TIM3+ CD44+ T-BET+	91
CD38+ TCF-1+ T-BET+	90

CD39+ EOMES+ CD38+	90
TOX1+ EOMES+ CD38+	88
TOX1+ CD38+ TCF-1+	88
TOX1+ CD39+ EOMES+ CD44+ TCF-1+ T-BET+	88
TOX1+ LAG-3+ EOMES+ TCF-1+	86
CD38+ CD44+ TCF-1+ T-BET+	85
LAG-3+ EOMES+ CD44+ TCF-1+	83
CD39+ CD38+ CD44+	83
TOX1+ TIM3+ CD39+ EOMES+ CD38+ CD44+ TCF-1+ T-BET+	82
TOX1+ TIM3+ LAG-3+ CD39+ EOMES+ CD38+ CD44+ TCF-1+ T-BET+	78
PD-1+ TOX1+ LAG-3+ EOMES+	75
TOX1+ EOMES+ CD38+ TCF-1+	75
PD-1+ TOX1+ CD39+ TCF-1+	73
PD-1+ CD44+ TCF-1+ T-BET+	71
PD-1+ TOX1+ CD38+	70
PD-1+ EOMES+ T-BET+	69
PD-1+ TOX1+ TIM3+ LAG-3+ CD38+ CD44+ TCF-1+ T-BET+	67
PD-1+ TOX1+ EOMES+ CD44+	67
PD-1+ EOMES+ CD44+ TCF-1+ T-BET+	67
TOX1+ CD39+ EOMES+ CD38+ CD44+ TCF-1+	64
TOX1+ CD39+ TCF-1+ T-BET+	63
PD-1+ TOX1+ TIM3+ LAG-3+ CD39+ EOMES+ CD44+ TCF-1+ T-BET+	63
TIM3+ EOMES+ CD44+	62
CD39+ EOMES+ T-BET+	61
TOX1+ TIM3+ EOMES+ TCF-1+	61
TIM3+ EOMES+ T-BET+	60
TOX1+ LAG-3+ T-BET+	60
PD-1+ EOMES+ CD44+ TCF-1+	59
CD39+ EOMES+ CD44+	59
PD-1+ TOX1+ LAG-3+ EOMES+ TCF-1+	59
LAG-3+ CD39+ TCF-1+	57
PD-1+ TOX1+ CD44+ T-BET+	57
PD-1+ TOX1+ LAG-3+ CD39+ EOMES+ CD38+ TCF-1+	56
LAG-3+ CD44+ TCF-1+ T-BET+	56
TIM3+ EOMES+ TCF-1+	54
PD-1+ TOX1+ LAG-3+ T-BET+	53
PD-1+ TOX1+ CD39+ EOMES+ TCF-1+ T-BET+	53
CD39+ EOMES+ CD38+ CD44+ TCF-1+	53
PD-1+ TOX1+ TIM3+ TCF-1+	53
CD39+ CD44+ TCF-1+	52
TOX1+ TIM3+ CD44+ TCF-1+	52
PD-1+ TOX1+ LAG-3+ TCF-1+	51
TOX1+ CD39+ EOMES+ CD38+	50
CD39+ EOMES+ CD38+ TCF-1+	49

PD-1+ CD44+ T-BET+	48
TOX1+ CD39+ EOMES+ CD38+ CD44+	47
TIM3+ EOMES+ CD44+ TCF-1+	47
PD-1+ TOX1+ CD39+ TCF-1+ T-BET+	47
TOX1+ CD39+ CD44+ TCF-1+ T-BET+	47
CD39+ EOMES+ CD44+ TCF-1+	46
PD-1+ TIM3+ LAG-3+ CD39+ EOMES+ CD38+ CD44+ TCF-1+ T-BET+	45
PD-1+ TOX1+ TIM3+ TCF-1+ T-BET+	44
PD-1+ TOX1+ TIM3+ LAG-3+ EOMES+ CD38+ CD44+ TCF-1+	43
TOX1+ CD39+ CD44+	43
CD39+ EOMES+ CD44+ TCF-1+ T-BET+	43
LAG-3+ CD38+ CD44+ TCF-1+	43
TOX1+ TIM3+ CD39+	43
LAG-3+ EOMES+ CD44+	42
PD-1+ TOX1+ LAG-3+ CD39+ EOMES+ CD38+ CD44+	42
TOX1+ CD38+ CD44+ TCF-1+ T-BET+	42
EOMES+ CD38+ CD44+ TCF-1+ T-BET+	42
LAG-3+ EOMES+ T-BET+	41
TIM3+ CD39+ TCF-1+	41
PD-1+ TOX1+ LAG-3+ CD39+ EOMES+ CD38+	41
PD-1+ CD39+	40
LAG-3+ EOMES+ CD38+ CD44+ TCF-1+	40
PD-1+ TOX1+ LAG-3+ CD39+ EOMES+ CD38+ CD44+ TCF-1+ T-BET+	40
LAG-3+ CD39+ EOMES+	39
PD-1+ EOMES+ CD44+	39
PD-1+ TOX1+ TIM3+ LAG-3+ CD39+ EOMES+ CD38+ TCF-1+	38
PD-1+ TOX1+ TIM3+ CD39+ EOMES+ CD38+ CD44+ TCF-1+ T-BET+	37
PD-1+ TOX1+ LAG-3+ EOMES+ T-BET+	37
TOX1+ LAG-3+ TCF-1+ T-BET+	37
PD-1+ TOX1+ TIM3+ T-BET+	37
TOX1+ TIM3+ CD38+ CD44+	37
PD-1+ TOX1+ CD38+ CD44+	37
PD-1+ TOX1+ LAG-3+ CD39+ EOMES+ TCF-1+	36
TOX1+ TIM3+ LAG-3+ EOMES+ CD38+ CD44+ TCF-1+ T-BET+	36
TOX1+ CD39+ EOMES+ T-BET+	35
TOX1+ TIM3+ EOMES+ CD44+	35
PD-1+ TOX1+ TIM3+ CD38+ CD44+ TCF-1+ T-BET+	34
TIM3+ CD39+ CD44+	34
LAG-3+ EOMES+ CD44+ TCF-1+ T-BET+	34
TOX1+ TIM3+ CD38+	34
TOX1+ CD38+ TCF-1+ T-BET+	33
PD-1+ LAG-3+ EOMES+ TCF-1+	33
PD-1+ TOX1+ TIM3+ CD39+ EOMES+ CD38+ CD44+ TCF-1+	32
PD-1+ TOX1+ TIM3+ CD38+ CD44+ T-BET+	32

LAG-3+ CD44+ T-BET+	32
TOX1+ CD39+ EOMES+ CD44+ TCF-1+	32
TIM3+ CD44+ TCF-1+ T-BET+	32
TIM3+ CD39+ CD38+	32
CD39+ CD44+ TCF-1+ T-BET+	32
TIM3+ CD38+ CD44+	31
LAG-3+ EOMES+ CD38+ CD44+	31
PD-1+ TOX1+ TIM3+ LAG-3+ CD39+ CD44+ TCF-1+ T-BET+	31
PD-1+ LAG-3+ EOMES+	31
PD-1+ TOX1+ EOMES+ CD44+ T-BET+	31
TOX1+ TIM3+ LAG-3+ CD39+ CD38+ CD44+ TCF-1+ T-BET+	31
LAG-3+ CD38+ TCF-1+	31
PD-1+ TOX1+ TIM3+ LAG-3+ EOMES+ CD38+ TCF-1+ T-BET+	30
TOX1+ CD39+ CD38+	30
TOX1+ TIM3+ CD44+ T-BET+	30
TIM3+ EOMES+ TCF-1+ T-BET+	30
TOX1+ LAG-3+ CD39+ EOMES+ CD44+ TCF-1+ T-BET+	30
PD-1+ LAG-3+	30
PD-1+ TOX1+ LAG-3+ CD39+ EOMES+ TCF-1+ T-BET+	30
TOX1+ CD39+ CD44+ TCF-1+	29
PD-1+ TOX1+ CD39+ T-BET+	29
TOX1+ TIM3+ CD44+ TCF-1+ T-BET+	29
PD-1+ TOX1+ TIM3+ LAG-3+ CD39+ EOMES+ CD38+ CD44+ T-BET+	29
LAG-3+ CD39+ EOMES+ CD38+ CD44+ TCF-1+	29
LAG-3+ CD39+ EOMES+ CD38+ CD44+	29
TIM3+ LAG-3+	29
LAG-3+ CD38+	28
TOX1+ EOMES+ CD38+ CD44+ TCF-1+ T-BET+	28
LAG-3+ CD39+ EOMES+ TCF-1+ T-BET+	28
TIM3+ LAG-3+ T-BET+	28
TOX1+ LAG-3+ EOMES+ TCF-1+ T-BET+	28
TOX1+ CD39+ EOMES+ TCF-1+ T-BET+	28
TOX1+ TIM3+ EOMES+ CD44+ TCF-1+	28
LAG-3+ CD39+ EOMES+ CD38+	28
PD-1+ TOX1+ LAG-3+ EOMES+ CD38+ TCF-1+	27
TIM3+ EOMES+ CD44+ TCF-1+ T-BET+	27
PD-1+ TOX1+ LAG-3+ CD39+ TCF-1+	27
PD-1+ LAG-3+ TCF-1+	27
PD-1+ LAG-3+ CD38+ TCF-1+ T-BET+	27
TOX1+ LAG-3+ CD39+ TCF-1+	27
PD-1+ TOX1+ LAG-3+ CD39+ T-BET+	27
TOX1+ CD38+ CD44+ T-BET+	26
TOX1+ TIM3+ LAG-3+ CD39+ EOMES+ CD38+ CD44+ TCF-1+	26
PD-1+ TOX1+ LAG-3+ EOMES+ CD38+	26

LAG-3+ EOMES+ CD38+ TCF-1+	26
TOX1+ LAG-3+ CD39+ EOMES+ CD38+ TCF-1+	26
LAG-3+ CD39+ EOMES+ CD38+ TCF-1+	26
TOX1+ TIM3+ LAG-3+ CD38+ CD44+ TCF-1+ T-BET+	26
PD-1+ TOX1+ TIM3+ CD39+ EOMES+ CD44+ TCF-1+	26
LAG-3+ CD39+ EOMES+ TCF-1+	26
PD-1+ TIM3+	25
CD39+ CD38+ CD44+ TCF-1+	25
PD-1+ TOX1+ LAG-3+ TCF-1+ T-BET+	25
PD-1+ TIM3+ LAG-3+ EOMES+ CD38+ CD44+ TCF-1+ T-BET+	25
LAG-3+ CD38+ CD44+	25
TOX1+ TIM3+ LAG-3+	25
LAG-3+ CD39+ TCF-1+ T-BET+	25
TOX1+ LAG-3+ EOMES+ T-BET+	25
TOX1+ TIM3+ CD38+ CD44+ TCF-1+ T-BET+	25
TOX1+ TIM3+ LAG-3+ EOMES+ CD38+ TCF-1+ T-BET+	24
PD-1+ TOX1+ CD39+ EOMES+ CD38+	24
CD39+ CD38+ TCF-1+	24
TIM3+ EOMES+ CD38+ CD44+ TCF-1+	24
TOX1+ TIM3+ EOMES+ CD38+ CD44+ TCF-1+	23
PD-1+ TOX1+ TIM3+ CD44+ TCF-1+	23
TOX1+ LAG-3+ CD39+ EOMES+ CD38+	23
PD-1+ TOX1+ CD39+ CD44+	23
PD-1+ TOX1+ CD39+ EOMES+ CD38+ TCF-1+	23
PD-1+ TOX1+ TIM3+ EOMES+ CD38+ CD44+ TCF-1+ T-BET+	23
CD39+ CD44+ T-BET+	23
PD-1+ TOX1+ CD39+ EOMES+ CD44+ TCF-1+	23
TIM3+ LAG-3+ CD39+ EOMES+ CD38+ CD44+ TCF-1+ T-BET+	22
LAG-3+ CD38+ CD44+ TCF-1+ T-BET+	22
TOX1+ TIM3+ EOMES+ T-BET+	22
TOX1+ CD39+ EOMES+ CD44+	22
PD-1+ TOX1+ LAG-3+ CD39+ EOMES+ CD38+ TCF-1+ T-BET+	22
EOMES+ CD38+ TCF-1+ T-BET+	22
LAG-3+ CD38+ TCF-1+ T-BET+	22
TIM3+ CD39+ T-BET+	22
TOX1+ LAG-3+ CD39+ T-BET+	22
LAG-3+ CD39+ EOMES+ CD44+ TCF-1+ T-BET+	22
PD-1+ TOX1+ LAG-3+ EOMES+ CD38+ CD44+ TCF-1+	22
PD-1+ LAG-3+ EOMES+ CD44+ TCF-1+	21
PD-1+ TOX1+ CD39+ CD44+ TCF-1+	21
PD-1+ EOMES+ CD44+ T-BET+	21
TIM3+ LAG-3+ CD38+ CD44+ TCF-1+ T-BET+	21
TIM3+ LAG-3+ EOMES+ TCF-1+	21
PD-1+ TOX1+ LAG-3+ EOMES+ CD38+ CD44+	21

TOX1+ TIM3+ EOMES+ TCF-1+ T-BET+	21
PD-1+ TOX1+ LAG-3+ CD39+ EOMES+ T-BET+	21
TOX1+ EOMES+ CD38+ T-BET+	21
TOX1+ LAG-3+ EOMES+ CD38+ TCF-1+	20
TIM3+ LAG-3+ TCF-1+	20
TOX1+ LAG-3+ CD39+ EOMES+ CD38+ CD44+	20
TOX1+ TIM3+ CD38+ TCF-1+ T-BET+	20
TOX1+ TIM3+ EOMES+ CD38+ CD44+ TCF-1+ T-BET+	20
PD-1+ TOX1+ TIM3+ CD44+	20
TOX1+ TIM3+ CD39+ TCF-1+	20
PD-1+ TOX1+ EOMES+ CD38+	20
EOMES+ CD38+ CD44+ T-BET+	20
PD-1+ TOX1+ CD38+ CD44+ TCF-1+	20
PD-1+ TOX1+ CD39+ EOMES+ T-BET+	19
TOX1+ CD39+ CD44+ T-BET+	19
TIM3+ LAG-3+ EOMES+ CD38+ CD44+ TCF-1+	19
LAG-3+ CD39+ T-BET+	19
TOX1+ TIM3+ LAG-3+ EOMES+ CD38+ TCF-1+	19
LAG-3+ EOMES+ CD38+	19
PD-1+ TOX1+ TIM3+ LAG-3+ CD39+ CD38+ CD44+ T-BET+	19
TOX1+ TIM3+ LAG-3+ EOMES+ CD38+ CD44+ TCF-1+	19
PD-1+ CD39+ EOMES+	18
CD39+ CD38+ CD44+ TCF-1+ T-BET+	18
TIM3+ CD39+ CD38+ CD44+	18
TIM3+ LAG-3+ EOMES+ CD38+ CD44+ TCF-1+ T-BET+	18
PD-1+ TOX1+ CD38+ TCF-1+	18
PD-1+ TOX1+ LAG-3+ EOMES+ TCF-1+ T-BET+	18
TIM3+ CD38+	18
TOX1+ LAG-3+ CD44+ TCF-1+	18
LAG-3+ CD39+ CD44+ TCF-1+	17
PD-1+ CD39+ TCF-1+	17
CD39+ CD38+ T-BET+	17
PD-1+ TOX1+ TIM3+ EOMES+ TCF-1+	17
TIM3+ CD38+ CD44+ TCF-1+ T-BET+	17
PD-1+ TOX1+ CD38+ T-BET+	17
PD-1+ TOX1+ EOMES+ CD38+ CD44+	17
PD-1+ TOX1+ CD39+ EOMES+ CD38+ CD44+	17
PD-1+ TOX1+ TIM3+ EOMES+	17
PD-1+ TOX1+ TIM3+ LAG-3+ CD39+ EOMES+ CD44+ TCF-1+	17
PD-1+ TOX1+ TIM3+ CD39+ CD38+ CD44+ TCF-1+ T-BET+	17
PD-1+ TOX1+ TIM3+ LAG-3+ CD44+ TCF-1+ T-BET+	17
TIM3+ EOMES+ CD44+ T-BET+	17
TOX1+ LAG-3+ CD39+ EOMES+ CD38+ TCF-1+ T-BET+	17
LAG-3+ CD39+ CD38+	17

PD-1+ TOX1+ TIM3+ CD38+ CD44+	16
PD-1+ TOX1+ TIM3+ LAG-3+ CD39+ EOMES+ CD38+ TCF-1+ T-BET+	16
LAG-3+ EOMES+ CD38+ TCF-1+ T-BET+	16
PD-1+ LAG-3+ T-BET+	16
CD39+ CD38+ CD44+ T-BET+	16
PD-1+ LAG-3+ TCF-1+ T-BET+	16
TOX1+ LAG-3+ EOMES+ CD38+	16
TOX1+ TIM3+ EOMES+ CD38+ TCF-1+	16
TOX1+ LAG-3+ CD39+ EOMES+ TCF-1+ T-BET+	16
PD-1+ TOX1+ LAG-3+ EOMES+ CD44+	15
TOX1+ LAG-3+ CD39+ EOMES+ CD44+ TCF-1+	15
PD-1+ TOX1+ LAG-3+ CD44+	15
PD-1+ LAG-3+ CD38+ TCF-1+	15
PD-1+ TOX1+ CD39+ EOMES+ CD44+ TCF-1+ T-BET+	14
PD-1+ TOX1+ EOMES+ CD38+ CD44+ TCF-1+	14
LAG-3+ CD39+ CD38+ CD44+ TCF-1+	14
LAG-3+ EOMES+ CD38+ CD44+ TCF-1+ T-BET+	14
LAG-3+ CD39+ CD38+ T-BET+	14
EOMES+ CD38+ T-BET+	14
TOX1+ LAG-3+ CD44+	14
PD-1+ TOX1+ LAG-3+ CD39+ CD44+ TCF-1+ T-BET+	14
TOX1+ TIM3+ EOMES+ CD44+ TCF-1+ T-BET+	14
PD-1+ TOX1+ TIM3+ CD39+ CD38+ CD44+ T-BET+	14
PD-1+ LAG-3+ CD39+	14
PD-1+ TOX1+ EOMES+ CD38+ CD44+ TCF-1+ T-BET+	14
PD-1+ LAG-3+ CD39+ T-BET+	14
TOX1+ LAG-3+ EOMES+ CD38+ CD44+ TCF-1+	14
TOX1+ EOMES+ CD38+ TCF-1+ T-BET+	14
TIM3+ LAG-3+ EOMES+ T-BET+	14
TIM3+ CD39+ EOMES+	14
PD-1+ TIM3+ T-BET+	14
PD-1+ CD39+ TCF-1+ T-BET+	14
PD-1+ TOX1+ LAG-3+ CD39+ TCF-1+ T-BET+	13
TOX1+ LAG-3+ CD38+ TCF-1+ T-BET+	13
PD-1+ TOX1+ CD38+ TCF-1+ T-BET+	13
TIM3+ LAG-3+ CD38+ TCF-1+ T-BET+	13
LAG-3+ CD39+ CD38+ TCF-1+ T-BET+	13
LAG-3+ CD39+ EOMES+ CD38+ TCF-1+ T-BET+	13
TOX1+ LAG-3+ EOMES+ CD38+ TCF-1+ T-BET+	13
TOX1+ LAG-3+ CD39+ EOMES+ CD38+ CD44+ TCF-1+	13
PD-1+ TOX1+ CD39+ EOMES+ CD44+	13
PD-1+ TIM3+ LAG-3+ CD38+ TCF-1+ T-BET+	13
PD-1+ TOX1+ TIM3+ CD44+ TCF-1+ T-BET+	13
TOX1+ CD39+ CD38+ CD44+	13

TOX1+ LAG-3+ CD39+ CD38+	13
TOX1+ TIM3+ CD39+ EOMES+	13
TOX1+ CD39+ CD38+ T-BET+	13
PD-1+ TOX1+ TIM3+ CD38+ TCF-1+ T-BET+	13
PD-1+ TOX1+ TIM3+ EOMES+ TCF-1+ T-BET+	13
LAG-3+ CD39+ CD38+ CD44+	12
TIM3+ CD39+ TCF-1+ T-BET+	12
PD-1+ TOX1+ LAG-3+ EOMES+ CD44+ TCF-1+	12
PD-1+ TOX1+ LAG-3+ CD39+ CD38+ TCF-1+	12
CD39+ CD38+ TCF-1+ T-BET+	12
PD-1+ TOX1+ LAG-3+ CD44+ TCF-1+	12
PD-1+ TOX1+ LAG-3+ CD44+ TCF-1+ T-BET+	12
PD-1+ TOX1+ CD39+ CD38+	12
PD-1+ TOX1+ EOMES+ CD38+ TCF-1+	12
TOX1+ LAG-3+ EOMES+ CD44+ TCF-1+	12
PD-1+ TOX1+ TIM3+ LAG-3+ EOMES+ TCF-1+	12
PD-1+ TIM3+ TCF-1+	12
TOX1+ LAG-3+ CD39+ CD38+ TCF-1+ T-BET+	12
TOX1+ TIM3+ EOMES+ CD38+ TCF-1+ T-BET+	12
PD-1+ LAG-3+ CD39+ EOMES+ TCF-1+	12
LAG-3+ EOMES+ CD44+ T-BET+	12
PD-1+ TIM3+ CD44+	12
TOX1+ LAG-3+ CD38+	12
TOX1+ LAG-3+ CD39+ EOMES+ CD38+ CD44+ TCF-1+ T-BET+	12
TOX1+ LAG-3+ CD44+ T-BET+	12
TIM3+ LAG-3+ CD39+	12
TIM3+ LAG-3+ EOMES+ CD38+ TCF-1+ T-BET+	12
TOX1+ LAG-3+ EOMES+ CD38+ CD44+	12
LAG-3+ CD38+ T-BET+	12
CD39+ EOMES+ CD38+ TCF-1+ T-BET+	12
TIM3+ LAG-3+ CD38+ T-BET+	12
PD-1+ CD39+ EOMES+ TCF-1+ T-BET+	12
TIM3+ LAG-3+ CD39+ EOMES+ CD44+ TCF-1+	12
PD-1+ CD39+ T-BET+	12
PD-1+ TOX1+ LAG-3+ CD39+ EOMES+ CD44+ TCF-1+	12
PD-1+ TOX1+ EOMES+ CD38+ TCF-1+ T-BET+	11
PD-1+ LAG-3+ EOMES+ CD44+ TCF-1+ T-BET+	11
PD-1+ LAG-3+ EOMES+ TCF-1+ T-BET+	11
LAG-3+ CD39+ EOMES+ CD38+ CD44+ TCF-1+ T-BET+	11
TOX1+ LAG-3+ CD39+ TCF-1+ T-BET+	11
TOX1+ CD39+ EOMES+ CD44+ T-BET+	11
PD-1+ LAG-3+ CD44+ TCF-1+	11
CD39+ EOMES+ CD38+ CD44+ TCF-1+ T-BET+	11
PD-1+ TOX1+ TIM3+ LAG-3+ CD38+ TCF-1+ T-BET+	11

TIM3+ CD38+ T-BET+	11
TOX1+ TIM3+ EOMES+ CD38+ CD44+	11
TIM3+ LAG-3+ EOMES+	11
TOX1+ TIM3+ EOMES+ CD44+ T-BET+	11
TOX1+ TIM3+ LAG-3+ CD39+ EOMES+ CD44+ TCF-1+ T-BET+	11
PD-1+ TOX1+ LAG-3+ CD39+ CD44+ TCF-1+	11
TIM3+ LAG-3+ CD44+	11
LAG-3+ CD39+ EOMES+ CD44+ TCF-1+	11
LAG-3+ CD39+ EOMES+ CD44+	11
PD-1+ TOX1+ TIM3+ CD38+	11
TOX1+ TIM3+ CD38+ T-BET+	11
PD-1+ TOX1+ LAG-3+ EOMES+ CD38+ CD44+ TCF-1+ T-BET+	11
PD-1+ CD38+	11
TOX1+ TIM3+ CD38+ TCF-1+	11
TIM3+ CD38+ TCF-1+ T-BET+	10
PD-1+ TOX1+ TIM3+ LAG-3+ EOMES+ CD44+ TCF-1+ T-BET+	10
PD-1+ TOX1+ LAG-3+ EOMES+ CD38+ CD44+ T-BET+	10
PD-1+ LAG-3+ CD39+ EOMES+ CD38+ CD44+ TCF-1+ T-BET+	10
TIM3+ CD38+ CD44+ T-BET+	10
TIM3+ LAG-3+ CD38+ CD44+ T-BET+	10
PD-1+ TIM3+ LAG-3+ CD39+ CD38+ CD44+ T-BET+	10
TIM3+ LAG-3+ EOMES+ TCF-1+ T-BET+	10
PD-1+ TOX1+ CD39+ CD38+ CD44+	10
PD-1+ LAG-3+ EOMES+ T-BET+	10
PD-1+ TOX1+ CD39+ EOMES+ CD44+ T-BET+	10
PD-1+ TOX1+ TIM3+ CD39+	10
PD-1+ TOX1+ CD39+ EOMES+ CD38+ CD44+ TCF-1+	10
PD-1+ TOX1+ TIM3+ LAG-3+	10
PD-1+ TOX1+ TIM3+ LAG-3+ CD38+ CD44+ T-BET+	10
TOX1+ LAG-3+ CD39+ EOMES+ T-BET+	10
LAG-3+ CD39+ CD44+	10
TIM3+ CD39+ CD44+ TCF-1+	10
TOX1+ TIM3+ LAG-3+ EOMES+ TCF-1+	10
TIM3+ EOMES+ CD38+ CD44+ TCF-1+ T-BET+	9
PD-1+ TIM3+ EOMES+ CD38+ CD44+ TCF-1+ T-BET+	9
TIM3+ CD39+ CD38+ TCF-1+	9
PD-1+ CD39+ CD44+ TCF-1+	9
PD-1+ CD38+ TCF-1+	9
PD-1+ LAG-3+ CD38+ CD44+ TCF-1+ T-BET+	9
PD-1+ TIM3+ CD44+ TCF-1+ T-BET+	9
TOX1+ EOMES+ CD38+ CD44+ T-BET+	9
PD-1+ TOX1+ LAG-3+ EOMES+ CD44+ TCF-1+ T-BET+	9
PD-1+ TOX1+ TIM3+ CD39+ TCF-1+ T-BET+	9
LAG-3+ CD39+ CD38+ CD44+ TCF-1+ T-BET+	9

PD-1+ TOX1+ TIM3+ CD39+ EOMES+ TCF-1+	9
TOX1+ TIM3+ CD39+ EOMES+ TCF-1+	9
TOX1+ LAG-3+ CD38+ T-BET+	9
PD-1+ TOX1+ LAG-3+ CD38+	9
PD-1+ TOX1+ TIM3+ LAG-3+ EOMES+	9
TOX1+ TIM3+ CD39+ CD38+ TCF-1+ T-BET+	9
TOX1+ TIM3+ CD38+ CD44+ TCF-1+	9
PD-1+ TOX1+ TIM3+ LAG-3+ CD39+ EOMES+ CD38+	9
TOX1+ LAG-3+ CD39+ CD44+ TCF-1+	9
TIM3+ CD38+ CD44+ TCF-1+	9
PD-1+ LAG-3+ EOMES+ CD38+ CD44+	8
TOX1+ LAG-3+ EOMES+ CD44+	8
PD-1+ TOX1+ TIM3+ CD39+ CD44+ TCF-1+ T-BET+	8
PD-1+ TOX1+ TIM3+ EOMES+ CD44+ TCF-1+	8
PD-1+ LAG-3+ CD39+ EOMES+ TCF-1+ T-BET+	8
PD-1+ TOX1+ TIM3+ EOMES+ CD44+	8
PD-1+ TOX1+ TIM3+ CD39+ EOMES+	8
PD-1+ LAG-3+ CD39+ CD38+ TCF-1+ T-BET+	8
PD-1+ TOX1+ TIM3+ CD44+ T-BET+	8
LAG-3+ EOMES+ CD38+ T-BET+	8
PD-1+ TOX1+ TIM3+ LAG-3+ CD38+ CD44+	8
PD-1+ TOX1+ TIM3+ LAG-3+ CD39+ CD44+ TCF-1+	8
CD39+ EOMES+ CD38+ CD44+ T-BET+	8
PD-1+ TOX1+ TIM3+ LAG-3+ CD39+ EOMES+ TCF-1+	8
CD39+ EOMES+ CD38+ T-BET+	8
CD39+ EOMES+ CD44+ T-BET+	8
PD-1+ CD39+ EOMES+ CD44+ TCF-1+	8
TOX1+ CD39+ CD38+ TCF-1+	8
PD-1+ CD39+ EOMES+ CD44+	8
PD-1+ TOX1+ TIM3+ LAG-3+ CD39+ EOMES+ CD38+ CD44+	8
TOX1+ LAG-3+ CD39+ CD44+ TCF-1+ T-BET+	8
PD-1+ CD39+ EOMES+ TCF-1+	8
TOX1+ TIM3+ LAG-3+ TCF-1+	8
PD-1+ TOX1+ CD39+ CD44+ T-BET+	8
PD-1+ TOX1+ CD39+ EOMES+ CD38+ CD44+ T-BET+	8
TOX1+ LAG-3+ CD39+ EOMES+ CD44+	8
PD-1+ TOX1+ LAG-3+ EOMES+ CD44+ T-BET+	8
PD-1+ TOX1+ CD39+ CD44+ TCF-1+ T-BET+	8
TOX1+ TIM3+ LAG-3+ CD39+ EOMES+ CD38+ TCF-1+ T-BET+	8
PD-1+ TOX1+ CD38+ CD44+ TCF-1+ T-BET+	8
PD-1+ TOX1+ LAG-3+ CD39+ CD38+ CD44+ TCF-1+ T-BET+	8
TIM3+ EOMES+ CD38+ CD44+	8
TIM3+ LAG-3+ EOMES+ CD44+ TCF-1+ T-BET+	8
PD-1+ TIM3+ EOMES+	8

TOX1+ TIM3+ LAG-3+ CD39+	8
TOX1+ TIM3+ LAG-3+ CD39+ CD38+ TCF-1+ T-BET+	8
PD-1+ TOX1+ CD39+ EOMES+ CD38+ CD44+ TCF-1+ T-BET+	8
PD-1+ LAG-3+ CD38+	7
TIM3+ EOMES+ CD38+	7
PD-1+ TOX1+ CD38+ CD44+ T-BET+	7
PD-1+ TOX1+ TIM3+ CD38+ T-BET+	7
PD-1+ TOX1+ TIM3+ LAG-3+ EOMES+ CD38+ CD44+	7
PD-1+ TOX1+ TIM3+ LAG-3+ EOMES+ CD38+ TCF-1+	7
PD-1+ TOX1+ LAG-3+ CD44+ T-BET+	7
PD-1+ TOX1+ TIM3+ CD39+ EOMES+ CD44+ TCF-1+ T-BET+	7
PD-1+ TOX1+ LAG-3+ CD39+ CD38+	7
PD-1+ TIM3+ LAG-3+ CD39+ EOMES+ CD38+ CD44+ TCF-1+	7
LAG-3+ CD39+ CD38+ TCF-1+	7
PD-1+ TOX1+ LAG-3+ CD39+ EOMES+ CD44+	7
PD-1+ TOX1+ LAG-3+ CD39+ EOMES+ CD44+ TCF-1+ T-BET+	7
PD-1+ TOX1+ LAG-3+ CD39+ EOMES+ CD38+ CD44+ T-BET+	7
PD-1+ TOX1+ EOMES+ CD38+ T-BET+	7
TOX1+ TIM3+ LAG-3+ CD39+ CD38+ T-BET+	7
TOX1+ LAG-3+ CD39+ CD38+ T-BET+	7
TIM3+ LAG-3+ CD38+ CD44+ TCF-1+	7
TOX1+ LAG-3+ EOMES+ CD38+ CD44+ TCF-1+ T-BET+	7
TOX1+ LAG-3+ CD39+ CD44+	7
TIM3+ LAG-3+ CD39+ CD38+ CD44+ TCF-1+ T-BET+	7
TOX1+ TIM3+ LAG-3+ CD38+ TCF-1+ T-BET+	7
TIM3+ LAG-3+ CD39+ EOMES+ TCF-1+	7
TOX1+ CD39+ EOMES+ CD38+ TCF-1+ T-BET+	7
PD-1+ CD38+ CD44+ TCF-1+	7
PD-1+ CD38+ CD44+	7
TOX1+ LAG-3+ CD39+ CD38+ CD44+ TCF-1+	7
TOX1+ TIM3+ LAG-3+ EOMES+ TCF-1+ T-BET+	7
TOX1+ LAG-3+ CD39+ CD38+ CD44+ TCF-1+ T-BET+	7
TIM3+ LAG-3+ CD39+ EOMES+ CD44+ TCF-1+ T-BET+	7
TIM3+ LAG-3+ TCF-1+ T-BET+	7
TOX1+ TIM3+ CD39+ TCF-1+ T-BET+	7
TOX1+ TIM3+ CD39+ T-BET+	7
TIM3+ LAG-3+ EOMES+ CD38+ TCF-1+	7
LAG-3+ EOMES+ CD38+ CD44+ T-BET+	6
TOX1+ TIM3+ LAG-3+ CD39+ CD38+ CD44+ T-BET+	6
PD-1+ TOX1+ LAG-3+ CD39+ EOMES+ CD38+ T-BET+	6
PD-1+ TOX1+ TIM3+ LAG-3+ CD39+ EOMES+ CD38+ T-BET+	6
LAG-3+ CD39+ EOMES+ T-BET+	6
PD-1+ TOX1+ TIM3+ CD39+ EOMES+ TCF-1+ T-BET+	6
TIM3+ LAG-3+ CD39+ EOMES+	6

PD-1+ TOX1+ CD39+ EOMES+ CD38+ TCF-1+ T-BET+	6
PD-1+ LAG-3+ EOMES+ CD38+ TCF-1+ T-BET+	6
PD-1+ TIM3+ LAG-3+ CD39+ EOMES+ TCF-1+ T-BET+	6
TOX1+ TIM3+ LAG-3+ CD44+ TCF-1+ T-BET+	6
TOX1+ TIM3+ LAG-3+ CD39+ EOMES+	6
TOX1+ LAG-3+ CD44+ TCF-1+ T-BET+	6
LAG-3+ CD39+ EOMES+ CD38+ T-BET+	6
PD-1+ TOX1+ TIM3+ LAG-3+ TCF-1+ T-BET+	6
TIM3+ LAG-3+ CD39+ CD38+	6
TOX1+ TIM3+ CD39+ CD38+ CD44+	6
PD-1+ TIM3+ CD44+ TCF-1+	6
TOX1+ LAG-3+ CD39+ CD44+ T-BET+	6
PD-1+ CD39+ CD38+ T-BET+	6
TOX1+ CD39+ CD38+ CD44+ TCF-1+	6
TIM3+ CD39+ CD44+ TCF-1+ T-BET+	6
TIM3+ EOMES+ CD38+ TCF-1+ T-BET+	6
PD-1+ TOX1+ TIM3+ CD39+ T-BET+	6
TOX1+ LAG-3+ EOMES+ CD38+ T-BET+	6
PD-1+ TOX1+ TIM3+ CD39+ TCF-1+	6
PD-1+ LAG-3+ CD44+	6
PD-1+ LAG-3+ CD44+ T-BET+	6
LAG-3+ CD39+ CD44+ TCF-1+ T-BET+	6
PD-1+ TIM3+ EOMES+ CD44+ TCF-1+	6
TOX1+ TIM3+ CD39+ CD44+	6
TIM3+ CD39+ CD38+ T-BET+	6
TOX1+ CD39+ CD38+ CD44+ TCF-1+ T-BET+	6
PD-1+ TOX1+ LAG-3+ CD38+ TCF-1+ T-BET+	6
PD-1+ TOX1+ TIM3+ LAG-3+ CD39+ TCF-1+ T-BET+	6
TIM3+ CD39+ CD38+ TCF-1+ T-BET+	6
PD-1+ CD38+ TCF-1+ T-BET+	6
TOX1+ CD39+ EOMES+ CD38+ T-BET+	6
PD-1+ LAG-3+ CD39+ EOMES+ T-BET+	6
TIM3+ LAG-3+ CD39+ CD38+ T-BET+	6
PD-1+ TOX1+ LAG-3+ EOMES+ CD38+ T-BET+	5
PD-1+ TIM3+ LAG-3+ EOMES+ CD38+ TCF-1+	5
TOX1+ TIM3+ CD39+ CD38+ CD44+ T-BET+	5
TOX1+ TIM3+ LAG-3+ EOMES+ CD38+ T-BET+	5
PD-1+ TOX1+ LAG-3+ EOMES+ CD38+ TCF-1+ T-BET+	5
TOX1+ TIM3+ CD39+ CD38+ T-BET+	5
TOX1+ TIM3+ CD39+ CD38+	5
TOX1+ TIM3+ LAG-3+ CD39+ CD38+	5
PD-1+ TIM3+ EOMES+ TCF-1+ T-BET+	5
PD-1+ TIM3+ EOMES+ CD44+ TCF-1+ T-BET+	5
PD-1+ TOX1+ TIM3+ CD38+ CD44+ TCF-1+	5

TOX1+ LAG-3+ CD39+ CD38+ TCF-1+	5
TOX1+ LAG-3+ CD39+ EOMES+ TCF-1+	5
PD-1+ TOX1+ LAG-3+ CD39+ CD44+	5
PD-1+ TOX1+ LAG-3+ CD39+ CD38+ T-BET+	5
PD-1+ TOX1+ LAG-3+ CD39+ CD38+ TCF-1+ T-BET+	5
TOX1+ TIM3+ CD39+ CD44+ TCF-1+	5
TOX1+ LAG-3+ CD38+ CD44+	5
TOX1+ TIM3+ LAG-3+ CD38+ TCF-1+	5
PD-1+ LAG-3+ CD39+ TCF-1+ T-BET+	5
TOX1+ CD39+ EOMES+ CD38+ CD44+ TCF-1+ T-BET+	5
PD-1+ LAG-3+ CD39+ EOMES+ CD44+ TCF-1+	5
PD-1+ LAG-3+ EOMES+ CD44+	5
PD-1+ EOMES+ CD38+ TCF-1+	5
TIM3+ LAG-3+ CD38+ TCF-1+	5
PD-1+ TOX1+ TIM3+ LAG-3+ CD39+ CD44+	5
TOX1+ TIM3+ LAG-3+ CD38+ CD44+ TCF-1+	5
TOX1+ TIM3+ LAG-3+ EOMES+	5
TIM3+ CD39+ EOMES+ TCF-1+ T-BET+	5
TOX1+ TIM3+ LAG-3+ EOMES+ CD44+ TCF-1+ T-BET+	5
TIM3+ EOMES+ CD38+ CD44+ T-BET+	5
PD-1+ TOX1+ TIM3+ LAG-3+ CD39+ EOMES+	5
PD-1+ TOX1+ TIM3+ LAG-3+ CD39+ EOMES+ TCF-1+ T-BET+	5
PD-1+ CD39+ CD38+ TCF-1+	5
TIM3+ LAG-3+ CD39+ EOMES+ CD38+ CD44+ TCF-1+	5
PD-1+ LAG-3+ CD39+ TCF-1+	5
PD-1+ TOX1+ LAG-3+ CD39+ CD38+ CD44+ T-BET+	5
PD-1+ LAG-3+ CD39+ EOMES+	5
PD-1+ TOX1+ LAG-3+ CD38+ CD44+	5
TOX1+ TIM3+ CD39+ EOMES+ CD44+ TCF-1+	5
TOX1+ TIM3+ LAG-3+ TCF-1+ T-BET+	5
PD-1+ TOX1+ LAG-3+ CD38+ CD44+ TCF-1+ T-BET+	5
PD-1+ TIM3+ LAG-3+ CD39+ CD38+ T-BET+	5
PD-1+ TOX1+ LAG-3+ CD38+ T-BET+	5
TIM3+ LAG-3+ CD38+	5
PD-1+ LAG-3+ CD39+ CD44+ TCF-1+	5
TOX1+ LAG-3+ CD38+ TCF-1+	5
TIM3+ LAG-3+ CD39+ CD38+ TCF-1+ T-BET+	5
PD-1+ TIM3+ LAG-3+ EOMES+ CD38+ CD44+ TCF-1+	4
PD-1+ TIM3+ LAG-3+ T-BET+	4
TOX1+ TIM3+ LAG-3+ CD39+ CD38+ CD44+	4
TIM3+ EOMES+ CD38+ TCF-1+	4
TOX1+ TIM3+ CD39+ EOMES+ TCF-1+ T-BET+	4
TIM3+ EOMES+ CD38+ T-BET+	4
TOX1+ TIM3+ CD39+ CD38+ CD44+ TCF-1+	4

PD-1+ TIM3+ LAG-3+ CD38+ CD44+ TCF-1+ T-BET+	4
TOX1+ TIM3+ CD39+ EOMES+ CD44+ TCF-1+ T-BET+	4
PD-1+ TOX1+ CD39+ CD38+ T-BET+	4
TOX1+ TIM3+ LAG-3+ CD39+ EOMES+ CD38+ CD44+	4
TOX1+ TIM3+ LAG-3+ CD39+ EOMES+ CD38+ CD44+ T-BET+	4
PD-1+ TOX1+ LAG-3+ CD39+ CD38+ CD44+ TCF-1+	4
PD-1+ TIM3+ LAG-3+ CD39+ EOMES+ CD38+ CD44+ T-BET+	4
PD-1+ TIM3+ LAG-3+ EOMES+ CD38+ TCF-1+ T-BET+	4
PD-1+ TIM3+ EOMES+ TCF-1+	4
TIM3+ LAG-3+ EOMES+ CD44+ T-BET+	4
PD-1+ EOMES+ CD38+ CD44+ TCF-1+ T-BET+	4
PD-1+ TOX1+ TIM3+ LAG-3+ CD39+ CD38+ TCF-1+ T-BET+	4
PD-1+ TOX1+ TIM3+ CD39+ CD38+ CD44+	4
TOX1+ LAG-3+ CD38+ CD44+ TCF-1+	4
TOX1+ LAG-3+ CD38+ CD44+ T-BET+	4
PD-1+ CD39+ CD44+	4
PD-1+ LAG-3+ CD39+ CD44+ TCF-1+ T-BET+	4
TIM3+ CD39+ EOMES+ CD44+ TCF-1+	4
PD-1+ LAG-3+ CD44+ TCF-1+ T-BET+	4
PD-1+ TIM3+ TCF-1+ T-BET+	4
PD-1+ EOMES+ CD38+ CD44+ TCF-1+	4
TIM3+ LAG-3+ CD39+ CD38+ CD44+ T-BET+	4
PD-1+ LAG-3+ CD38+ T-BET+	4
PD-1+ TOX1+ TIM3+ LAG-3+ CD39+ CD44+ T-BET+	4
PD-1+ TOX1+ TIM3+ LAG-3+ CD38+ CD44+ TCF-1+	4
PD-1+ TOX1+ TIM3+ LAG-3+ CD39+ TCF-1+	4
PD-1+ TOX1+ TIM3+ LAG-3+ EOMES+ TCF-1+ T-BET+	4
PD-1+ LAG-3+ CD39+ EOMES+ CD38+ CD44+ TCF-1+	4
PD-1+ LAG-3+ CD39+ EOMES+ CD44+ TCF-1+ T-BET+	4
PD-1+ TOX1+ TIM3+ EOMES+ T-BET+	4
TOX1+ LAG-3+ CD39+ CD38+ CD44+	4
PD-1+ TIM3+ CD44+ T-BET+	4
PD-1+ TOX1+ TIM3+ EOMES+ CD44+ TCF-1+ T-BET+	4
TOX1+ TIM3+ CD38+ CD44+ T-BET+	4
TOX1+ LAG-3+ EOMES+ CD38+ CD44+ T-BET+	4
PD-1+ TOX1+ TIM3+ LAG-3+ CD39+ EOMES+ CD44+ T-BET+	4
PD-1+ TOX1+ TIM3+ EOMES+ CD44+ T-BET+	4
PD-1+ TIM3+ CD39+ TCF-1+	4
PD-1+ TOX1+ TIM3+ EOMES+ CD38+ CD44+ TCF-1+	4
PD-1+ TIM3+ EOMES+ CD44+ T-BET+	4
TIM3+ LAG-3+ CD39+ EOMES+ CD38+ CD44+	3
TOX1+ CD39+ CD38+ TCF-1+ T-BET+	3
TIM3+ LAG-3+ CD39+ EOMES+ CD38+ TCF-1+	3
PD-1+ TOX1+ TIM3+ LAG-3+ CD39+ CD38+ CD44+ TCF-1+	3

TOX1+ TIM3+ LAG-3+ CD38+ CD44+ T-BET+	3
TOX1+ TIM3+ LAG-3+ CD39+ TCF-1+ T-BET+	3
PD-1+ TOX1+ EOMES+ CD38+ CD44+ T-BET+	3
TOX1+ TIM3+ LAG-3+ EOMES+ CD44+	3
TIM3+ CD38+ TCF-1+	3
TIM3+ LAG-3+ CD39+ EOMES+ CD38+	3
TOX1+ TIM3+ LAG-3+ EOMES+ CD44+ TCF-1+	3
TIM3+ LAG-3+ CD39+ EOMES+ CD44+ T-BET+	3
PD-1+ TOX1+ TIM3+ LAG-3+ CD39+ CD38+ T-BET+	3
TOX1+ TIM3+ LAG-3+ CD38+ CD44+	3
PD-1+ TOX1+ TIM3+ LAG-3+ CD39+	3
TOX1+ TIM3+ LAG-3+ T-BET+	3
PD-1+ TOX1+ TIM3+ LAG-3+ EOMES+ CD38+ CD44+ T-BET+	3
TIM3+ LAG-3+ CD39+ EOMES+ TCF-1+ T-BET+	3
TIM3+ LAG-3+ EOMES+ CD38+ T-BET+	3
TIM3+ LAG-3+ CD39+ T-BET+	3
TIM3+ LAG-3+ EOMES+ CD44+	3
TIM3+ LAG-3+ CD39+ TCF-1+	3
TIM3+ LAG-3+ CD39+ TCF-1+ T-BET+	3
TOX1+ TIM3+ CD39+ CD44+ T-BET+	3
TIM3+ LAG-3+ CD39+ CD44+ TCF-1+ T-BET+	3
TOX1+ LAG-3+ EOMES+ CD44+ TCF-1+ T-BET+	3
PD-1+ TOX1+ TIM3+ CD39+ CD44+ TCF-1+	3
TIM3+ LAG-3+ CD39+ CD38+ CD44+	3
TOX1+ LAG-3+ CD38+ CD44+ TCF-1+ T-BET+	3
PD-1+ TOX1+ LAG-3+ CD38+ CD44+ TCF-1+	3
PD-1+ TOX1+ TIM3+ CD39+ EOMES+ CD38+ TCF-1+ T-BET+	3
PD-1+ TOX1+ TIM3+ CD39+ EOMES+ CD38+ CD44+	3
LAG-3+ CD38+ CD44+ T-BET+	3
TOX1+ TIM3+ CD39+ EOMES+ CD38+ TCF-1+ T-BET+	3
TOX1+ TIM3+ CD39+ EOMES+ CD38+ CD44+ T-BET+	3
TIM3+ LAG-3+ EOMES+ CD44+ TCF-1+	3
PD-1+ TOX1+ TIM3+ LAG-3+ T-BET+	3
PD-1+ TOX1+ TIM3+ LAG-3+ CD44+ TCF-1+	3
LAG-3+ CD39+ EOMES+ CD38+ CD44+ T-BET+	3
TIM3+ LAG-3+ CD39+ CD38+ CD44+ TCF-1+	3
PD-1+ TOX1+ TIM3+ LAG-3+ EOMES+ T-BET+	3
TOX1+ TIM3+ LAG-3+ CD39+ CD44+ T-BET+	3
PD-1+ LAG-3+ CD39+ EOMES+ CD38+ T-BET+	3
TIM3+ LAG-3+ CD44+ TCF-1+	3
PD-1+ TIM3+ EOMES+ CD38+ TCF-1+	3
TIM3+ CD39+ CD44+ T-BET+	3
PD-1+ LAG-3+ CD39+ EOMES+ CD44+	3
TIM3+ LAG-3+ CD44+ TCF-1+ T-BET+	3

PD-1+ EOMES+ CD38+	3
PD-1+ TIM3+ EOMES+ CD44+	3
TIM3+ CD39+ EOMES+ CD44+ TCF-1+ T-BET+	3
PD-1+ LAG-3+ EOMES+ CD38+	3
PD-1+ LAG-3+ EOMES+ CD38+ TCF-1+	3
PD-1+ TIM3+ EOMES+ T-BET+	3
PD-1+ TIM3+ LAG-3+ CD39+ EOMES+ CD44+ TCF-1+	3
PD-1+ LAG-3+ EOMES+ CD38+ CD44+ TCF-1+	3
PD-1+ TIM3+ LAG-3+ CD39+ EOMES+ TCF-1+	3
PD-1+ LAG-3+ EOMES+ CD38+ CD44+ TCF-1+ T-BET+	3
PD-1+ CD38+ T-BET+	3
TIM3+ CD39+ CD38+ CD44+ TCF-1+ T-BET+	3
PD-1+ TIM3+ LAG-3+ EOMES+ TCF-1+ T-BET+	3
PD-1+ LAG-3+ CD39+ EOMES+ CD38+ TCF-1+	3
PD-1+ TIM3+ LAG-3+ CD39+ CD44+ TCF-1+ T-BET+	3
TIM3+ CD39+ EOMES+ CD38+ CD44+ TCF-1+	3
PD-1+ TIM3+ LAG-3+ EOMES+ CD44+ TCF-1+ T-BET+	3
TIM3+ CD39+ EOMES+ CD38+ CD44+ TCF-1+ T-BET+	3
PD-1+ TIM3+ LAG-3+ CD38+ TCF-1+	3
TOX1+ TIM3+ LAG-3+ CD39+ EOMES+ CD38+ TCF-1+	3
PD-1+ CD38+ CD44+ TCF-1+ T-BET+	3
PD-1+ TIM3+ CD39+ EOMES+ CD44+ TCF-1+	3
PD-1+ CD39+ CD38+	3
PD-1+ CD39+ EOMES+ T-BET+	3
PD-1+ CD39+ EOMES+ CD38+ TCF-1+	3
PD-1+ CD39+ CD38+ TCF-1+ T-BET+	3
TOX1+ TIM3+ LAG-3+ CD39+ EOMES+ TCF-1+ T-BET+	3
PD-1+ CD39+ EOMES+ CD44+ TCF-1+ T-BET+	3
PD-1+ CD39+ EOMES+ CD38+ CD44+ T-BET+	3
PD-1+ TIM3+ CD39+ EOMES+ CD38+ CD44+ TCF-1+ T-BET+	3
PD-1+ CD39+ EOMES+ CD38+ CD44+ TCF-1+ T-BET+	3
PD-1+ TIM3+ CD39+	3
PD-1+ TIM3+ CD39+ CD38+ CD44+ TCF-1+ T-BET+	3
PD-1+ TIM3+ EOMES+ CD38+ CD44+ TCF-1+	3
PD-1+ CD39+ CD44+ T-BET+	3
PD-1+ LAG-3+ CD39+ EOMES+ CD38+	2
PD-1+ TOX1+ TIM3+ CD39+ CD38+ CD44+ TCF-1+	2
TOX1+ LAG-3+ EOMES+ CD44+ T-BET+	2
PD-1+ LAG-3+ CD39+ EOMES+ CD38+ CD44+ T-BET+	2
PD-1+ TIM3+ EOMES+ CD38+ CD44+	2
PD-1+ TIM3+ CD39+ CD38+ T-BET+	2
TIM3+ LAG-3+ EOMES+ CD38+ CD44+ T-BET+	2
PD-1+ TOX1+ TIM3+ EOMES+ CD38+ CD44+	2
PD-1+ TIM3+ EOMES+ CD38+ CD44+ T-BET+	2

PD-1+ TIM3+ CD39+ CD44+ T-BET+	2
TOX1+ LAG-3+ CD39+ EOMES+ CD38+ T-BET+	2
TIM3+ LAG-3+ CD44+ T-BET+	2
TIM3+ LAG-3+ CD39+ CD44+ TCF-1+	2
TOX1+ TIM3+ LAG-3+ CD39+ CD44+ TCF-1+	2
TOX1+ LAG-3+ CD39+ CD38+ CD44+ T-BET+	2
PD-1+ TIM3+ CD38+ CD44+ TCF-1+ T-BET+	2
PD-1+ TOX1+ TIM3+ LAG-3+ CD44+	2
PD-1+ LAG-3+ CD39+ CD38+ CD44+ T-BET+	2
PD-1+ TOX1+ TIM3+ CD39+ EOMES+ CD38+ TCF-1+	2
PD-1+ CD39+ CD38+ CD44+ TCF-1+ T-BET+	2
TIM3+ LAG-3+ CD39+ EOMES+ CD38+ TCF-1+ T-BET+	2
PD-1+ TOX1+ TIM3+ LAG-3+ CD39+ EOMES+ T-BET+	2
PD-1+ CD39+ EOMES+ CD38+ T-BET+	2
TIM3+ LAG-3+ CD39+ EOMES+ CD38+ T-BET+	2
PD-1+ TOX1+ TIM3+ LAG-3+ CD39+ CD38+ CD44+	2
PD-1+ CD39+ EOMES+ CD38+ CD44+ TCF-1+	2
PD-1+ TOX1+ TIM3+ LAG-3+ CD39+ CD38+	2
TIM3+ CD39+ EOMES+ CD44+	2
TIM3+ CD39+ EOMES+ TCF-1+	2
PD-1+ LAG-3+ CD38+ CD44+ TCF-1+	2
TIM3+ LAG-3+ CD39+ EOMES+ CD44+	2
TIM3+ CD39+ EOMES+ T-BET+	2
PD-1+ EOMES+ CD38+ TCF-1+ T-BET+	2
TOX1+ CD39+ EOMES+ CD38+ CD44+ T-BET+	2
PD-1+ TOX1+ TIM3+ LAG-3+ EOMES+ CD44+ TCF-1+	2
PD-1+ TOX1+ TIM3+ LAG-3+ EOMES+ CD44+	2
TIM3+ LAG-3+ CD39+ EOMES+ T-BET+	2
TIM3+ CD39+ EOMES+ CD38+ T-BET+	2
PD-1+ LAG-3+ EOMES+ CD38+ CD44+ T-BET+	2
PD-1+ TOX1+ TIM3+ LAG-3+ CD38+ T-BET+	2
PD-1+ TOX1+ TIM3+ LAG-3+ CD38+	2
PD-1+ TOX1+ TIM3+ LAG-3+ CD44+ T-BET+	2
PD-1+ TIM3+ CD39+ EOMES+ TCF-1+ T-BET+	2
TIM3+ CD39+ EOMES+ CD38+ CD44+	2
PD-1+ TOX1+ TIM3+ LAG-3+ TCF-1+	2
PD-1+ LAG-3+ CD39+ CD38+	2
PD-1+ LAG-3+ CD39+ CD38+ T-BET+	2
PD-1+ TOX1+ TIM3+ CD39+ EOMES+ CD38+ CD44+ T-BET+	2
PD-1+ TOX1+ LAG-3+ CD39+ EOMES+ CD44+ T-BET+	2
PD-1+ CD39+ CD38+ CD44+	2
TIM3+ LAG-3+ EOMES+ CD38+	2
TOX1+ TIM3+ LAG-3+ CD39+ EOMES+ CD44+ TCF-1+	2
PD-1+ CD39+ CD38+ CD44+ T-BET+	2

TOX1+ TIM3+ LAG-3+ EOMES+ CD38+	2
TOX1+ TIM3+ LAG-3+ CD39+ EOMES+ TCF-1+	2
TOX1+ TIM3+ LAG-3+ CD39+ EOMES+ CD44+	2
PD-1+ TOX1+ CD39+ CD38+ TCF-1+	2
PD-1+ TOX1+ CD39+ CD38+ CD44+ T-BET+	2
PD-1+ TIM3+ LAG-3+ EOMES+ CD44+ T-BET+	2
PD-1+ TIM3+ LAG-3+ EOMES+ CD44+ TCF-1+	2
TOX1+ TIM3+ CD39+ EOMES+ T-BET+	2
PD-1+ TOX1+ CD39+ CD38+ CD44+ TCF-1+ T-BET+	2
PD-1+ TIM3+ LAG-3+ CD39+ T-BET+	2
TOX1+ TIM3+ LAG-3+ EOMES+ CD38+ CD44+	2
TOX1+ TIM3+ LAG-3+ EOMES+ T-BET+	2
TOX1+ TIM3+ LAG-3+ CD39+ EOMES+ CD38+ T-BET+	2
TIM3+ CD39+ CD38+ CD44+ T-BET+	2
PD-1+ TIM3+ LAG-3+ CD39+ CD44+ T-BET+	2
PD-1+ TOX1+ LAG-3+ CD38+ CD44+ T-BET+	2
PD-1+ TOX1+ LAG-3+ CD38+ TCF-1+	2
PD-1+ TIM3+ LAG-3+ CD39+ EOMES+ CD38+ T-BET+	2
PD-1+ TIM3+ LAG-3+ CD39+ CD38+ CD44+ TCF-1+	2
TOX1+ TIM3+ LAG-3+ CD44+ TCF-1+	2
PD-1+ TIM3+ LAG-3+ CD39+ EOMES+ T-BET+	2
PD-1+ TIM3+ LAG-3+ EOMES+	2
PD-1+ TIM3+ LAG-3+ EOMES+ T-BET+	2
LAG-3+ CD39+ CD38+ CD44+ T-BET+	2
TOX1+ TIM3+ EOMES+ CD38+ CD44+ T-BET+	2
PD-1+ TIM3+ CD39+ EOMES+ CD44+	2
TOX1+ TIM3+ EOMES+ CD38+	2
TOX1+ TIM3+ EOMES+ CD38+ T-BET+	2
TOX1+ TIM3+ LAG-3+ CD39+ CD38+ TCF-1+	2
PD-1+ TIM3+ CD39+ EOMES+ CD38+ TCF-1+ T-BET+	2
TIM3+ LAG-3+ CD38+ CD44+	2
PD-1+ TIM3+ CD39+ EOMES+ CD38+ CD44+ T-BET+	2
PD-1+ TOX1+ LAG-3+ CD39+ CD38+ CD44+	2
TOX1+ TIM3+ LAG-3+ CD44+	2
PD-1+ TIM3+ LAG-3+ TCF-1+ T-BET+	2
PD-1+ TOX1+ LAG-3+ CD39+ CD44+ T-BET+	2
PD-1+ TIM3+ LAG-3+ CD38+ T-BET+	2
TOX1+ TIM3+ LAG-3+ EOMES+ CD38+ CD44+ T-BET+	2
TOX1+ TIM3+ LAG-3+ CD39+ CD44+	1
TOX1+ TIM3+ LAG-3+ CD39+ CD38+ CD44+ TCF-1+	1
PD-1+ TIM3+ LAG-3+ CD39+ EOMES+ CD38+ CD44+	1
PD-1+ CD39+ EOMES+ CD38+ CD44+	1
PD-1+ TIM3+ LAG-3+ CD39+ EOMES+ CD38+ TCF-1+	1
PD-1+ CD39+ EOMES+ CD38+	1

TOX1+ TIM3+ LAG-3+ EOMES+ CD44+ T-BET+	1
PD-1+ TOX1+ TIM3+ LAG-3+ EOMES+ CD38+	1
PD-1+ LAG-3+ EOMES+ CD38+ T-BET+	1
TIM3+ LAG-3+ CD39+ EOMES+ CD38+ CD44+ T-BET+	1
TOX1+ TIM3+ LAG-3+ CD38+	1
PD-1+ TIM3+ LAG-3+ CD39+ EOMES+ CD44+ TCF-1+ T-BET+	1
PD-1+ CD39+ CD38+ CD44+ TCF-1+	1
TOX1+ TIM3+ LAG-3+ CD44+ T-BET+	1
TOX1+ TIM3+ LAG-3+ CD38+ T-BET+	1
PD-1+ TOX1+ TIM3+ LAG-3+ EOMES+ CD38+ T-BET+	1
PD-1+ TOX1+ TIM3+ LAG-3+ CD38+ TCF-1+	1
TOX1+ TIM3+ LAG-3+ CD39+ T-BET+	1
PD-1+ TOX1+ CD39+ CD38+ TCF-1+ T-BET+	1
PD-1+ EOMES+ CD38+ CD44+ T-BET+	1
PD-1+ TOX1+ CD39+ CD38+ CD44+ TCF-1+	1
PD-1+ LAG-3+ CD38+ CD44+	1
PD-1+ TOX1+ TIM3+ LAG-3+ CD39+ EOMES+ CD44+	1
PD-1+ LAG-3+ CD38+ CD44+ T-BET+	1
PD-1+ TOX1+ TIM3+ LAG-3+ CD39+ T-BET+	1
PD-1+ CD39+ EOMES+ CD44+ T-BET+	1
PD-1+ LAG-3+ EOMES+ CD44+ T-BET+	1
PD-1+ TOX1+ TIM3+ LAG-3+ CD39+ CD38+ TCF-1+	1
TOX1+ TIM3+ LAG-3+ CD39+ EOMES+ CD44+ T-BET+	1
PD-1+ EOMES+ CD38+ CD44+	1
TOX1+ TIM3+ LAG-3+ CD39+ EOMES+ T-BET+	1
TOX1+ TIM3+ LAG-3+ CD39+ EOMES+ CD38+	1
PD-1+ EOMES+ CD38+ T-BET+	1
TOX1+ CD39+ CD38+ CD44+ T-BET+	1
TOX1+ TIM3+ LAG-3+ CD39+ TCF-1+	1
PD-1+ TIM3+ LAG-3+ CD39+ CD38+ TCF-1+	1
PD-1+ TIM3+ LAG-3+ CD39+ EOMES+	1
TIM3+ CD39+ EOMES+ CD38+ TCF-1+ T-BET+	1
TOX1+ TIM3+ CD39+ CD38+ TCF-1+	1
PD-1+ TOX1+ TIM3+ EOMES+ CD38+ TCF-1+ T-BET+	1
PD-1+ TOX1+ TIM3+ EOMES+ CD38+ TCF-1+	1
PD-1+ TIM3+ CD38+	1
PD-1+ TIM3+ CD38+ T-BET+	1
PD-1+ TIM3+ CD38+ TCF-1+	1
PD-1+ TIM3+ CD38+ TCF-1+ T-BET+	1
PD-1+ TIM3+ CD38+ CD44+	1
PD-1+ TIM3+ LAG-3+ CD38+ CD44+ TCF-1+	1
PD-1+ TIM3+ LAG-3+ CD38+ CD44+ T-BET+	1
PD-1+ TIM3+ LAG-3+ CD44+ T-BET+	1
PD-1+ TIM3+ LAG-3+ CD44+	1

PD-1+ TIM3+ LAG-3+ TCF-1+	1
PD-1+ TIM3+ CD39+ T-BET+	1
TIM3+ LAG-3+ CD39+ CD44+ T-BET+	1
PD-1+ TIM3+ CD39+ TCF-1+ T-BET+	1
TIM3+ LAG-3+ CD39+ CD44+	1
TOX1+ LAG-3+ CD39+ EOMES+ CD38+ CD44+ T-BET+	1
PD-1+ TIM3+ CD39+ CD44+	1
LAG-3+ CD39+ CD44+ T-BET+	1
PD-1+ TIM3+ CD39+ CD38+	1
PD-1+ TIM3+ CD39+ CD38+ CD44+ T-BET+	1
TIM3+ LAG-3+ EOMES+ CD38+ CD44+	1
PD-1+ TOX1+ TIM3+ EOMES+ CD38+ CD44+ T-BET+	1
PD-1+ TIM3+ LAG-3+ EOMES+ TCF-1+	1
PD-1+ CD38+ CD44+ T-BET+	1
TOX1+ TIM3+ CD39+ EOMES+ CD38+	1
TOX1+ TIM3+ CD39+ EOMES+ CD38+ CD44+ TCF-1+	1
PD-1+ TIM3+ LAG-3+ CD39+ CD38+ CD44+ TCF-1+ T-BET+	1
PD-1+ TIM3+ LAG-3+ CD39+ CD38+ TCF-1+ T-BET+	1
PD-1+ LAG-3+ CD39+ CD44+	1
PD-1+ LAG-3+ CD39+ CD44+ T-BET+	1
PD-1+ TIM3+ CD39+ EOMES+ TCF-1+	1
PD-1+ LAG-3+ CD39+ CD38+ TCF-1+	1
PD-1+ TIM3+ LAG-3+ CD39+ TCF-1+ T-BET+	1
PD-1+ TOX1+ TIM3+ CD39+ EOMES+ CD38+	1
PD-1+ LAG-3+ CD39+ CD38+ CD44+	1
PD-1+ LAG-3+ CD39+ CD38+ CD44+ TCF-1+	1
PD-1+ TIM3+ LAG-3+ EOMES+ CD44+	1
LAG-3+ CD39+ EOMES+ CD44+ T-BET+	1
TIM3+ CD39+ CD38+ CD44+ TCF-1+	1
TOX1+ TIM3+ CD39+ EOMES+ CD44+ T-BET+	1
TIM3+ LAG-3+ CD39+ CD38+ TCF-1+	1
PD-1+ LAG-3+ CD39+ EOMES+ CD44+ T-BET+	1
PD-1+ TOX1+ TIM3+ CD39+ CD38+ T-BET+	1
PD-1+ TOX1+ TIM3+ CD39+ CD38+	1
PD-1+ TOX1+ TIM3+ CD39+ CD44+ T-BET+	1
PD-1+ TOX1+ TIM3+ CD39+ CD44+	1
PD-1+ LAG-3+ CD39+ EOMES+ CD38+ TCF-1+ T-BET+	1
TOX1+ TIM3+ LAG-3+ CD39+ CD44+ TCF-1+ T-BET+	1

Supplementary Table S5. Raw counts of cell-cell spatial interactions present in the dataset.

Cell-Cell Spatial Interaction	Count
Ki-67- Neoplastic & Ki-67- Neoplastic	2876770
Myeloid cells & Myeloid cells	1480053
Myeloid cells & Ki-67- Neoplastic	465886
B cells & B cells	450530
Ki-67- Neoplastic & Ki-67+ Neoplastic	437638
CD44- CD4 Th & CD44- CD4 Th	226250
Mesenchymal & Mesenchymal	220227
CD44- CD4 Th & B cells	219910
CD44- CD8 T Other & CD44- CD4 Th	206383
Mesenchymal & Ki-67- Neoplastic	202107
Ki-67+ Neoplastic & Ki-67+ Neoplastic	165702
CD44- CD8 T Other & CD44- CD8 T Other	158210
CD44- CD8 T Other & B cells	111164
CD44- CD4 Th & Myeloid cells	107677
Myeloid cells & Mesenchymal	90234
CD44- CD8 T Other & Myeloid cells	89976
B cells & Myeloid cells	62552
Myeloid cells & Ki-67+ Neoplastic	58793
CD44- CD8 T Other & Ki-67- Neoplastic	49618
B cells & Ki-67- Neoplastic	49336
CD44- CD4 Th & Ki-67- Neoplastic	48406
CD44- CD4 Th1 Other & CD44- CD4 Th	42570
CD44- CD8 T Other & CD44- CD4 Th1 Other	34844
CD44- CD4 Th & mTREG	32692
CD44- CD4 Th & CD44+ CD4 Th	31233
CD44- CD4 Th & Mesenchymal	29024
CD44- CD8 T Other & mTREG	27872
CD44+ CD4 Th & B cells	27606
CD44- CD8 T Other & Mesenchymal	26494
CD44+ CD4 Th & CD44+ CD4 Th	24718
CD44+ CD4 Th & Myeloid cells	24454
CD44- CD4 Th1 Other & B cells	24437
CD44+ CD8 T Other & Myeloid cells	23784
mTREG & Myeloid cells	23570
CD44- CD8 T Other & CD44+ CD8 T Other	23249
Naive TREG & B cells	23177
CD44- CD4 Th & Naive TREG	22405
CD44+ CD8 T Other & CD44+ CD8 T Other	22351
Mesenchymal & Ki-67+ Neoplastic	20910
CD44+ CD8 T Other & CD44+ CD4 Th	20823
CD44+ CD8 T Other & CD44- CD4 Th	20030
CD44+ CD8 T Other & B cells	19305
CD44- CD8 T Other & Naive TREG	16461

B cells & Mesenchymal	15010
mTREG & B cells	14656
mTREG & Ki-67- Neoplastic	14362
CD44- CD8 T Other & CD44+ CD4 Th	12734
CD44- CD4 Th1 Other & CD44- CD4 Th1 Other	11730
mTREG & Mesenchymal	10419
CD44- CD4 Th1 Other & Myeloid cells	9616
mTREG & mTREG	9087
CD8 T NAIVE & CD44- CD8 T Other	8303
Naive TREG & Naive TREG	7839
CD8 T NAIVE & CD44- CD4 Th	7103
B cells & Ki-67+ Neoplastic	6512
CD44- CD4 Th & Ki-67+ Neoplastic	6452
CD44- CD8 T Other & Ki-67+ Neoplastic	6392
CD44- CD4 Th & T-BET+ TREG	6102
Naive TREG & Myeloid cells	6035
CD44+ CD4 Th & mTREG	5918
CD44- CD4 Th1 Other & Mesenchymal	5711
CD44- CD4 Th1 Other & Ki-67- Neoplastic	5640
CD8 TEMRA & CD44+ CD4 Th	5367
CD44- CD8 T Other & T-BET+ TREG	5300
CD44+ CD8 T Other & mTREG	5186
Naive TREG & Ki-67- Neoplastic	5185
CD8 T NAIVE & B cells	5149
T-BET+ TREG & B cells	5086
Naive TREG & mTREG	4921
CD44+ CD8 T Other & Ki-67- Neoplastic	4863
CD8 TEMRA & CD44+ CD8 T Other	4772
CD44+ CD4 Th & Mesenchymal	4593
CD44- CD4 Th1 Other & mTREG	4305
CD44+ CD4 Th & Naive TREG	4166
CD8 TEMRA & B cells	3878
CD44+ CD8 T Other & Mesenchymal	3536
CD44+ CD4 Th & Ki-67- Neoplastic	3476
CD8 TEMRA & CD44- CD8 T Other	3454
CD8 TEMRA & CD44- CD4 Th	3399
CD44- CD4 Th1 Other & T-BET+ TREG	3382
CD8 TEMRA & CD8 TEMRA	3337
CD8 TEMRA & Myeloid cells	3226
CD44- CD4 Th1 Other & CD44+ CD4 Th	3112
CD44- CD4 Th1 Other & Naive TREG	3052
CD44+ CD8 T Other & CD44- CD4 Th1 Other	2766
CD44+ CD8 T Other & Naive TREG	2300
CD4 Th1EMRA & CD44- CD4 Th	1997

CD4 Th1EM & CD44- CD4 Th	1949
mTREG & Ki-67+ Neoplastic	1924
T-BET+ TREG & Myeloid cells	1857
Naive TREG & Mesenchymal	1852
CD4 Th1EMRA & B cells	1839
Naive TREG & T-BET+ TREG	1681
CD4 Th1EM & Myeloid cells	1667
CD4 Th1EMRA & CD44+ CD4 Th	1607
CD4 Th1EM & CD44+ CD4 Th	1542
CD44- CD8 T Other & CD4 Th1EM	1486
mTREG & T-BET+ TREG	1458
CD8 TEM & CD44- CD8 T Other	1322
CD44+ CD8 T Other & CD4 Th1EM	1311
CD8 TEM & CD44+ CD8 T Other	1285
CD8 TEM & CD44+ CD4 Th	1283
CD8 T NAIVE & CD44- CD4 Th1 Other	1238
CD44- CD8 T Other & CD4 Th1EMRA	1162
CD8 TEM & CD44- CD4 Th	1140
T-BET+ TREG & T-BET+ TREG	1119
CD4 Th1EM & CD44- CD4 Th1 Other	1112
CD44+ CD4 Th & T-BET+ TREG	1092
CD8 TEX & CD44+ CD8 T Other	1071
CD44+ CD8 T Other & T-BET+ TREG	1020
T-BET+ TREG & Ki-67- Neoplastic	1013
T-BET+ TREG & Mesenchymal	969
CD44+ CD8 T Other & CD4 Th1EMRA	969
CD4 Th1EMRA & CD44- CD4 Th1 Other	934
CD4 Th1EMRA & Myeloid cells	932
CD8 TEMRA & Ki-67- Neoplastic	878
CD8 TEM & Myeloid cells	847
CD8 T NAIVE & CD44+ CD8 T Other	837
CD8 TEM & B cells	808
CD4 Th1EM & Mesenchymal	790
CD8 TEMRA & Naive TREG	769
CD8 TEX & CD44- CD8 T Other	754
CD8 T NAIVE & Myeloid cells	740
CD4 Th1EMRA & CD4 Th1EMRA	739
CD44- CD4 Th1 Other & Ki-67+ Neoplastic	727
CD44+ CD8 T Other & Ki-67+ Neoplastic	710
CD4 Th1EM & mTREG	685
CD8 T NAIVE & CD8 T NAIVE	678
CD8 TEM & CD8 TEM	628
CD8 T NAIVE & Naive TREG	618
CD4 Th1EM & B cells	609

CD44+ CD4 Th1 Other & Ki-67- Neoplastic	580
CD8 TEMRA & CD4 Th1EMRA	576
CD8 T NAIVE & mTREG	574
CD44+ CD4 Th1 Other & Myeloid cells	550
CD8 TEX & CD44+ CD4 Th	522
CD8 TEX & CD44- CD4 Th	514
CD4 Th1EM & Ki-67- Neoplastic	510
CD4 Th1EMRA & Naive TREG	507
CD44+ CD4 Th & Ki-67+ Neoplastic	495
CD8 TEM & CD8 TEMRA	478
CD44- CD4 Th1 Other & CD44+ CD4 Th1 Other	477
CD4 Th1EMRA & T-BET+ TREG	476
CD8 TEMRA & CD44- CD4 Th1 Other	467
CD8 TEMRA & mTREG	459
CD8 T NAIVE & CD44+ CD4 Th	457
Naive TREG & Ki-67+ Neoplastic	451
CD8 TEX & B cells	442
CD4 Th1EM & CD4 Th1EM	431
CD8 TEMRA & Mesenchymal	383
CD8 TEX & CD8 TEX	368
CD44+ CD4 Th1 Other & B cells	353
CD8 TEMRA & T-BET+ TREG	350
CD8 TEM & CD4 Th1EM	340
CD44+ CD4 Th1 Other & CD44+ CD4 Th1 Other	338
CD8 TEX & mTREG	316
CD8 TEX & Myeloid cells	316
CD8 TEM & mTREG	309
CD44+ CD4 Th1 Other & CD44- CD4 Th	303
CD4 Th1EMRA & CD44+ CD4 Th1 Other	290
CD8 TTEX & CD44+ CD8 T Other	285
CD4 Th1EM & T-BET+ TREG	281
CD44+ CD4 Th1 Other & Mesenchymal	278
CD8 TEMRA & CD8 TEX	250
CD4 Th1EMRA & Ki-67- Neoplastic	247
CD4 Th1EMRA & mTREG	239
CD8 TTEX & Myeloid cells	221
CD44- CD8 T Other & CD44+ CD4 Th1 Other	215
CD8 T NAIVE & T-BET+ TREG	213
CD44+ CD4 Th1 Other & CD44+ CD4 Th	206
CD8 TEM & CD44- CD4 Th1 Other	199
CD8 TEX & Ki-67- Neoplastic	199
CD8 TTEX & CD44- CD8 T Other	194
CD8 T NAIVE & Mesenchymal	193
CD44+ CD8 T Other & CD44+ CD4 Th1 Other	186

CD8 TTEX & CD44+ CD4 Th	176
CD8 TEMRA & CD4 Th1EM	174
CD4 Th1EMRA & Mesenchymal	172
CD8 TTEX & CD44- CD4 Th	168
CD8 TEM & T-BET+ TREG	159
T-BET+ TREG & Ki-67+ Neoplastic	150
CD8 T NAIVE & CD8 TEMRA	150
CD4 Th1EM & CD4 Th1EMRA	146
CD4 Th1EM & Naive TREG	137
CD8 TEM & CD4 Th1EMRA	131
CD8 T NAIVE & Ki-67- Neoplastic	116
CD8 TTEX & B cells	111
CD8 TEFF & CD44+ CD8 T Other	108
CD8 TEX & Naive TREG	101
CD8 TEX & CD44- CD4 Th1 Other	96
CD8 TEM & CD8 TEX	91
CD8 TEFF & B cells	88
CD8 TEM & Mesenchymal	85
CD8 TEX & T-BET+ TREG	83
CD8 TEX & CD8 TTEX	83
CD8 TEM & Naive TREG	82
CD8 TEMRA & Ki-67+ Neoplastic	81
CD8 TTEX & mTREG	80
CD8 TTEX & Ki-67- Neoplastic	77
CD8 TEX & Mesenchymal	75
CD8 TEX & CD4 Th1EM	72
CD8 TEM & Ki-67- Neoplastic	68
CD44+ CD4 Th1 Other & Ki-67+ Neoplastic	65
CD8 TEFF & CD44- CD8 T Other	64
CD44+ CD4 Th1 Other & T-BET+ TREG	61
CD8 TEFF & CD8 TEMRA	56
CD4 Th1EFF & B cells	56
CD44+ CD4 Th1 Other & mTREG	54
CD8 TEFF & Myeloid cells	50
CD8 TEFF & CD44- CD4 Th	49
CD4 Th1EFF & Myeloid cells	47
CD4 Th1EM & Ki-67+ Neoplastic	45
CD8 TEFF & CD8 TEFF	42
CD4 Th1EM & CD44+ CD4 Th1 Other	41
CD8 T NAIVE & CD4 Th1EMRA	35
CD8 TEMRA & CD8 TTEX	34
CD44+ CD4 Th1 Other & Naive TREG	34
CD8 TEMRA & CD44+ CD4 Th1 Other	31
CD8 TTEX & Mesenchymal	30

CD8 TEX & CD4 Th1EMRA	29
CD8 T NAIVE & CD4 Th1EM	28
CD4 Th1EFF & CD44+ CD4 Th	28
CD8 TEFF & CD44- CD4 Th1 Other	26
CD8 TEFF & Mesenchymal	25
CD8 TTEX & Naive TREG	25
CD8 TEFF & Ki-67- Neoplastic	24
CD4 Th1EMRA & Ki-67+ Neoplastic	23
CD8 T NAIVE & CD8 TEM	22
CD8 TEX & Ki-67+ Neoplastic	22
CD4 Th1EFF & CD44+ CD4 Th1 Other	21
CD8 TTEX & CD44- CD4 Th1 Other	21
CD8 T NAIVE & CD8 TEX	20
CD8 T NAIVE & CD44+ CD4 Th1 Other	20
CD4 Th1EFF & Ki-67- Neoplastic	19
CD4 Th1EFF & CD44- CD4 Th1 Other	18
CD8 TTEX & CD4 Th1EM	18
CD8 TTEX & CD8 TTEX	17
CD8 TTEX & Ki-67+ Neoplastic	15
CD4 Th1EFF & CD4 Th1EMRA	15
CD8 TEFF & CD44+ CD4 Th	13
CD8 TEM & CD8 TTEX	11
CD8 TEMRA & CD4 Th1EFF	11
CD8 TEX & CD44+ CD4 Th1 Other	10
CD44- CD8 T Other & CD4 Th1EFF	8
CD8 T NAIVE & Ki-67+ Neoplastic	8
CD4 Th1EFF & Ki-67+ Neoplastic	8
CD44+ CD8 T Other & CD4 Th1EFF	7
CD4 Th1EFF & CD44- CD4 Th	7
CD8 TTEX & CD4 Th1EMRA	7
CD8 TTEX & T-BET+ TREG	7
CD8 TEM & Ki-67+ Neoplastic	5
CD4 Th1EFF & Naive TREG	5
CD8 TEFF & CD8 TTEX	5
CD8 TEFF & T-BET+ TREG	4
CD8 TEFF & CD44+ CD4 Th1 Other	4
CD8 TEM & CD44+ CD4 Th1 Other	4
CD4 Th1EFF & CD4 Th1EM	4
CD8 TEX & CD4 Th1EFF	4
CD4 Th1EFF & Mesenchymal	4
CD8 TEFF & Naive TREG	4
CD8 T NAIVE & CD8 TEFF	3
CD4 Th1EFF & CD4 Th1EFF	3
CD4 Th1EFF & T-BET+ TREG	3

CD4 Th1EFF & mTREG	2
CD8 T NAIVE & CD8 TTEX	2
CD8 TEM & CD4 Th1EFF	2
CD8 TEFF & mTREG	1
CD8 TEFF & CD8 TEM	1